MT Striped Birefringence Pattern Formation and Application of Laser Tweezers in Microrheology, Bacterial Motility and Adhesion

by

Yifeng Liu

M. Sc., Brown University, 2005

B. Sc., University of Science and Technology of China., 2003

Thesis

Submitted in partial fulfillment of the

requirements for the degree of Doctor of Philosophy

in the Department of Physics at Brown University

Providence, Rhode Island

May, 2009

Abstract of "MT Striped Birefringence Pattern Formation and Application of Laser Tweezers in Microrheology, Bacterial Motility and Adhesion" by Yifeng Liu, Ph.D., Brown University, May, 2009.

Various mechanisms govern pattern formation in chemical and biological reaction systems, giving rise to structures with distinct morphologies and physical properties. The self-organization of polymerizing microtubules (MTs) is of particular interest because of its implications for biological function. We report a study of the microscopic structure and properties of the striped patterns that spontaneously form in polymerizing tubulin solutions and propose a mechanism driving this assembly. We further present a mechanical model to explain the process and mechanism of buckling, and to infer properties of MT bundles such as packing geometry and size.

Using oscillatory optical tweezers based active microrheology, the frequency-dependent viscoelasticity of MT bundled networks were measured. This method implements forced oscillation of a 1.5µm silica bead embedded in a MT bundled network. Both the storage modulus and the loss modulus depend on the direction of the oscillatory motion of the bead relative to the alignment direction of the bundles. Furthermore, we have built an infrared laser tweezers setup for passive microrheology and to study the biophysics of bacterial motility and adhesion. We determined the force profile both near the center of the trap and at the far edge. Using the newly-built laser

tweezers and position detection system, we studied microrheological properties of F-actin in both isotropic and nematic phases. This method records the displacement of thermally driven micron-sized beads, based on which shear moduli of the underlying network were calculated. The result is consistent with that obtained by video particle tracking.

In addition, we use the calibrated optical trap to determine the trapping force on a swimming *Caulobacter crescentus* swarmer cell during its escape from the trap center. We further apply laser tweezers to study the rotation of a trapped *Caulobacter* swarmer cell and the process by which the cell struggles to escape from the trap center. Aided by the laser trap, we also show that bringing the holdfast of a stalked cell close to a glass surface facilitates adhesion of the cell to the surface, consistent with the model that cells must overcome a repulsive barrier at the surface to adhere efficiently.

© Copyright 2009 by Yifeng Liu

This dissertation by Yifeng Liu is accepted in its present form by the Department of Physics as satisfying the dissertation requirement for the degree of Doctor of Philosophy.

Date 9/23/08

Jay X. Tang, Director

Recommended to the Graduate Council

Date 9/23/08

Thomas R P

Thomas Powers, Reader

Date 9/23/08

James M Valles Jr

James M. Valles Jr., Reader

Approved by the Graduate Council

Date ____________

Sheila Bonde
Dean of the Graduate School

Vita

Education

- **Brown University, Providence, RI 02912** *2003-2008*
  - *Ph.D. in Physics.* Department of Physics. *September 2008*
  - *M.Sc. in Physics.* Department of Physics. *May 2005*
- **University of Science and Technology of China, Hefei, P.R. China** *1999-2003*
  - *B.Sc. & Eng. in Materials Science and Engineering.* Department of Materials Science and Engineering. *July 2003*

Publications and Manuscripts

- **Y. Liu**, Y. Guo, J. M. Valles Jr. and J. X. Tang, "Microtubule bundling and nested buckling drive stripe formation in polymerizing tubulin solutions" *Proc. Natl. Acad. Sci. U.S.A.*, **103**, 10654 (2006)

- Y. Guo, **Y. Liu**, J. X. Tang and J. M. Valles Jr., "Polymerization Force Driven Buckling of Microtubule Bundles Determines the Wavelength of Patterns Formed in Tubulin Solutions" *PRL*, **98**, 198103 (2007)

- Y. Guo, **Y. Liu**, R. Oldenbourg, J. X. Tang and J. M. Valles Jr., "Effects of Osmotic Force and Torque on Microtubule Bundling and Pattern Formation" (*submitted*)

- Jun He, Michael Mak, **Yifeng Liu** and Jay X. Tang, "Counter-ion Dependent Microrheological Properties of F-actin Solution across Isotropic-Nematic Phase Transition" Phys. Rev. E , **78**, 011908 (2008)

- **Yifeng Liu**, Guanglai Li, Anubhav Tripathi, Yves V. Brun, and Jay X. Tang, "Application of laser tweezers in the studies of bacterial swimming, cell body rotation, escape and adhesion" (*submitted*)

Experiences

- Research Assistant. Advisor: Professor Jay X. Tang, Department of Physics, Brown University, Providence, RI. *May 2004 - August 2008.*

- Teaching Assistant. Department of Physics, Brown University, Providence, RI.

  September 2003 - May 2004.

Preface

This thesis presents two biophysics studies, one is on microscopic investigation and mechanical modeling of Microtubule (MT) striped birefringence pattern formation *in vitro*, the other is about the construction of an optical tweezers and position detection system and its applications in microrheology and bacterial motility and adhesion. These two studies are presented as two separated parts.

In part one, I first give an introduction to MT and MT birefringence patterns in Chapter 1. Chapter 2 describes the experimental methods and techniques used in this study including sample preparation, various microscopic methods and details about certain measurements. In Chapter 3, the macroscopic and microscopic structure, and physical properties of MT striated birefringence patterns are presented. A nested buckling model is also proposed to explain the undulations of birefringence and fluorescence intensity. These results were published in [57]. Based on the observed pattern structures and further studies on the growth of bundles and solution retardance, we propose a mechanical model for the buckling process in Chapter 4 and the results were published in [42]. The results regarding the effects of PEG on MT bundling and pattern formation has been submitted for publication [41].

In part two, I first gave an introduction to optical tweezers and microrheology in chapter 4. In chapter 5, I described the construction of the optical tweezers and position detection system, and the process of calibrating the optical trap. In chapter 6, the application of optical tweezers in microrheology is presented, including experimental methods and results. In chapter 7, the application of optical tweezers on bacterial motility and adhesion is presented.

Yifeng Liu

Acknowledgments

The first part of the work presented on MT pattern formation in this thesis is a collaborative project with Yongxing Guo under the joint supervision of Prof. Jay X. Tang and Prof. James M. Valles Jr.

I would like to express my great thanks to my thesis advisor, Prof. Jay X. Tang, for his supervision and insightful advice throughout this work. My great thanks also go to Prof. James M. Valles Jr. for his kind support and valuable discussions. I would also like to thank Yongxing Guo for collaborating in the MT pattern formation project. I would like to recognize all former and current lab members including: Dr. Karim Addas, Dr. Guanglai Li, Dr. Jorge Viamontes, Dr. Jing Wang at Lehigh University, Dr. Qi Wen, Jun He, Hyeran Kang and Patrick Oakes. Special appreciation also goes to Prof. Allan F. Bower, Prof. Yves V. Brun at Indiana University, Prof. Rudolf Oldenbourg at Marine Biology Lab, Prof. Daniel OuYang at Lehigh University, Prof. Thomas Powers, Prof. Anubhav Tripathi for their helpful suggestions. I also want to thank my parents and friends for their encouragements and support throughout my experience at Brown University.

Contents

Vita iv

Preface vii

Acknowledgments ix

List of Figures xv

I Investigation of Mechanism and Characteristics of Microtubule Striated Birefringence Patterns 1

1 Introduction to Microtubule (MT) and MT Pattern Formation 2

1.1 What is microtubule 2

1.2 Motivation and importance of studies on MT assembly and pattern formation 5

2 Experimental Methods 8

2.1 Experimental chamber 8

2.2 Purification of tubulin and polymerization of MTs 8

2.3 Kinetics measurement 9

2.4 Aligning MTs with static magnetic fields 10

2.4.1 Magnetic torque on a single MT 11

2.4.2 Time needed to align a MT in a magnetic field 11

2.5 Fluorescence and phase-contrast microscopy 12

2.6 Birefringence measurements 13

2.7 MT bundle size measurement using PolScope 14

2.8 Sedimentation and quantitative fluorescence assay 14

3 Properties of Microtubule Striped Birefringence Patterns 16

3.1 Macroscopic appearance of birefringence patterns 16

3.1.1 Role of convective flow and gravity in pattern formation . . . 19

3.2 MT bundle formation 20

3.3 Small angle x-ray scattering experiments and data analysis 26

3.4 Birefringence measurement, phase contrast and fluorescence imaging of striated patterns 30

3.4.1 Quantitative analysis of periodic variations in birefringence and fluorescene intensity 30

3.5 Decomposition of the pattern structure into MT bundles and dispersed MTs in the network 34

3.6 Estimation of MT bundle size and bending energy based on retardance measurement . . . 35

3.7 Time evolution of retardance, bundle length and buckling wavelength 38

4 Mechanism of Striped Pattern Formation and a Mechanical Buckling Model 43

4.1 Mechanism of striped birefringence pattern formation . . . 43

4.2 Estimation of buckling wavelength based on minimization of energy . 44

4.3 The mechanical buckling model . . . 46

4.3.1 Buckling force . . . 49

4.4 Numerical estimates about buckling wavelength . . . 49

II Optical Tweezers and Its Applications in Microrheology and *Caulobacter* Motility and Adhesion 53

5 Introduction to Optical Tweezers and Microrheology 54

5.1 How optical tweezers work . . . 54

5.2 Microrheology . . . 57

5.2.1 Passive microrheology . . . 57

5.2.2 Active microrheology . . . 60

6 Setup of the Optical Trapping and Position Detection System 63

6.1 Optical tweezers setup . . . 63

6.2 Position detection using photodiode detector 65

6.3 Calibration of the optical trap 66

6.3.1 Theory 66

6.3.2 Experimental determination of trap stiffness and whole range trap force 68

7 Application of Optical Tweezers in Microrheology of Microtubule and Actin Networks 75

7.1 Experimental methods 75

7.1.1 Measurement of viscoelasticity of isotropic and nematic actin networks using passive microrheology 75

7.1.2 Measurement of anisotropic elastic properties of MT bundled network using active microrheology 79

7.2 Results and discussion 82

7.2.1 Moduli as a function of frequency for isotropic and nematic F-actin solutions 82

7.2.2 Anisotropic elastic properties of bundled MT network 88

8 Application of Optical Tweezers in the Study of Bacteria Swimming and Adhesion 91

8.1 Introduction 91

8.2 Experimental methods 93

8.2.1 Bacteria sample preparation 93

8.3 Results and discussion 94

8.3.1 Trapping force on *Caulobacter* swarmer cells 94

8.3.2 Cell body rotation of a trapped *Caulobacter* swarmer cell . . . 95

8.3.3 Escape of a *Caulobacter* swarmer cell from the laser trap . . . 98

8.3.4 Facilitated adhesion of a *Caulobacter* stalked cell via holdfast using laser tweezers 102

8.4 Summary and conclusion 105

Bibliography **109**

List of Figures

1.1 Structure of a microtubule (Adapted from http://www.med.unibs.it). 3

1.2 Schematic drawing of a mitotic spindle (adapted from www.sparknotes.com). Microtubules aligns and segregates chromosomes during eukaryotic cell division. 3

1.3 GTP-Cap Model for Microtubule Dynamic Instability. The polymerization phase is thought to be stabilized by a thin cap of tubulin dimers at the microtubule plus-end with a GTP molecule associated with each beta-tubulin subunit. Stochastic loss of the GTP cap, due to hydrolysis or subunit loss, results in a transition to the depolymerizing phase known as catastrophe. Back transition (rescue) is also observed. Taken from Inoue and Salmon (1995) Mole. Biol. Cell 6:1619-1640. 4

3.1 MT striped birefringence pattern observed between crossed polarizers. The axis of the cuvette was at 0^o (left) and 45^o (right) relative to that of the polarization directions of the polarizers, respectively. The dimensions of the cuvette are 40 x 10 x 1 mm. 17

3.2 Pattern development of a polymerizing 5 mg/ml MT solution following initial alignment by a 9 Tesla vertical static magnetic field for 5 min. The images were taken between crossed polarizers with the long axis of the cuvette (8 mm wide, 0.4 mm thick) at 45° with respect to the polarizing directions of the polarizers. (A) Image after 5 min of polymerization in the magnetic field. Notice that the solution appears brighter than the background region outside the meniscus, which has no birefringence. Rotating the cuvette by 45° changes the image to dark (data not shown), indicating that MTs are aligned in the magnetic field direction. (B) The same sample imaged 30 min after initiation of polymerization, showing formation of stripes which are aligned predominantly in the direction perpendicular to the direction of initial bulk alignment. 17

3.3 Time evolution of a MT pattern. The images were taken between crossed polarizers with the long axis of the cuvette (8 mm wide, 0.4 mm thick) at 45° with respect to the polarizing directions of the polarizers. The arrow indicates the direction of gravity. 18

3.4 Time series of a MT pattern formation during the initial stage. Dye particles were added to the tubulin solution before polymerization. . 19

3.5 Wave-like patterns formed in capillaries where shear flow was purposely induced. The capillary is 500 μm wide. 20

3.6 Successive frames of a typical phase-contrast movie showing buckling of MT bundles. The contrast of the images here was enhanced for better visualization. 8 mg/ml tubulin solution in a 40 × 10 × 1 mm cuvette was prepared as described in Materials and Methods. The sample was subjected to convective flow (induced by asymmetrical thermal contacts between the two edges of the cuvette with a water bath-warmed aluminum holder) for the first 9 min and then the cuvette was laid flat on the microscope stage at 30°C. 21

3.7 MT bundles detected by both birefringence and fluorescence measurements. MTs polymerized from a 5 mg/ml tubulin solution in glass cuvettes were taken out and then applied on a coverslip and covered with a glass slide. (A) Results of the PolScope measurement. Brightness indicates the magnitude of retardance and pins represent the slow axis directions which are consistent with the orientations of MT bundles. (B) Fluorescence image of the rectangular region as indicated in A. 22

3.8 MT bundles observed using high magnification fluorescence microscopy. MTs polymerized from a 5 mg/ml tubulin solution in glass cuvettes were taken out and then applied on a coverslip and covered with a glass slide. 23

3.9 A typical confocal image of MT bundles (green). MTs were polymerized in glass capillaries and labeled with taxol conjugated Oregon Green. 23

3.10 Scattering pattern from a SAXS scan. The scattering pattern contains the information on the structure of the sample. The solvent scattering has been subtracted. Different rings around the axis of the initial incident beam represent different scattering angles θ. The scattering intensity I(q) at each scattering angle was averaged over the region between the two red lines. The brightest region in the center is where the strong main beam (containing unscattered beam) hit. 28

3.11 Plot of logarithm of scattering intensity log(I) versus scattering vector q. The peak positions are at 0.0046, 0.028, 0.057, 0.084 inverse angstrom, respectively. 28

3.12 Scattering from oriented solution of hydrated MTs [16]. The value of q for the first peak is at 0.027 inverse angstrom, the second peak is at 0.055 inverse angstrom, the third peak is at 0.084 inverse angstrom. All these three peaks correspond to Fourier transform of the MT cylinder. 29

3.13 Theoretical interparticle interference function [62]. d and f corresponds to arrays of finite size with perfect hexagonal symmetry corresponding to regular bundles of 19 microtubules; e and g corresponds to finite paracrystals in two dimensions corresponding to bundles of microtubules (about 20 MTs per bundle) with deviations from hexagonal arrangement. 29

3.14 Quantitative analysis of the striped patterns based on birefringence measurements [57]. (A) PolScope measurement of a typical sample self-organized in 3.3 mg/ml tubulin solution (taxol-Oregon Green added for fluorescence imaging performed on the same sample). The solution in a 0.4 mm thick cuvette was initially exposed to a 9 Tesla magnetic field for 30 min. The measurement was done after the pattern was stable. The brightness indicates the magnitude of retardance and the pins show slow axis orientations. (B) Retardance values along the white line in A (blue curve) and fit (red curve) using $\Delta(x) = \Delta_0 \sqrt{1 + \tan^2 \varphi(x)}$. The x axis starts from the left end of the white line in A. The slow axis orientations φ are measured values as shown in C. The only fitting parameter is Δ_0. (C) Slow axis orientations along the same line. (D) Schematic showing that the packing density is proportional to $\sqrt{1 + \tan^2 \varphi}$ for nested MT bundles (each curve represents a bundle). (E) Retardance along the white line in A and fit proportionally to $\sqrt{1 + \tan^2 \varphi}$, where φ is the slow axis direction at each corresponding position. This figure is taken from [57]. 31

3.15 Quantitative analysis of the striped patterns based on fluorescence measurement [57]. (A) Phase contrast image (contrast enhanced) of the same region as in Fig. 3.14 but with a smaller field of view. Blue points are manually picked up along a MT bundle. The red curve is a fit to the shape of the bundle using the sum of three sinusoidal functions. (B) Fluorescence image of the same region, the red curve is the same as in A. (C) The blue curve is a plot of the fluorescence intensity along the red curve in B as a function of the horizontal axis, x. The red curve is a fit using $I(x) = I_b + I_0\sqrt{1 + \tan^2\varphi(x)}$, witch yields $I_b = 299$ and $I_0 = 143$. Here $tan\varphi(x)$ corresponds to the calculated slope of the contour of the bundle based on the fit to its shape. (D) Linear fit of fluorescence intensity to $\sqrt{1 + \tan^2\varphi}$ using data from C. The non-zero intercept of the line with the ordinate implies a background fluorescence caused by dispersed MTs. This figure is taken from [57]. 32

3.16 Illustration and measurements of the uniform elongation of MT bundles [1]. (a),(b) Phase contrast images of a sample region, showing progression of the pattern over 1 h. MT bundles are discerned by the thin striations. Segments 1 through 3 are adjacent pieces of a contour followed by bundles. The segment ends are defined by fiducial marks. (c) Magnified view of the region denoted by the white box in (b), showing an encircled fiducial mark. (d) Fast Fourier Transform (FFT) of (c). (e) The radially averaged FFT intensity plotted versus the azimuthal angle θ and fit using a Gaussian function. The local bundle orientation is orthogonal to the angle at which the Gaussian fit peaks. (f)-(h) Length of segments 1 (f), 2 (g), 3 (h) as a function of time. (i) Lengths of the three segments as a function of time, normalized to their lengths at 46 min. This figure is taken from [42]. 39

3.17 Time evolution of a MT pattern obtained by measuring the retardance and slow axis of the sample using a PolScope imaging system [2]. (a),(b) Retardance images of a sample region at 12 and 100 min of self-organization, respectively. The color bar shows the retardance magnitude scale and the green pins provide the slow axis orientation. The straight white lines represent the slow axis line scan position. (c) Slow axis line scan (black) and the fitted slow axis orientation $\varphi(x) = \arctan\{A\frac{2\pi}{\lambda}\cos[\frac{2\pi}{\lambda}(x + x_0)]\}$ (red) at 100 min. (d) The dominant buckling wavelength λ, obtained from the fitted shapes of the bundle at individual time points. (e) The length evolution of the fitted bundle contour. $L_0 = 1544\,\mu$m is the initial unbuckled length of the bundle. The segment before the arrow designates the latent period prior to the onset of the buckling. (f) The magnitude of the retardance averaged over the line as shown in (a) versus the normalized length L/L_0. This figure is taken from [42]. 40

4.1 Schematic drawing to illustrate the elastic buckling model. 46

4.2 A schematic showing an array of bundles embedded in an elastic medium. The blue circles represent the cross sections of representative bundles with a spacing of d. The diameter of each bundle is 2R. F indicates the force exerted on the bundles by the surrounding elastic network, which is assumed to be linear with the extent of buckling ξ as: $F = \alpha\xi\, dx$. Here α is the elastic constant of the surrounding medium and dx represents unit bundle length. The stress σ is: $\sigma = \frac{F}{2R\,dx}$, and strain γ can be written as: $\gamma = \frac{\xi}{d}$. Therefore, shear modulus G' can be calculated as $G' = \frac{Fd}{\xi 2R\,dx} = \frac{\alpha\xi\,dx\,d}{\xi 2R\,dx} = \frac{d}{2R}\alpha$. So α is related to G' as $\alpha = \frac{2R}{d}G' = \sqrt{\eta}\,G'$, where η is the volume fraction of bundles. 50

5.1 Schematic drawing to illustrate origin of optical force in the regime where ray optics can be used. The initial momentum of the light beam is denoted as M and the final momentum to each photon is denoted M' in the figure. The momentum change is represented by the red arrow. The force thus induced on the sphere points in the opposite direction, as represented by F. 55

5.2 Schematic showing a damped driven harmonic oscillator, which illustrates the motion and the forces on a particle using an applied oscillatory laser trap. The solid line denotes the origin of the coordinate system, the dashed line indicating the location of the bead, and the dotted line the center of the oscillating trap. The equation of motion for the particle is: $m\ddot{x}(w,t) = -6\pi\eta(w)a\dot{x}(w,t) - \kappa(w)x + k_{ot}Ae^{iwt} - k_{ot}x(w,t)$, where k_{ot} is the trap stiffness of the oscillating beam, A is the amplitude of the oscillatory beam with frequency w, $\eta(w)$ and $\kappa(w)$ represent the viscosity and the elasticity of the medium, respectively, and $x(w,t)$ is the bead displacement with respect to the center of the trap (solid line). 61

6.1 Laser tweezers setup. 64

6.2 Scattering force, gradient force and total trap force on a one micron spherical particle as a function of the displacement of the particle to the trap center. This result is derived by A. Ashkin [9]. 67

6.3 Measurement of trap force in the linear region of the trap. (a) Power spectral density of a typical bead and a Lorentzian fit $S_{xx}(f) = \frac{k_B T}{\pi^2\beta(f^2+f_c^2)}$. (b) Trap potential as a function of displacement and a parabolic fit. The potential is calculated from the distribution of bead displacement at the same laser intensity as that used in (a). (c) Comparison of trap force obtained from (a), denoted by the solid line, and (b), denoted by the gray dots and a linear fit to them shown as the dashed line. . . . 70

6.4 A picture of the flow cell. The cell is about 15 cm long and 5 cm wide. At the end of the cell are inlet and outlet tubings. The two outlets in the middle are connected to vacuum. A gasket is attached to the bottom of the cell (green) to ensure good isolation from the outside air and prevent leaking of solution. 71

6.5 (a) The velocity of a typical bead initially trapped but then dislodged upon application of flow in the flow chamber. (b) The solid circles represent the force on the same bead as in (a) and were fit to an exponential function to yield $y = 1.4 \times e^{-1.5\,x}$ (dashed curve). In the linear region, the gray dots (red) within a displacement of about 100 nm are replots from Fig. 6.3c, and the dashed line depicts the expected force profile in this region. 72

6.6 An illustration showing the force profile and range of a laser trap. A picture of the trap is shown in red, a probe particle in blue, and the whole force profile in black. The dashed line indicates the position of the beam waist. The dimensions are drawn roughly to scale. The trap force is linear with displacement in the low displacement regime, consistent with experiments. The force drops gradually down to zero beyond the peak when the bead is so far away from the trap center that no laser beams are scattered by the bead. 74

7.1 A schematic diagram of the active microrheology experimental setup [104]. The area enclosed by the dashed lines represents an inverted optical microscope. 78

7.2 Moduli for a typical 0.5 mg/ml isotropic F-actin solution (contribution to elasticity due to the trap stiffness has been subtracted). Filled symbols represent G' and empty symbols represents G". Black symbols represent data for the direction perpendicular to the sample capillary. Red symbols represent data for the direction parallel to the capillary. The sampling frequency was 20000 Hz and 540000 data points were recorded. 84

7.3 Moduli for a 1 mg/ml actin solution (contribution to elasticity due to the trap stiffness has been subtracted). Filled symbols represent G' and empty symbols represents G". Blue symbols represent data for the direction perpendicular to the sample capillary. Green symbols represent data for the direction parallel to the capillary. The sampling frequency was 2000 Hz and 540000 data points were recorded. 85

7.4 Frequency dependence of moduli for a 4 mg/ml nematic F-actin solution. For the spectra on the left, the bead displacement was measured with the VPT (video particle tracking) method and the mean square displacement was converted to moduli using Generalized Stocks Relation; for the spectrum on the right, the bead positions were tracked by the photodiode. In the overlapped region between the two dash dot lines, the laser tweezers based results are shown in gray symbols. The two methods give consistent results for G'_x, G'_y, and G''_y; G''_x measured by the VPT method, however, is about twice of that measured by laser tweezers based method. Both spectra were measured using 1 μm beads and obtained from averaging over ten beads. The solid straight line shows a scaling law of $\omega^{3/4}$. 86

7.5 (A) A representative fluorescence image superimposed on a bright field image, so that both MT bundles (green) and beads (yellow) can be seen. (B) Moduli as a function of frequency for bead 1, showing large differences between the two directions. 90

8.1 (a) The swimming velocity of each of three bacteria as a function of displacement from the center of the trap. (b) The empty symbols represent forces calculated from the velocities in (a), and the dashed curve is a replot from Fig. 6.5b. In the linear region, the gray dots within a displacement of about 100 nm are replots from Fig. 6.3c, and the dashed line depicts the expected force profile in this region. . . . 96

8.2 A schematic drawing which illustrates why the cell body aligns in the direction of the optical axis. Each end of the cell body experiences a trap force against the direction of the laser intensity gradient, shown as $F1$ and $F2$ in the figure. The net effect of these two forces is a torque which tends to rotate the cell body back to the optical axis direction. Therefore, the equilibrium position for the cell body is the optical axis direction. 97

8.3 Selected frames from a movie displaying the escape process of a trapped swarmer cell. The cross indicates the position of the trap center. The white curve on the last image shows the trajectory of the cell. The dark dots indicate the center positions of the cell body over the eight frames. 99

8.4 (a) Typical voltage signal as a function of time. The voltage is proportional to the displacement, projected in each of two orthogonal directions, of the cell body from the trap center. The dark thin curve shows that the total laser intensity was decreased stepwise. The other two curves represent the voltage traces in the two orthogonal directions acquired by the photodiode detector. (b) A magnified view of the voltage traces right before and after escape of the cell from the trap. (c) Power spectral density of the two voltage traces in (a), showing a wide peak corresponding to the rotation frequencies of the trapped cell. . 100

8.5 Schematic drawing of a cell tilting away from the optical axis. The straight arrow indicates the force generated by the flagella motor. The curved arrow indicates the resulting torque which tends to steer the cell towards the horizontal plane. 102

8.6 Facilitation of *Caulobacter* adhesion via holdfast by the laser trap. The cross indicates the center of the trap. The laser beam was blocked at later times, thus no cross is shown on the time frame of either 34s or 46s. The inset at the lower right corner of each picture depicts the facilitated adhesion process, in which the box represents the sample chamber, the dark tadpole-like drawing illustrates the cell and the horizontal line represents the position of the focal plane. 103

8.7 An example of DLVO energy of a bacterium interacting with a flat glass surface as a function of the distance from the cell to the surface. 106

Part I

Investigation of Mechanism and Characteristics of Microtubule Striated Birefringence Patterns

Chapter 1

Introduction to Microtubule (MT) and MT Pattern Formation

1.1 What is microtubule

A microtubule (MT) is composed of 13 staggered protofilament, built up by longitudinally associated α, β-tubulin heterodimers (see Fig. 1.1). The strict alternation of α- and β- subunits results in a longitudinal polarity [55]. Protofilaments form sheets at the ends of growing MTs, but curl and peel apart from each other at the ends of shortening MTs, eventually detaching as highly curved oligomers [26].

Microtubules constitute one of the most important components of the eukaryotic cytoskeleton. They participate in many fundamental cellular functions including the maintenance of shape, motility, and signal transmission, and play a determining role

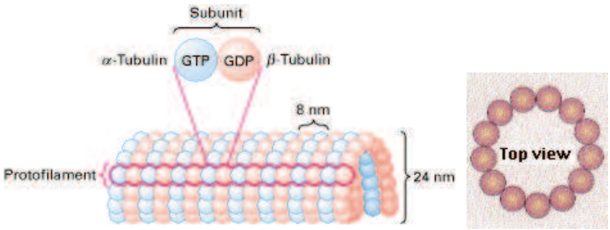
Subunit
α-Tubulin
GTP
GDP
β-Tubulin
8 nm
Protofilament
24 nm
Top view

Figure 1.1: Structure of a microtubule (Adapted from http://www.med.unibs.it).

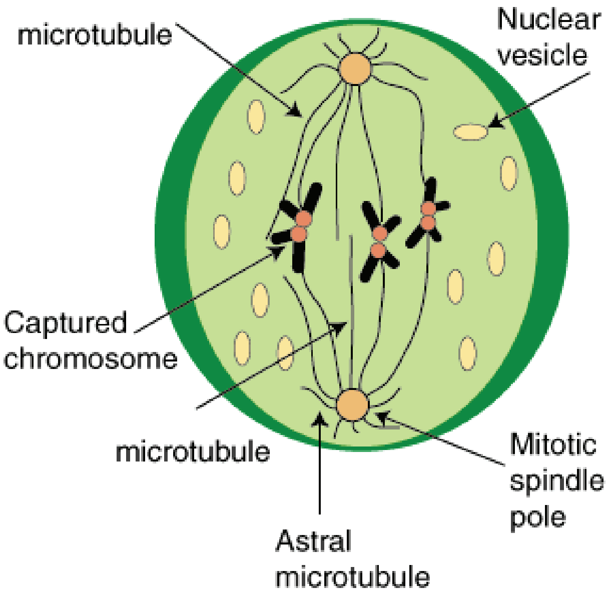
microtubule
Nuclear vesicle
Captured chromosome
microtubule
Astral microtubule
Mitotic spindle pole

Figure 1.2: Schematic drawing of a mitotic spindle (adapted from www.sparknotes.com). Microtubules aligns and segregates chromosomes during eukaryotic cell division.

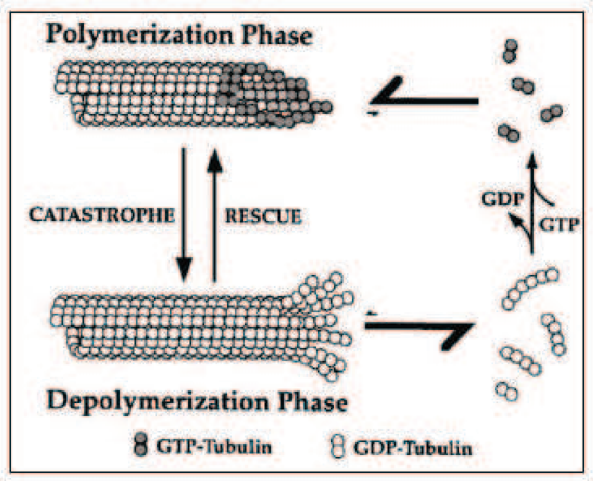

Figure 1.3: GTP-Cap Model for Microtubule Dynamic Instability. The polymerization phase is thought to be stabilized by a thin cap of tubulin dimers at the microtubule plus-end with a GTP molecule associated with each beta-tubulin subunit. Stochastic loss of the GTP cap, due to hydrolysis or subunit loss, results in a transition to the depolymerizing phase known as catastrophe. Back transition (rescue) is also observed. Taken from Inoue and Salmon (1995) Mole. Biol. Cell 6:1619-1640.

in the organizational changes that occur during the early stages of embryogenesis [30, 21]. Microtubules are a significant component of brain neuron cells and they make up the mitotic spindles (see Fig. 1.2) that separate the chromosomes during cell division [5].

At the basis of the active role of MTs lies dynamic instability: under the influence of GTP hydrolysis, a single MT alternates repeatedly between states of prolonged growth (polymerization) and shrinkage, both in a cell and with purified tubulin outside a cell (see Fig. 1.3).

MTs are polymerized from tubulin dimers at physiological temperatures with proper buffer conditions including GTP. β tubulin hydrolyzes guanosine triphosphate (GTP) during polymerization [105]. α tubulin also binds GTP, but this GTP is bound in a non-exchangeable manner (at the N-site) and is not hydrolyzed during polymerization [85]. MT polymerization dynamics is influenced by the addition of taxol. Taxol binds specifically to beta-tubulin in the microtubule [47] and causes microtubule bundle formation within the cell. It was found that 1.0 µM taxol induces a lateral aggregation of microtubules which, by 12 to 24 h of treatment, results in the appearance of dense bundles of tightly-packed microtubules [44].

1.2 Motivation and importance of studies on MT assembly and pattern formation

Cytoskeletal proteins can form dynamic spatial structures by themselves even in the absence of cellular organizing centers or molecular motors. Solutions of MTs and GTP can generate various dissipative structures including asters, vortices and polygonal networks [66]. The microtubule system could serve as a simple model for studying pattern formation by biomolecules in vitro [59]. The results of these studies may have important relevance and implications for the cellular functions of MTs based on their self-assembly and in connection with their mechanical properties.

Of particular relevance here are striped birefringence (light-polarizing) patterns that spontaneously form in MT solutions without motors. Hitt *et al.* attributed these patterns to the formation of liquid crystalline domains [46]. Tabony, on the other hand, proposed a reaction–diffusion based mechanism [88], suggesting that reaction–diffusion could account qualitatively for the concentration variations [89] and the sensitivity of the patterns to gravity and magnetic fields [74]. Similar striated patterns were found *in vivo*. In particular, an array of parallel wavy microtubules form between the cortical and inner cytoplasm of the vegetal hemisphere in amphibian eggs, likely serving as tracks of the microtubule associated motors for cytoplasmic transport [35].

We present results regarding the role of gravity, the structural basis and underlying mechanism for the birefringence stripes and the origin of the spatial concentration oscillations in the striped patterns through a series of microscopic investigations, including phase-contrast, fluorescence, and quantitative polarized light microscopy. Based on our observations of MT alignment, bundling, buckling, and the fact that the spatial concentration variation is solely an effect of periodic alignment of bundled MTs, we infer that the pattern formation in our system is mechanical in origin. Accordingly, we present a mechanical buckling model of a microtubule bundle within an elastic network formed by other similarly aligned and buckling bundles and unaligned MTs to explain the shape, wavelength, critical buckling force and other characteristics of the patterns such as retardance evolution, bundle growth rate and packing geometry. Moreover, we studied the effect of polymer molecules such as Polyethylene Glycol (PEG, MW=35 kDa) on microtubule bundling and pattern formation. The result regarding the modification of the pattern by PEG yields a better understanding of the mechanism of formation and characteristics of MT bundles in the striped patterns.

Chapter 2

Experimental Methods

2.1 Experimental chamber

Intracellular organization has to do with the confined geometry of cells. To simulate the closed environment of cells, we use rectangular cuvettes which have dimensions of 40 ×10 ×1 mm made of quartz (International Crystals, Oklahoma City, OK) or 50× 8 ×0.4 mm made of glass (Vitrocom, New Bedford, MA).

2.2 Purification of tubulin and polymerization of MTs

Tubulin was purified from fresh bovine brains by two cycles of polymerization and depolymerization, followed by cation exchange chromatography on a phosphocellulose column following standard protocols [99, 103]. Tubulin-containing fractions were pooled, concentrated by additional cycle of assembly and disassembly, homogenized in PM buffer (0.1 M PIPES, 2 mM MgCl2, 1 mM EGTA, pH 6.9) with 0.5 mM GTP, disbursed into aliquots, frozen in liquid nitrogen, and stored at – 80 °C.

Immediately before use, tubulin solutions were thawed and then centrifuged at 1,800 g for 5 min at 4°C to remove small amounts of aggregates. For most of our samples, the GTP concentration was 2 mM unless otherwise specified. Samples were degassed (after the addition of GTP) in cuvettes at 4°C to prevent air bubble formation that would otherwise occur during the increase in temperature to 37°C. The cuvettes were incubated on ice for 10 min before inducing polymerization.

2.3 Kinetics measurement

Microtubule assembly was initiated by adding GTP into a tubulin solution (4 °C) and filling the mixture into a rectangular cuvette, and then inserted the cuvette into holder in a circulating water-warmed Shimadzu spectrophotometer. The air temperature within the Shimadzu chamber was about 34 – 35 °C. Kinetics measurements were performed immediately after by recording optical density (i.e., absorbance) at 350 nm every two seconds for 1500 seconds (25 mins). What is measured is diminished transmittance of light due to scattering off objects of macromolecular particles. As tubulin polymerizes into microtubules, incident light scatters more the more microtubules (approximately 0.5 μm or longer) are polymerized. Assuming that Beer's law holds,

$$-log(\frac{I}{I_0}) = k\,c$$

, where I_0 is the incident light intensity and I is the outgoing light intensity. k is extinction constant and c is the concentration of MTs formed.

2.4 Aligning MTs with static magnetic fields

The application of static magnetic fields has been a non-intrusive mechanical method to align biological samples [16, 107, 94, 29]. In particular, the alignment of MTs in a magnetic field of a few Tesla has been shown by Glade *et al.* [39]. Theoretical estimation shows that the minimum field strength needed to align a $5\,\mu m$ MT parallel to the magnetic field direction is about 7.6 Tesla [16]. For MTs longer than $5\,\mu m$, the required field strength is even smaller. The magnetic field in our experiments was produced by a super-conducting magnet system (American Magnetics, Oak Ridge, TN) with a room temperature bore. The diameter of the bore is 11 mm. Pre-cooled tubulin solutions in glass cuvettes were placed in a 9 Tesla vertical magnetic field oriented parallel to the long axis of the cuvettes. The temperature of the bore was pre-equilibrated to 37°C by circulating warm air through it from above. The sample temperature, measured with a thermometer, rose from 0°C to 37°C in about 100 s. Observations and measurements were made at either room temperature or 30°C, when specified, after the sample was removed from the magnet.

2.4.1 Magnetic torque on a single MT

The magnetic energy of a single MT oriented at an angle θ with the direction of a magnetic field B is:

$$\Delta E = -\frac{L\Delta\chi}{2\mu_0} B^2 \cos^2\theta \tag{2.1}$$

Here L is the length of the MT, $\Delta\chi$ is the diamagnetic anisotropy of MT.

Therefore the torque induced by the magnetic field is:

$$\begin{aligned} \tau_B &= \frac{\partial \Delta E}{\partial \theta} \\ &= \frac{L\Delta\chi}{2\mu_0} B^2 \sin 2\theta \end{aligned} \tag{2.2}$$

2.4.2 Time needed to align a MT in a magnetic field

The equation governing the rotation of a MT in a magetic field is:

$$\beta \frac{d\theta}{dt} = -\tau_B,$$

Here $\beta = \frac{2\pi}{3}\frac{\eta L^3}{\log(L/d)}$ is the rotational drag coefficient and d is the diameter of a MT. Therefore,

$$\frac{2\pi}{3}\frac{\eta L^3}{\log(L/d)}\frac{d\theta}{dt} = -\frac{L\Delta\chi}{2\mu_0} B^2 \sin 2\theta$$

The above equation yields:

$$\begin{aligned} t &= (\ln\tan\theta - \ln\tan\theta_0)\frac{\mu_0\beta}{L\Delta\chi B^2} \\ &= (\ln\tan\theta - \ln\tan\theta_0)\frac{\mu_0}{\Delta\chi B^2}\frac{2\pi}{3}\frac{\eta L^2}{\ln(L/D)} \\ &\propto L^2, \end{aligned}$$

where θ_0 and θ are the initial and final angle between the MT and the magnetic field direction. Numerically, the time needed to rotate a $10\,\mu$m long MT from $\theta_0 = 45^\circ$ to $\theta = 10^\circ$ in a 9 Tesla magnetic field is about 47 s.

2.5 Fluorescence and phase-contrast microscopy

Microscopic structures of self-organized MT pattern inside cuvettes were examined with fluorescence and phase-contrast microscopy at room temperature on a Nikon ECLIPSE E800 microscope. Images of 12-bit depth were collected by a 1,392×1,040-pixel Coolsnap digital camera (Roper Scientific, Trenton, NJ) driven by META-MORPH imaging software (Universal Imaging, Downingtown, PA). For fluorescence imaging, MTs were labeled to a 3.5% stoichiometry in the ratio of total number of Oregon green-conjugated taxol (Molecular Probes) molecules to tubulin dimers. Blue light (wavelength 480 nm) was used for excitation, and green light emitted by taxol-Oregon green (peak wavelength 532 nm) was measured.

2.6 Birefringence measurements

The birefringence of objects is a sensitive indicator of structural order at dimensions finer than the wavelength of light. Birefringence can vary in time and space, revealing the subtle changes in ordered arrangements. One easy and quick method to examine sample birefringence is to place the cuvette between two sheets of Polaroid (Edmund Optics, Blackwood, NJ) oriented with their axes of transmission at 90° (extinction 99.98%) and illuminated by a light box (Hall Productions, Grover Beach, CA). 8-bit depth images were recorded by a CCD camera (Sony, XCD-SX900, NY) driven by Fire-I software at a resolution of 1280 × 1024.

More quantitative birefringence measurements were performed using a Nikon ECLIPSE E800 microscope equipped with a PolScope package (CRI, Cambridge, MA) and a standard CCD camera (MTI 300RC, Michigan, IN) with 640 × 480 resolution. Polscope technique is a sensitive and reliable tool for quantitative measurements of microscopic distributions of birefringence of biological samples [84]. The technique uses elliptically polarized illumination beam which is produced by a combination of a linear polarizer and two liquid crystal retarders. The polarization property of the illumination beam changes after going through the sample. The final polarization was probed by a circular analyzer. The intensity distribution of light on the image plane depends on the retardation of the liquid crystal retarders and birefringence of the sample. The functional dependence can be calculated by multiplying the Jones matrix of the illumination beam and the matrixes of the optical components including the sample that the beam goes through. Four settings of the liquid crystal retarders were used to calculate the corresponding intensity distribution. Solving the four functions relating the retarder settings and the intensity distribution yields the retardance and slow axis distribution of the sample. Background retardance caused by other optical components is subtracted [71].

2.7 MT bundle size measurement using PolScope

MT bundle size was calculated from the birefringence of the bundle as measured using PolScope. Retardance images were analyzed using Matlab. Specifically, a line scan was taken on the cross section of a MT bundle and the intensity along the cross section was integrated to yield the retardance area. Given that the integrated retardance area of a single MT is $A = 7.5\,nm^2$ [72, 51], the number of MTs along the cross section of the bundle can be determined.

2.8 Sedimentation and quantitative fluorescence assay

This assay was performed to test the contribution of free fluorescent taxol and free tubulin associated with taxol to the total fluorescence signal. First, the fluorescence of a solution of fluorescent taxol labeled (with a stoichiometry of 3.5% in the ratio of the total number of taxol molecules to that of tubulin dimers) MTs was measured using a fluorescence spectrometer (PerkinElmer, Wellesley, MA). Then the solution was centrifuged at 280,000g for 30 min to sediment MTs. The fluorescence of the supernatant was subsequently measured.

Chapter 3

Properties of Microtubule Striped Birefringence Patterns

3.1 Macroscopic appearance of birefringence patterns

When a sample of microtubules is inserted between two polarizers that have their axes of polarization at 90° to each other, the fraction of light which can pass through depends on the MT polarization. Thus, the axis of alignment of MTs can be mapped out based on the distribution of light passing through.

Fig. 3.1 shows a birefringence image taken through crossed polarizers. The dimensions of the cuvette are 40 x 10 x 1 mm. Fig. 3.2 shows a similar pattern formed by a MT solution which was exposed to a 9T magnetic field for 5 mim after initiation of

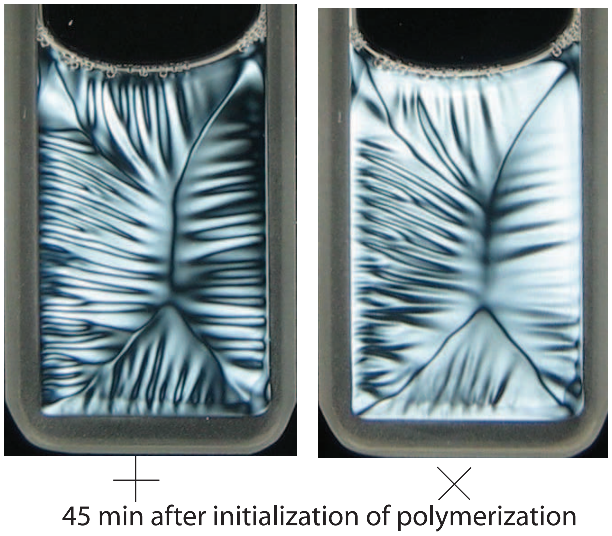
45 min after initialization of polymerization

Figure 3.1: MT striped birefringence pattern observed between crossed polarizers. The axis of the cuvette was at 0^o (left) and 45^o (right) relative to that of the polarization directions of the polarizers, respectively. The dimensions of the cuvette are 40 x 10 x 1 mm.

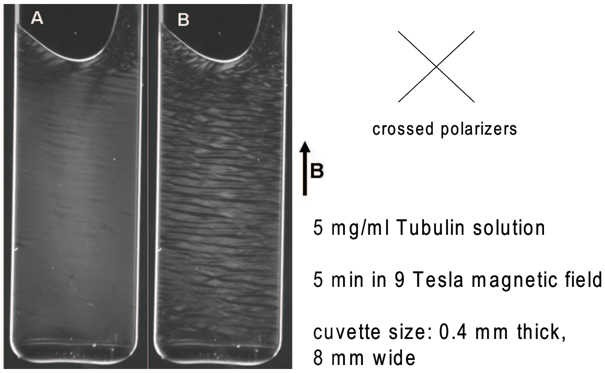
A
B
crossed polarizers
B
5 mg/ml Tubulin solution
5 min in 9 Tesla magnetic field
cuvette size: 0.4 mm thick,
8 mm wide

Figure 3.2: Pattern development of a polymerizing 5 mg/ml MT solution following initial alignment by a 9 Tesla vertical static magnetic field for 5 min. The images were taken between crossed polarizers with the long axis of the cuvette (8 mm wide, 0.4 mm thick) at 45° with respect to the polarizing directions of the polarizers. (A) Image after 5 min of polymerization in the magnetic field. Notice that the solution appears brighter than the background region outside the meniscus, which has no birefringence. Rotating the cuvette by 45° changes the image to dark (data not shown), indicating that MTs are aligned in the magnetic field direction. (B) The same sample imaged 30 min after initiation of polymerization, showing formation of stripes which are aligned predominantly in the direction perpendicular to the direction of initial bulk alignment.

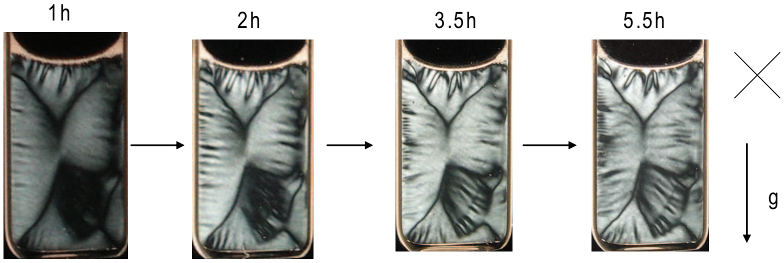

Figure 3.3: Time evolution of a MT pattern. The images were taken between crossed polarizers with the long axis of the cuvette (8 mm wide, 0.4 mm thick) at 45° with respect to the polarizing directions of the polarizers. The arrow indicates the direction of gravity.

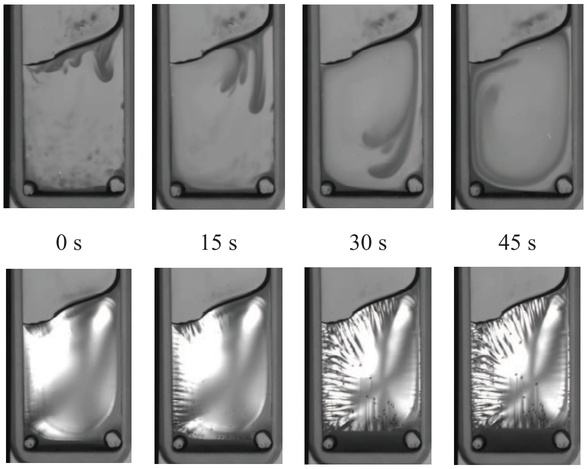

0 s 15 s 30 s 45 s

3 mins 5 mins 15 mins 20 mins

Figure 3.4: Time series of a MT pattern formation during the initial stage. Dye particles were added to the tubulin solution before polymerization.

polymerization. Alternating bright and dark regions were observed, indicating undulating microtubule orientations. Dynamic in nature, the overall shape of the pattern does not change much over the course of 6 hours (see Fig. 3.3), it only becomes more sharp and detailed.

3.1.1 Role of convective flow and gravity in pattern formation

Existence of convective flow was investigated by adding Phenol Red dye in the bottom of a cuvette before tubulin solution was added. Upon non-uniform increase of solution temperature, convection was observable by tracing the red dye particles. Fig. 3.4 displays a series of images from a movie where the motion of dye particles following the flow was apparent. A further evidence of flow induced alignment and subsequent pattern formation is that similar wave-like patterns (see Fig. 3.5) form in narrow

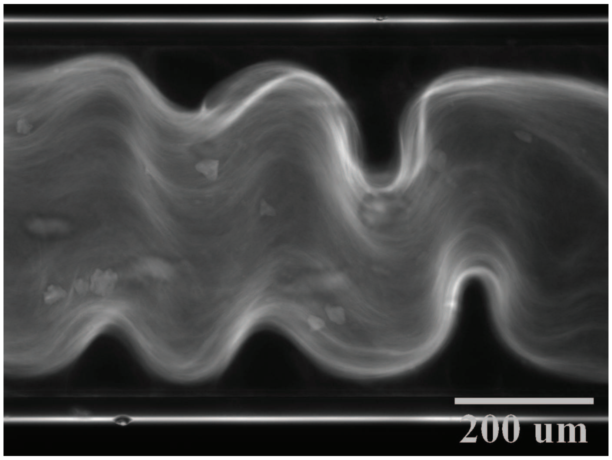

10X fluorescence image, 6hours after shear flow

Figure 3.5: Wave-like patterns formed in capillaries where shear flow was purposely induced. The capillary is 500 μm wide.

capillaries in which shear flow was purposely induced through injection of solution.

Stripes were less apparent when initiating MT polymerization in a upright cuvette which was warmed up uniformly, for example, when immersing the cuvette in a 37°C water bath. On the other hand, strips did form when warming a flat cuvette nonuniformly (data not shown). These control experiments demonstrate that gravity does not directly play a role in the formation of striped patterns, but convective flows do. No strips formed in experiments performed in space [90] because no convection was available to align MTs.

3.2 MT bundle formation

The sequence of phase contrast microscopy images shown in Fig. 3.6 reveals the morphology of the MTs inside striped patterns. At 10 min, striations with a gradual

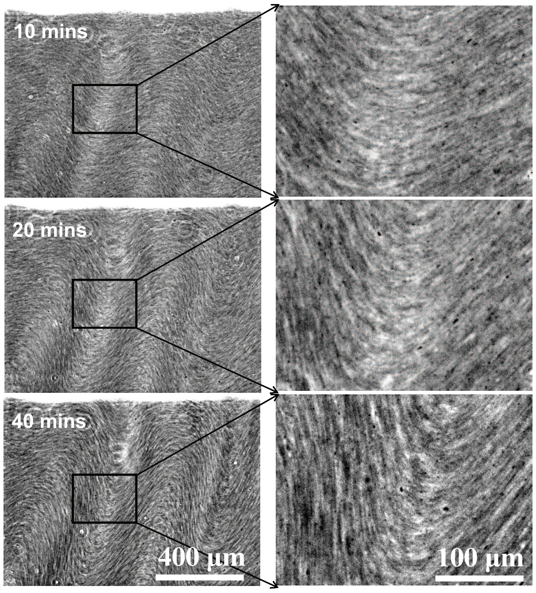

Figure 3.6: Successive frames of a typical phase-contrast movie showing buckling of MT bundles. The contrast of the images here was enhanced for better visualization. 8 mg/ml tubulin solution in a 40 × 10 × 1 mm cuvette was prepared as described in Materials and Methods. The sample was subjected to convective flow (induced by asymmetrical thermal contacts between the two edges of the cuvette with a water bath-warmed aluminum holder) for the first 9 min and then the cuvette was laid flat on the microscope stage at 30°C.

undulation are apparent. This undulation becomes stronger with time until its amplitude is comparable to its spatial period. We identify the striations as bundled MTs since single MTs are unresolvable with this technique.

Bundles of MTs are clearly recognizable in fluorescence and PolScope images of samples taken out from cuvettes which contain striped patterns, as shown in Fig. 3.8. MT clouds instead of bundles were observed in samples in which the stripes did not form. This result suggests that MT bundling is necessary for the formation of the striped patterns.

MT bundles observed at higher magnification using fluorescence microscopy are

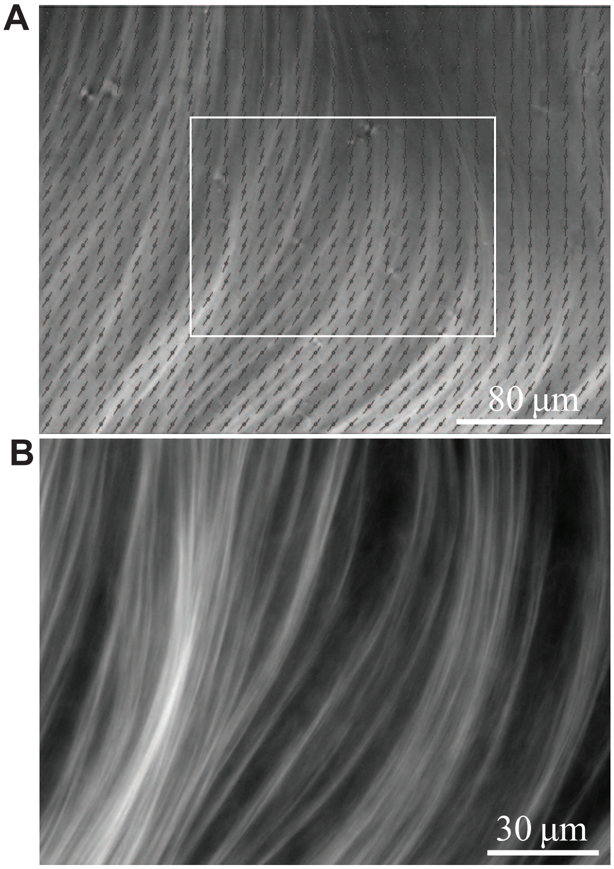

Figure 3.7: MT bundles detected by both birefringence and fluorescence measurements. MTs polymerized from a 5 mg/ml tubulin solution in glass cuvettes were taken out and then applied on a coverslip and covered with a glass slide. (A) Results of the PolScope measurement. Brightness indicates the magnitude of retardance and pins represent the slow axis directions which are consistent with the orientations of MT bundles. (B) Fluorescence image of the rectangular region as indicated in A.

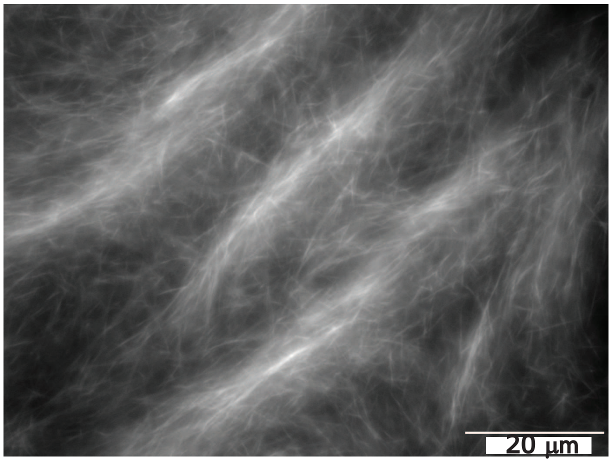

Figure 3.8: MT bundles observed using high magnification fluorescence microscopy. MTs polymerized from a 5 mg/ml tubulin solution in glass cuvettes were taken out and then applied on a coverslip and covered with a glass slide.

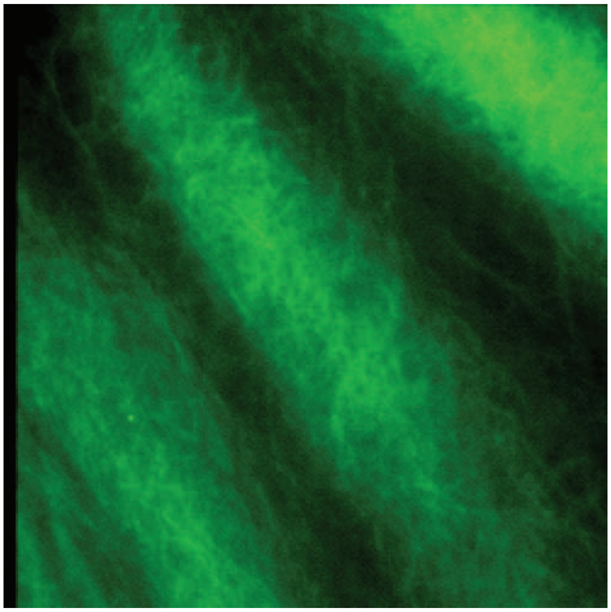

Figure 3.9: A typical confocal image of MT bundles (green). MTs were polymerized in glass capillaries and labeled with taxol conjugated Oregon Green.

shown in Fig. 3.7. A typical confocal image of MT bundles is shown in Fig. 3.9, in which MT bundles are green. Although these bundles appear as loosely packed aggregates of parallel microtubules (because bundles were disturbed during pipeting and subsequent pressing on the cover slide), it is highly likely that microtubule bundles inside striped patterns are much more tightly packed, as demonstrated later in the discussion of the mechanical buckling model.

It has been reported that bundling transitions of filamentous biopolymers such as DNA, F-actin and MTs can be induced by either electrostatic or steric interaction [91]. The electrostatic interaction stems from the polyelectrolyte nature of these biopolymers [91], which gives rise to nonspecific binding by ligands carrying opposite charges including counterions. At sufficiently high concentration of counterions of appropriate valency, typically divalent or higher, a net attractive interaction can occur, leading to the subsequent lateral aggregation. The steric interaction refers to a distinct physical mechanism known also as depletion attraction to colloidal scientists or macromolecular crowding in the biochemistry literature [58]. It has been theoretically predicted and experimentally shown that rigid filaments coexisting with a crowded solution of inert polymers or globular proteins may spontaneously coalesce into bundles [58, 50].

Both interactions discussed above are likely relevant to the bundle formation of MTs in this study. MTs are known to be highly negatively charged, and are surrounded by counterions, particularly the divalent Mg^{2+} ions existing in millimolar concentration. The counterions significantly screen the negatively charged MTs, reducing the mutual repulsion between them. Theoretical work over the past decades has predicted attractive interactions due to correlations of counterions shared by parallely aligned rods of like charge [73, 83]. Experimentally, MTs have been observed to form bundles in the presence of divalent and multivalent cations [92, 67]. As an additional factor, unpolymerized tubulin dimers, oligomers and even short MTs may serve as "inert" macromolecules, which facilitate the lateral aggregation of parallely aligned MTs via the steric interaction. Indeed, MTs have been shown to form bundles of different morphologies in the presence of inert macromolecules [68].

We speculate that MT bundle formation in our system is due to the combined effects of counterion induced attraction and depletion force. The 2 mM divalent counterion Mg^{2+} present in the MT solutions may be insufficient to induce substantial bundling alone. Combining its effect with the depletion attraction, however, and given the fact that the polymerizing MTs are concurrently being aligned by external forces, bundling becomes the likely outcome. In fact, experimental evidence of spontaneous bundling of MTs has been given by Hitt *et al.* [46]. In this study, we confirm the previous report and show that bundling of MTs is a key step towards developing the striated patterns.

3.3 Small angle x-ray scattering experiments and data analysis

Small angle x-ray scattering (SAXS) is a technique where the elastic scattering of x-rays (wavelength 0.1 to 0.2 nm) by a sample is recorded at very low angles (typically 0.1^o - 10^o). This angular range contains information about the shape and size of macromolecules, characteristic distances of partially ordered materials, pore sizes, and other data. SAXS is capable of delivering structural information of macromolecules between 5 and 25 nm, of repeat distances in partially ordered systems of up to 150 nm [40].

In the case of biological macromolecules such as proteins, the advantage of SAXS is that a crystalline sample is not needed. However, due to the random orientation of dissolved or partially ordered molecules, the spatial averaging leads to a loss of information in SAXS. In this study, we used SAXS to study the scattering of microtubule bundles. The x-ray source was synchrotron beam at Brookhaven National Laboratory. To prepare sample for measurements, 5 mg/ml tubulin was polymerized in eppendorf tubes and injected into a 1.5 mm diameter cylindrical x-ray tube. The wavelength of x-ray is 0.776 angstrom, and the data acquisition time is 10 minutes.

In a typical SAXS experiment, a monochromatic beam of x-rays is brought to a MT sample from which some of the x-rays scatter, while most simply go through the sample without interacting with it. The scattered x-rays form a scattering pattern which is then detected by a detector positioned behind the sample perpendicular to the direction of the primary beam that initially hit the sample. The scattered intensity I(q) is recorded as a function of momentum transfer q (q=$4\pi\sin\theta/\lambda$, where 2θ is the angle between the incident and scattered beam.

Fig. 3.10 shows a typical scattering pattern, the brightness indicates the scattering intensity. The random positions and orientations of MTs result in an isotropic intensity distribution. Fig. 3.11 plots the scattering vector q versus the logarithm of the scattering intensity (azimuthally averaged).

The scattering pattern is close to that of a dilute solution of MTs. The peaks correspond to the Fourier transform of the MT cylinder if we compare Fig. 3.11 with Fig. 3.12. We do not see peaks corresponding to packing of MTs in bundles if we compare Fig. 3.11 with Fig. 3.13 and other scattering plots of MT bundles in the literature [67, 68, 69]. Therefore, we speculate that most MTs are dispersed in the samples tested and the scattering from small fraction of bundles was smeared by the scattering from single MTs. The low extent of bundle formation here as compared with that in striated patterns was probably due to lack of alignment factors such as convection and magnetic fields during polymerization.

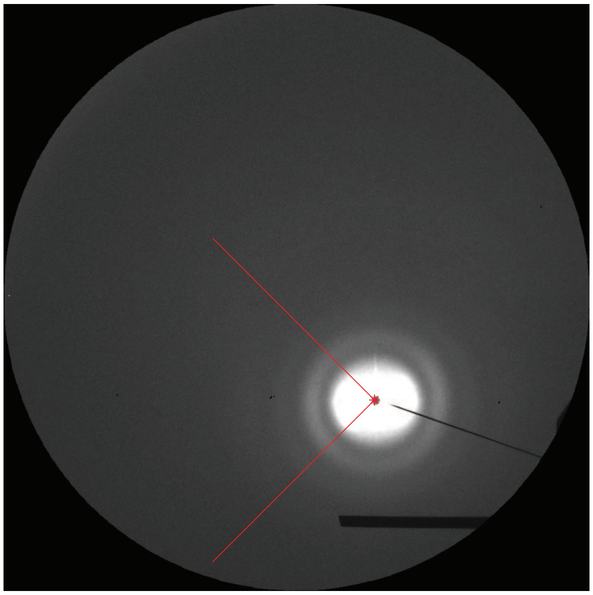

Figure 3.10: Scattering pattern from a SAXS scan. The scattering pattern contains the information on the structure of the sample. The solvent scattering has been subtracted. Different rings around the axis of the initial incident beam represent different scattering angles θ. The scattering intensity I(q) at each scattering angle was averaged over the region between the two red lines. The brightest region in the center is where the strong main beam (containing unscattered beam) hit.

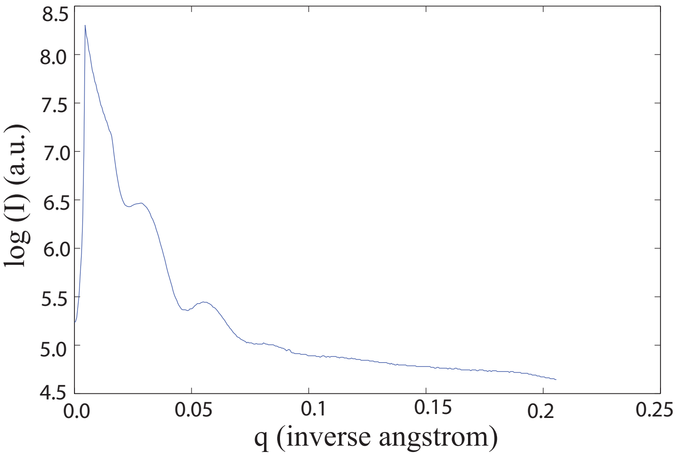

Figure 3.11: Plot of logarithm of scattering intensity log(I) versus scattering vector q. The peak positions are at 0.0046, 0.028, 0.057, 0.084 inverse angstrom, respectively.

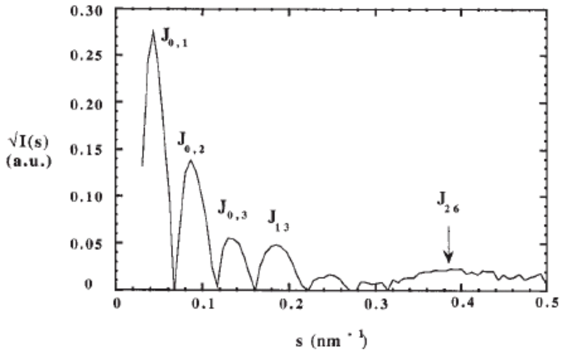

Figure 3.12: Scattering from oriented solution of hydrated MTs [16]. The value of q for the first peak is at 0.027 inverse angstrom, the second peak is at 0.055 inverse angstrom, the third peak is at 0.084 inverse angstrom. All these three peaks correspond to Fourier transform of the MT cylinder.

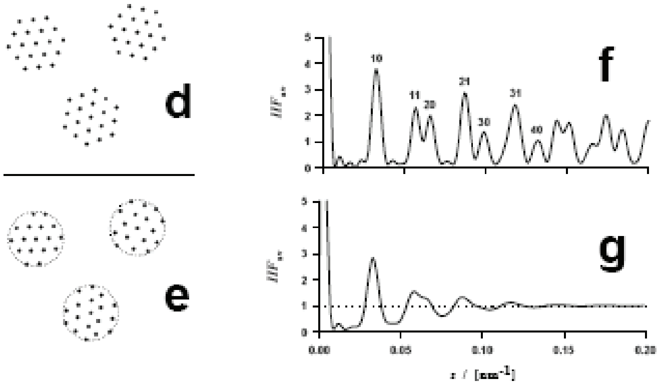

Figure 3.13: Theoretical interparticle interference function [62]. d and f corresponds to arrays of finite size with perfect hexagonal symmetry corresponding to regular bundles of 19 microtubules; e and g corresponds to finite paracrystals in two dimensions corresponding to bundles of microtubules (about 20 MTs per bundle) with deviations from hexagonal arrangement.

3.4 Birefringence measurement, phase contrast and fluorescence imaging of striated patterns

We use birefringence measurement, phase contrast and fluorescence imaging to study the microscopic characteristics of striated patterns. Fig. 3.14A, Fig. 3.15A, Fig. 3.15B shows a typical PolScope, phase contrast and fluorescence image of the striated pattern respectively.

Both the solution retardance magnitude and the slow axis orientation of MTs vary in space (see Fig. 3.14A). The retardance values and the MT slow axis orientations along the white line in Fig. 3.14A are plotted in Fig. 3.14B and Fig. 3.14C, respectively. Note that the retardance is higher in the sloped regions and lower in the peak and valley regions of the waves. Similar to the retardance, the fluorescence intensity undulates in space as shown in Fig. 3.15B. The wave-like striations in the phase contrast image are due to MT bundles (single MTs are not resolvable using phase contrast microscopy) undulating in a wave-like manner, which give rise to macroscopic birefringence stripes between crossed polarizers.

3.4.1 Quantitative analysis of periodic variations in birefringence and fluorescene intensity

Concurrent undulations in the retardance and fluorescence intensity of labeled MTs are apparent as mentioned in the previous paragraph. These undulations have half

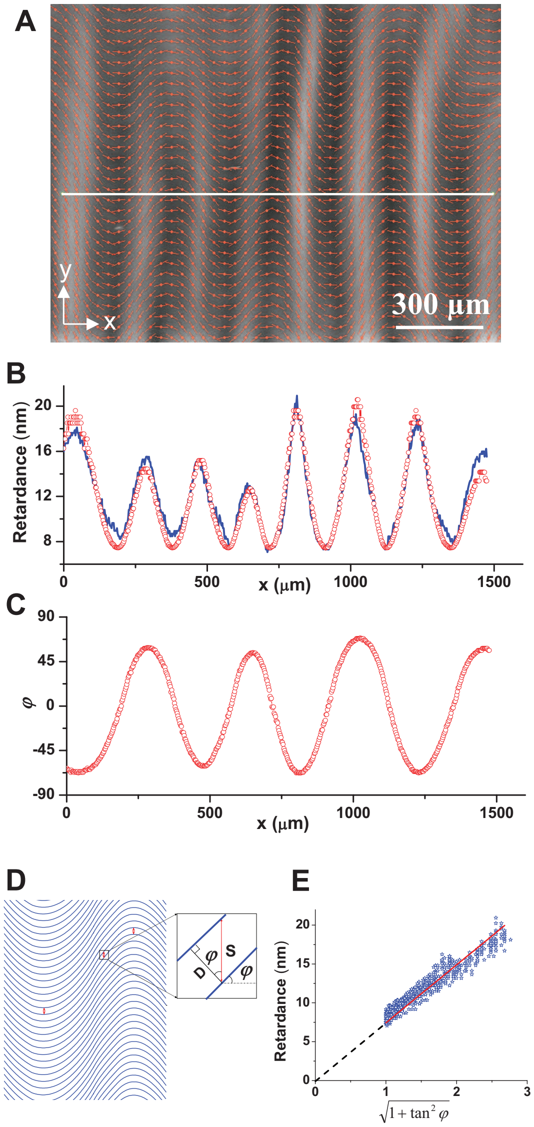

Figure 3.14: Quantitative analysis of the striped patterns based on birefringence measurements [57]. (A) PolScope measurement of a typical sample self-organized in 3.3 mg/ml tubulin solution (taxol-Oregon Green added for fluorescence imaging performed on the same sample). The solution in a 0.4 mm thick cuvette was initially exposed to a 9 Tesla magnetic field for 30 min. The measurement was done after the pattern was stable. The brightness indicates the magnitude of retardance and the pins show slow axis orientations. (B) Retardance values along the white line in A (blue curve) and fit (red curve) using $\Delta(x) = \Delta_0 \sqrt{1+\tan^2\varphi(x)}$. The x axis starts from the left end of the white line in A. The slow axis orientations φ are measured values as shown in C. The only fitting parameter is Δ_0. (C) Slow axis orientations along the same line. (D) Schematic showing that the packing density is proportional to $\sqrt{1+\tan^2\varphi}$ for nested MT bundles (each curve represents a bundle). (E) Retardance along the white line in A and fit proportionally to $\sqrt{1+\tan^2\varphi}$, where φ is the slow axis direction at each corresponding position. This figure is taken from [57].

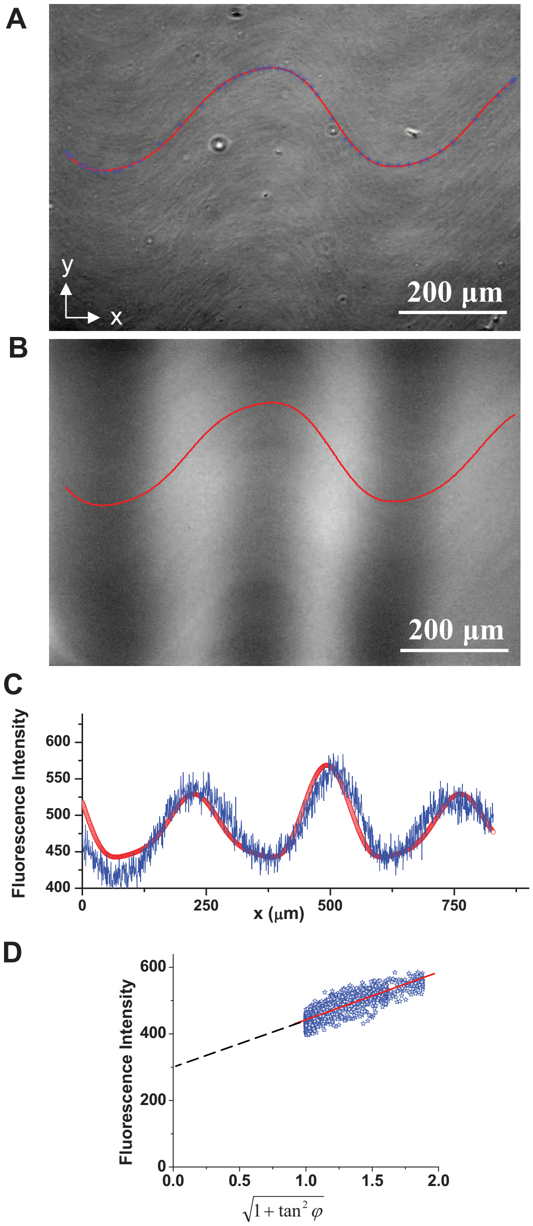

Figure 3.15: Quantitative analysis of the striped patterns based on fluorescence measurement [57]. (A) Phase contrast image (contrast enhanced) of the same region as in Fig. 3.14 but with a smaller field of view. Blue points are manually picked up along a MT bundle. The red curve is a fit to the shape of the bundle using the sum of three sinusoidal functions. (B) Fluorescence image of the same region, the red curve is the same as in A. (C) The blue curve is a plot of the fluorescence intensity along the red curve in B as a function of the horizontal axis, x. The red curve is a fit using $I(x) = I_b + I_0\sqrt{1+\tan^2\varphi(x)}$, witch yields $I_b = 299$ and $I_0 = 143$. Here $tan\varphi(x)$ corresponds to the calculated slope of the contour of the bundle based on the fit to its shape. (D) Linear fit of fluorescence intensity to $\sqrt{1+\tan^2\varphi}$ using data from C. The non-zero intercept of the line with the ordinate implies a background fluorescence caused by dispersed MTs. This figure is taken from [57].

the spatial period of the wavy bundles and indicate how the MT density varies.

The nesting of buckled bundles accounts for the observed retardance and fluorescence intensity variations. As shown schematically in Fig. 3.14D, bundles of MTs buckle into a wave-like shape and nest with their neighbors. We assume that the transverse bundle displacement, S, is independent of the horizontal position, x. The local packing density of bundles (number of bundles per μm^2), P, however, depends on x through φ(x) as:

$$P \propto \frac{1}{D} = \frac{1}{S\cos\varphi} = \frac{1}{S}\sqrt{1 + tan^2\varphi(x)} \tag{3.1}$$

where φ is the local angle of the MT bundles measured relative to the original alignment direction. As the retardance magnitude is proportional to the packing density of aligned filaments [43, 81], it is expected to follow $\Delta(x) = \Delta_0\sqrt{1 + \tan^2\varphi(x)}$. To test this expectation, the measured Δ in Fig. 3.14B is plotted against $\sqrt{1 + \tan^2\varphi}$ in Fig. 3.14E. These data are consistent with the expected proportional relationship and a fit yields Δ_0=7.44 nm.

The nesting of buckled bundles also accounts for the coexisting fluorescence intensity variations. The fluorescence intensity contributed by MTs aligned in the bundles is also expected to follow $I \propto \sqrt{1 + tan^2\varphi}$. Unlike the retardance, however, there is an additional background contribution, I_b, which is due to dispersed MTs. These MTs are most likely randomly oriented as they do not contribute to birefringence. To test these expectations, we use a typical phase contrast image (Fig. 3.15A) to follow the contour of a bundle (i.e., to determine $\varphi(x)$ along the bundle). The blue points were picked along a discernible bundle and their positions were fit to a simple Fourier expansion with three sinusoidal terms. The measured fluorescence intensities along the red fitted curve in Fig. 3.15B are plotted as the blue curve in Fig. 3.15C versus the horizontal position, x. The red curve in Fig. 3.15C is a fit to $I(x) = I_b + I_0\sqrt{1 + \tan^2\varphi(x)}$ which yields $I_b = 299$ and $I_0 = 143$ (see also Fig. 3.15D), where $I(x)$ is the total fluorescence intensity and $\tan\varphi(x)$ is the calculated corresponding slope of the bundle based on the fit to its shape.

3.5 Decomposition of the pattern structure into MT bundles and dispersed MTs in the network

It is known that taxol binds tightly and specifically to MTs (see, for example, [47]). Thus the measured fluorescence signal mainly comes from MTs incorporated into bundles and in the surrounding network. To validate this assertion, we centrifuged a solution of fluorescent taxol labeled MTs and measured the fluorescence signal of the supernatant. The signal after sedimenting MTs was less than 3% of the original solution (data not shown), confirming that the contribution to the fluorescence signal from free fluorescent taxol and any fluorescent taxol bound to either tubulin dimers or short fragments of MTs that do not sediment is negligible.

Using the background and the average total fluorescence intensity, I_b and $\bar{I}$, respectively, we calculated the fraction, η, of MTs incorporated into the nested bundles after the pattern became stable. For the sample presented in Fig. 3.15, $\bar{I} = 485$ (see Fig. 3.15C),

$$\eta = \frac{\bar{I} - I_b}{\bar{I}} = \frac{485 - 299}{485} = 38\% \tag{3.2}$$

where $\bar{I} - I_b$ is the contribution from MTs incorporated into the bundles. These calculations demonstrate that only a fraction of MTs forms the undulating bundles. The other fraction of MTs exist in a non-birefringent, isotropic network based on the fact that there is no background retardance (see Fig. 3.14E).

3.6 Estimation of MT bundle size and bending energy based on retardance measurement

We estimate the average number of MTs in the cross section of a bundle from the retardance image shown in Fig. 3.8A. The retardance signal of a single MT has a peak of 0.07 nm and a spread of 0.17 μm [72, 51]. The average retardance in Fig. 3.8A is about 2 nm.

So, the number of MTs in Fig. 3.8B which has a width of about 150 μm can be obtained as follows:

$$N_{MT} = \frac{2nm \times 150\mu m}{0.07nm \times 0.17\mu m} = 25,210$$

The total number of bundles in Fig. B is estimated to be about 100, so each bundle contains

$$n_2 = \frac{N_{MT}}{100} = \frac{25,210}{100} = 252\, MTs/bundle$$

The bundle radius can be calculated as follows:

$$\begin{aligned} \frac{\pi R^2}{\pi(12nm)^2} &= 250 \\ \Longrightarrow R &= 16 \times 12nm \\ \Longrightarrow R &= 192nm \end{aligned}$$

Assuming the shape of the bundle is $y = a\lambda \sin\frac{2\pi x}{\lambda}$ $(a = \frac{1}{2})$, the bending energy of all the MTs in a 5 mg/ml solution in a cuvette with sizes $8mm \times 0.4mm \times 40mm$ is:

$$
\begin{aligned}
E_{MTs} &= \frac{L}{L_{per\,wavelength}} \times E_{MT,per\,wavelength} \\
&= \frac{L}{L_{per\,wavelength}} \times \frac{k}{2}\int_0^\lambda \rho^2 ds \\
&= \frac{L}{\int_0^\lambda \sqrt{1+y'^2}dx} \times \frac{k}{2}\int_0^\lambda \frac{y''^2}{(1+y'^2)^3}\sqrt{1+y'^2}dx \\
&= \frac{L}{\lambda} \times \frac{k}{\lambda} \times \{\frac{8a^2\pi^4}{\int_0^1 \sqrt{1+4a^2\pi^2\cos^2 2\pi t}dt} \times \int_0^1 \frac{\sin^2 2\pi t}{(1+4a^2\pi^2\cos^2 2\pi t)^{5/2}}dt\} \\
&= Constant \times \frac{L}{\lambda^2} \times \frac{\pi}{4}ER^4 \\
&= 11.1 \times \frac{1.64 \times 10^7 \times 40mm}{(600\mu m)^2} \times \frac{\pi}{4} \times 1.2 \times 10^9 pa \times (12nm)^4 \\
&= 3.95 \times 10^{-10} J \\
&= 9.55 \times 10^{10} K_B T
\end{aligned}
$$

Here L is the length of the cuvette, 1.64×10^7 is the total number of MTs in a 5 mg/ml solution in the cross section of a cuvette with sizes $8mm \times 0.4mm \times 40mm$ (assuming each MT has a length of L and the critical concentration of polymerization is 1 mg/ml). On the other hand the energy released by GPT hydrolysis can be estimated as follows:

$$
\begin{aligned}
E_{GTP} &= 2mM \times 8mm \times 0.4mm \times 40mm \times 6.02 \times 10^{23} \times 10K_B T \\
&= 1.6 \times 10^{18} K_B T
\end{aligned}
$$

Therefore, energy provided by GTP hydrolysis is enough for buckling to occur.

3.7 Time evolution of retardance, bundle length and buckling wavelength

Time lapse phase contrast microscopy reveals that MT bundles elongate uniformly along their contour during buckling, which is consistent with polymerization occurring uniformly along the bundles. Bundle elongation is illustrated in the phase contrast images Fig. 3.16(a) and Fig. 3.16(b), showing a fixed region taken 12 and 100 min after polymerization initiation, respectively. The three white curves in each image are computer generated traces of bundle contours that extend between selected fiducial marks. The fiducial marks are visible as dark spots. To generate the white curves, we presumed that the bundles followed the striations and traced the stripes between the fiducial marks. The marks were tracked by MetaMorph (Universal Imaging, West Chester, PA). We determined the local striation orientation at each pixel by calculating a Fast Fourier Transform (FFT) of the area around the pixel, shown, for example, in Fig. 3.16(c). The FFT appeared as an elongated spot oriented perpendicular to the striation direction [Fig. 3.16(d)]. The radially integrated FFT intensity has a peak at a specific azimuthal angle [Fig. 3.16(e)] that is perpendicular to the striation orientation. In this way, the lengths of three segments along a MT bundle were recorded every 30 seconds and plotted in Fig. 3.16(f), (g) and (h). The normalized lengths of these three segments grew at nearly the same, constant rate, shown in Fig. 3.16(i), implying that the MT bundles elongate uniformly along their contour

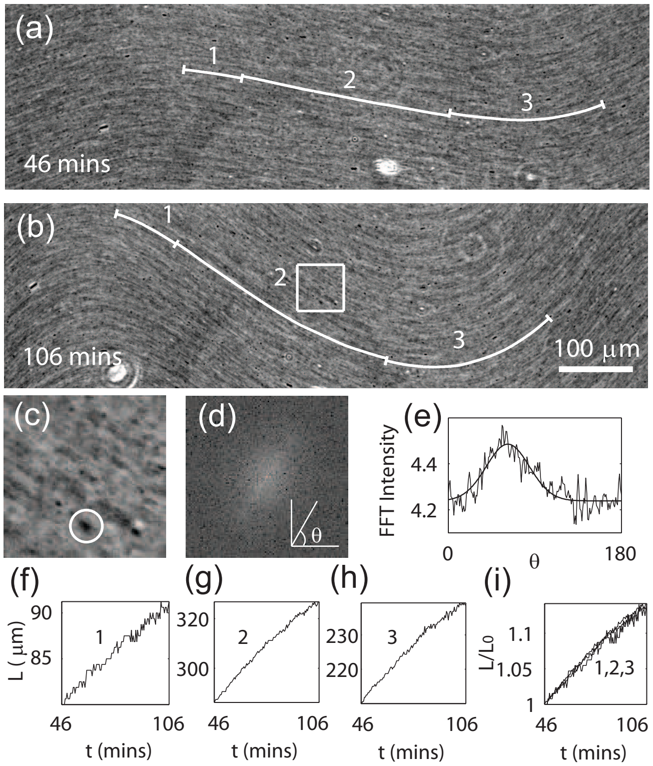

Figure 3.16: Illustration and measurements of the uniform elongation of MT bundles [1]. (a),(b) Phase contrast images of a sample region, showing progression of the pattern over 1 h. MT bundles are discerned by the thin striations. Segments 1 through 3 are adjacent pieces of a contour followed by bundles. The segment ends are defined by fiducial marks. (c) Magnified view of the region denoted by the white box in (b), showing an encircled fiducial mark. (d) Fast Fourier Transform (FFT) of (c). (e) The radially averaged FFT intensity plotted versus the azimuthal angle θ and fit using a Gaussian function. The local bundle orientation is orthogonal to the angle at which the Gaussian fit peaks. (f)-(h) Length of segments 1 (f), 2 (g), 3 (h) as a function of time. (i) Lengths of the three segments as a function of time, normalized to their lengths at 46 min. This figure is taken from [42].

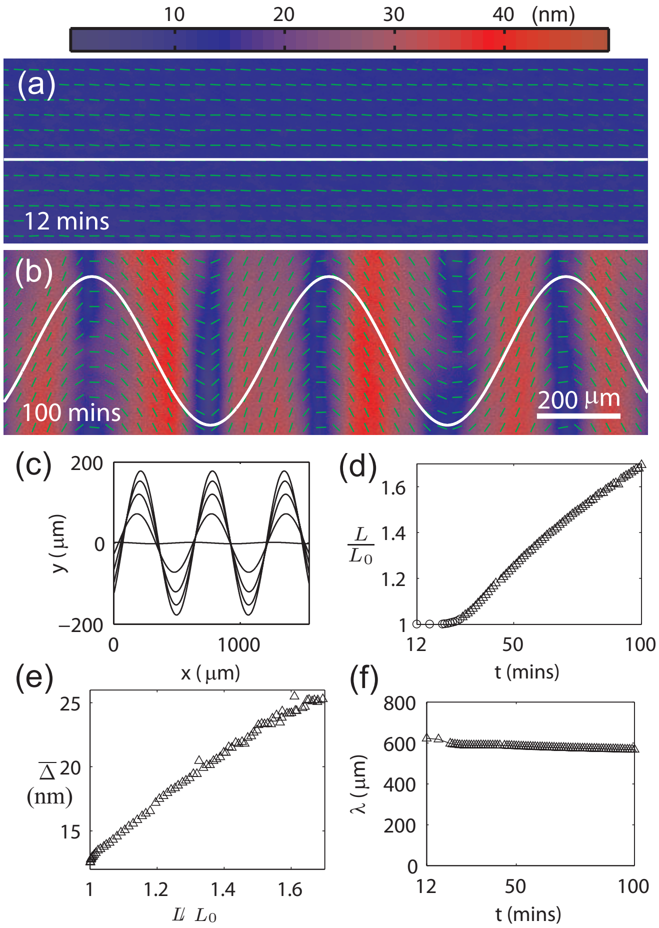

Figure 3.17: Time evolution of a MT pattern obtained by measuring the retardance and slow axis of the sample using a PolScope imaging system [2]. (a),(b) Retardance images of a sample region at 12 and 100 min of self-organization, respectively. The color bar shows the retardance magnitude scale and the green pins provide the slow axis orientation. The straight white lines represent the slow axis line scan position. (c) Slow axis line scan (black) and the fitted slow axis orientation $\varphi(x) = \arctan\{A\frac{2\pi}{\lambda}\cos[\frac{2\pi}{\lambda}(x+x_0)]\}$ (red) at 100 min. (d) The dominant buckling wavelength λ, obtained from the fitted shapes of the bundle at individual time points. (e) The length evolution of the fitted bundle contour. $L_0 = 1544\,\mu$m is the initial unbuckled length of the bundle. The segment before the arrow designates the latent period prior to the onset of the buckling. (f) The magnitude of the retardance averaged over the line as shown in (a) versus the normalized length L/L_0. This figure is taken from [42].

instead of growing solely at their ends. It further suggests that the bundles elongate through polymerization of their constituent MTs, which start and end at random places along a bundle. The uniform growth of all MTs within a bundle justifies a uniform compressional force throughout the bundle during buckling.

Additional quantitative information about the microscopic picture of the buckling is gained through time-lapse birefringence measurements. PolScope images, taken sequentially at a fixed sample region [2], yielded the time evolution at each pixel of both the retardance ($\Delta \equiv \text{birefringence} \times h$, where h is the sample thickness) and slow axis direction [$\varphi(x)$, orientation of MT bundles]. Two representative PolScope images of a single region taken at different stages of self-organization are shown in Fig. 6.2(a) and 6.2(b). The slow axis variation, $\varphi(x)$, along the white lines in Fig. 6.2(a) and 6.2(b) can be fit to $\varphi(x) = \arctan\{A\frac{2\pi}{\lambda}\cos[\frac{2\pi}{\lambda}(x + x_0)]\}$, indicating that the bundle follows $\xi(x) = A\sin[\frac{2\pi}{\lambda}(x + x_0)]$ with a single wavelength λ, buckling amplitude A, and offset x_0 [Fig. 6.2(c)]. The resultant wavelength, $\lambda \approx 600\,\mu\text{m}$, is plotted in Fig. 6.2(d). The normalized contour length calculated from the fits, $L(t)/L_0$, grew nearly linearly with time at a normalized rate of $\dot{L}(t)/L_0 \approx 1\,\%$ per min [Fig. 6.2(e)]. Simultaneously, the retardance magnitude averaged over the white line in Fig. 6.2(a) increased roughly in proportion to $L(t)/L_0$ [Fig. 6.2(f)]. Based on the nesting model we proposed earlier and assuming that neighboring MT bundles do not coalesce, the average retardance goes as $\overline{\Delta}(t) \sim \delta \times n(t)L(t)/L_0$ [57, 72], where $n(t)$ is the number of MTs in the cross section of a bundle and δ is the retardance of a single MT.

Therefore, the linear relation between $\overline{\Delta}(t)$ and $L(t)/L_0$ implies that $n(t)$ remains constant throughout buckling. Thus, the elongation of MT bundles occurs through the polymerization of MTs within the bundles and does not involve the incorporation of new MTs to existing bundles.

Chapter 4

Mechanism of Striped Pattern Formation and a Mechanical Buckling Model

4.1 Mechanism of striped birefringence pattern formation

We propose a two-stage mechanism for the stripe formation: polymerizing MTs align uniformly along the direction of external magnetic fields or convective flow and form bundles in the early stage; the bundles grow uniformly due to the elongation of constituent MTs and eventually buckle and nest into a wave-like shape in the later stage. The two-stage mechanism for the stripe formation not only involves the chemical and biological reaction of MT polymerization and bundle formation, but also incorporates a mechanical component of buckling of growing MT bundles. This mechanism might account for some large scale phenomena in biological morphogenesis and provide a basis for further experimental and theoretical work.

4.2 Estimation of buckling wavelength based on minimization of energy

We estimate the characteristic wavelength of buckling by minimizing the sum of bending energy of the bundles, the elastic energy of the MT network surrounding the bundles and the compressional energy of the bundles. We assume that buckling arises once the compressional strain of a growing MT bundle exceeds a critical value and the characteristic wavelength is selected at the onset of the buckling instability with the critical strain. We consider MT bundles as homogeneous elastic rods, the buckling of which costs bending energy. The MTs incorporated into bundles are not the only population of MTs in the system (see Eq. 3.2), but there exists another population of MTs which form an elastic MT network. Thus, buckling of the bundles involves an elastic deformation of the surrounding MT network and induces an elastic energy to the network. We assume that the elastic restoring force applied by the network on the bundle per unit bundle length, F, is proportional to the displacement of the bundle in the transverse direction, $\xi(x)$, as: $F(x) = \alpha\,\xi(x)$, where α is the elastic constant of the network per unit length along the bundle. The actual mode of buckling is selected by minimizing the sum of the bundle bending and compressional energy and the network elastic energy. The bending energy scales approximately as:

$$E_{bending} \;=\; \frac{\kappa}{2}\int_0^\lambda \rho^2 \frac{d}{\lambda}\, ds$$

$$\approx \frac{\kappa}{2}\frac{8\pi^4\delta^2}{\lambda^3}\frac{d}{\lambda}$$

$$= ER^4\pi^5\frac{\delta^2 d}{\lambda^4}$$

where κ is the bending stiffness of the bundle, E is the Young's modulus of the bundle, d is the end to end distance of the bundle, R is the radius of the bundle and δ is the amplitude of buckling, which is much smaller than λ at the onset of buckling. The elastic energy of the network scales as:

$$E_{elastic} = \frac{1}{2}\alpha\frac{\delta^2}{2}d = \frac{\alpha}{4}\delta^2 d$$

i.e., $E_{elastic} \propto \alpha\,\delta^2$. The bundle compressional energy is calculated as follws:

$$E_{compression} = \frac{1}{2}k_{bundle}\epsilon^2 L^2 = \frac{1}{2}\frac{EA}{L}\epsilon^2 L^2 = \frac{1}{2}EA\epsilon^2 L$$

where k_{bundle} is the spring constant of the bundle, ϵ is the strain, L is the bundle length and A is the cross sectional area of the bundle. The constraint of a fixed contour length of the bundle dictates that

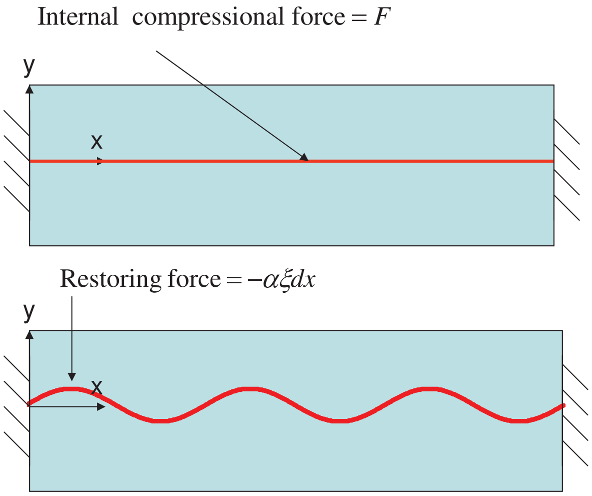
Internal compressional force = F
y
x
Restoring force = $-\alpha\xi dx$
y
x

Figure 4.1: Schematic drawing to illustrate the elastic buckling model.

$$\int_0^{\lambda} \sqrt{1+y'^2}\,\frac{d}{\lambda}\,dx \approx (1+\frac{\pi^2\delta^2}{\lambda^2})d = const$$

i.e., $\delta \propto \lambda$. Thus $E_{bending} \propto \frac{E\,R^4}{\lambda^2}$, $E_{elastic} \propto \alpha\,\lambda^2$ and $E_{compression}$ is not dependent on buckling wavelength. Minimization of $E_{bending} + E_{elastic} = \frac{E\,R^4}{\lambda^2} + \alpha\,\lambda^2$ leads to $\lambda \propto \sqrt[4]{\frac{E}{\alpha}}\,R$. This scaling result suggests that the buckling wavelength has a weaker dependence on E and α as compared to the dependence on R.

4.3 The mechanical buckling model

We propose an elastic buckling model based on the equation of motion of buckling MT bundles to illustrate the buckling phenomenon. We model MT bundles as nested elastic rods (see Fig. 4.1), which buckle against an elastic surrounding network. Let us first consider buckling of a single rod and then compare it with the buckling of multiple rods. It is known that buckling of a single rod against a fixed point by an applied force along its long axis will give rise to Euler buckling, i.e., buckling with half a wavelength. In the case of MT bundles, however, they are not separated but inter-correlated with a dense MT network in the surrounding area between the bundles. Euler type of buckling requires much distortion of the network, thereby increasing the elastic energy of the network. On the other hand, buckling with several bends will reduce the amount of distortion and stabilize the system. To describe the effect of the surrounding medium on buckling, we consider a single bundle in the center of the sample and characterize its interaction with the network using a single elastic constant, α, such that $\alpha\xi(x)$ is the elastic restoring force exerted by the network on the bundle per unit length (see Fig. 4.1), where $\xi(x)$ is the bundle displacement in the y direction. Treating the bundle as a rod with a bending rigidity, K, under a compressional force, F, the force balance in the y direction at the onset of the buckling is given by [15, 38, 52].

$$K\frac{\partial^4\xi(x)}{\partial x^4} + \frac{\partial}{\partial x}[F\frac{\partial\xi(x)}{\partial x}] + \alpha\xi(x) = 0 \tag{4.1}$$

Standard normal mode stability analysis of Eq. (4.1), assuming $\xi(x) \propto e^{ikx}$ and a uniform F, yields $F = \alpha/k^2 + Kk^2$. This result suggests a critical compressional force $F_c = 2\sqrt{K\alpha}$ for a buckling solution and a characteristic wavelength

$$\lambda_c = 2\pi/k = \pi\sqrt{8K/F_c} = 2\pi\sqrt[4]{K/\alpha} \tag{4.2}$$

The resultant characteristic wavelength [Eq. (4.2)] agrees with the prediction for λ_c based on energy minimization. This model predicts buckling in a higher mode than the fundamental one as in the classic Euler buckling.

In agreement with experiments, this model implies that the orientation of MT bundles in a striped sample varies continuously in space in a wave-like manner. In contrast, previous models had suggested that discrete and alternate angular orientations of the MTs formed the striated patterns [89]. In addition, the weak dependence of λ_c on K and α is consistent with the small variations in both the observed wavelength across a single macroscopic sample and the patterns formed under different conditions (for example, samples with different tubulin concentrations and samples in containers with different sizes). Once the wavelength is selected at the onset of buckling, it does not change with time, in agreement with the experimental observation (see Fig. 3.17d).

Two limits exist for elastic properties of the bundle (K). If tight packing (solid model) of the MTs inside the bundle is assumed, then $K_{\text{solid}} = n^2 K_{\text{MT}}$, where $K_{\text{MT}} \approx 3.4 \times 10^{-23}\, N \cdot m^2$ is the bending rigidity of a single MT [27, 96]. If MTs slide freely inside the bundle, then $K_{\text{slip}} = nK_{\text{MT}}$. By plotting the wavelength over a reasonable range of individual MT lengths for both models[42], we found that the solid model for K appears more reasonable than the slip model, in agreement with previous assumptions, which yield a wavelength comparable to experimental measurements. The fact that K depends quadratically on n in our system suggests that MTs are fully coupled (acting like a solid material) inside the bundle, similar to the behavior of F-actin bundles held together through depletion forces [22].

4.3.1 Buckling force

The occurrence of buckling implies that a longitudinal compressional stress builds up within the MT bundles. The concomitant elongation of the bundles during buckling suggests that this stress most likely results from polymerization forces exerted by individual MTs. Other known force generation mechanisms in MT systems require molecular motors, which are absent from these solutions. Thus, we are led to the picture that the individual MTs in a bundle continue to polymerize and, once encountering boundary confinements imposed by adjacent bundles and/or cuvette walls, generate a longitudinal compressional force within the bundle. The compressional force induced by polymerization increases while MTs keep growing. When the force exceeds a critical value, the bundles start to buckle. In addition this force keeps constant during the process of buckling, consistent with the fact that the elongation rate of MT bundles during buckling is constant (see 3.17f, g and h).

4.4 Numerical estimates about buckling wavelength

Recall from previous discussions that the critical buckling wavelength $\lambda_c = 2\pi \sqrt[4]{K/\alpha}$, where K is the bending stiffness of MT bundles and α is the elastic constant of the

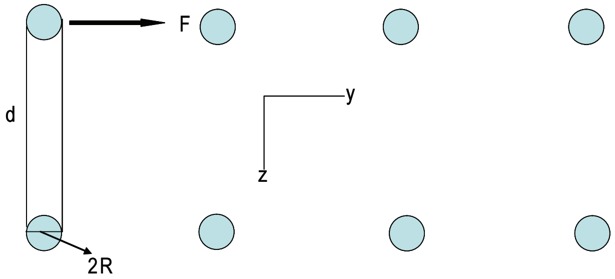

Figure 4.2: A schematic showing an array of bundles embedded in an elastic medium. The blue circles represent the cross sections of representative bundles with a spacing of d. The diameter of each bundle is 2R. F indicates the force exerted on the bundles by the surrounding elastic network, which is assumed to be linear with the extent of buckling ξ as: $F = \alpha\xi\, dx$. Here α is the elastic constant of the surrounding medium and dx represents unit bundle length. The stress σ is: $\sigma = \frac{F}{2R\,dx}$, and strain γ can be written as: $\gamma = \frac{\xi}{d}$. Therefore, shear modulus G' can be calculated as $G' = \frac{F d}{\xi 2R\,dx} = \frac{\alpha\xi\,dx\,d}{\xi 2R\,dx} = \frac{d}{2R}\alpha$. So α is related to G' as $\alpha = \frac{2R}{d}\,G' = \sqrt{\eta}\,G'$, where η is the volume fraction of bundles.

surrounding MT network. In order to obtain a numerical estimate of the wavelength, we need to estimate K and α. The relation between the bending rigidity of a single MT (k) and the Young's modulus of single MT (E) is:

$$\begin{aligned} k &= EI \\ &= E\frac{\pi}{4}r^4 \end{aligned}$$

So,

$$\begin{aligned}
E &= \frac{k}{I} \\
&= \frac{4k}{\pi r^4} \\
&= \frac{4 \times 3.4 \times 10^{-23}}{3.14 \times (12 \times 10^{-9})^4} \\
&\approx 2 \times 10^9 \, Pa
\end{aligned}$$

Here r is the radius of a single MT. We assume that the Young's modulus of a MT bundle is about the same order of magnitude as that of a single MT (solid model). The spring constant of the network per unit length, α, is proportional to the elastic shear modulus of the network in the following way: $\alpha \sim \frac{2R}{d} G' \approx \sqrt{\eta}\, G' \approx \sqrt{1.36 \times 10^{-3}} \times 10 \, Pa \approx 0.4 \, Pa$ (see Fig. 4.2), where R is the radius of the bundle, d is the lateral spacing between adjacent bundles, G' is the elastic shear modulus, which is typically in the order of 10 Pa and η is the volume fraction of bundled MTs, which is about 1.36×10^{-3} for 5 mg/ml MT solutions (MT protein density is about 1.4 g/cm^3). So the volume fraction for 5 mg/ml microtubule is: $\eta = \frac{5 \times 10^{-3} g/(1.4 \, g/cm^3)}{1 \, ml} = 0.36\%$. Assuming that bundles represent 38% (see Eq. 3.2) of total protein volume, the volume fraction of bundles is $0.36 \times 38\% \approx 0.136\%$). Based on the assumption that MTs are close to tight packing inside a bundle (solid model), the radius of a bundle is about $\sqrt{250 \times (12 \, nm)^2} \approx 200 \, nm$ where 250 is the number of MTs in a bundle and 12 nm is the radius of a single MT. Therefore, an estimation for the characteristic wavelength is: $\lambda_c = 2\pi \sqrt[4]{K/\alpha} = \sqrt{2}\, \pi^{5/4} \sqrt[4]{\frac{E}{\alpha}}\, R \approx 6 \times \sqrt[4]{\frac{1 \, GPa}{0.4 \, Pa}} \times 200 \, nm \approx 300 \, \mu m$, which is comparable to the experimentally observed buckling wavelength (see Fig. 3.14A).

Part II

Optical Tweezers and Its Applications in Microrheology and *Caulobacter* Motility and Adhesion

Chapter 5

Introduction to Optical Tweezers and Microrheology

5.1 How optical tweezers work

It was discovered that light intensity gradient in a tightly focused laser beam could be used to trap particles by Arthur Ashkin of Bell Laboratory in 1978 [8]. These traps, also called optical or laser tweezers, allow one to manipulate micron-sized particles with light easily and reliably. They also allow one to take force measurements in the pico-newton range [4, 24, 20]. The understanding of the physical reason for trapping due to a light gradient depends on the wavelength of light used compared to the size of the object trapped.

In cases where the dimensions of the particle are greater than the laser wavelength,

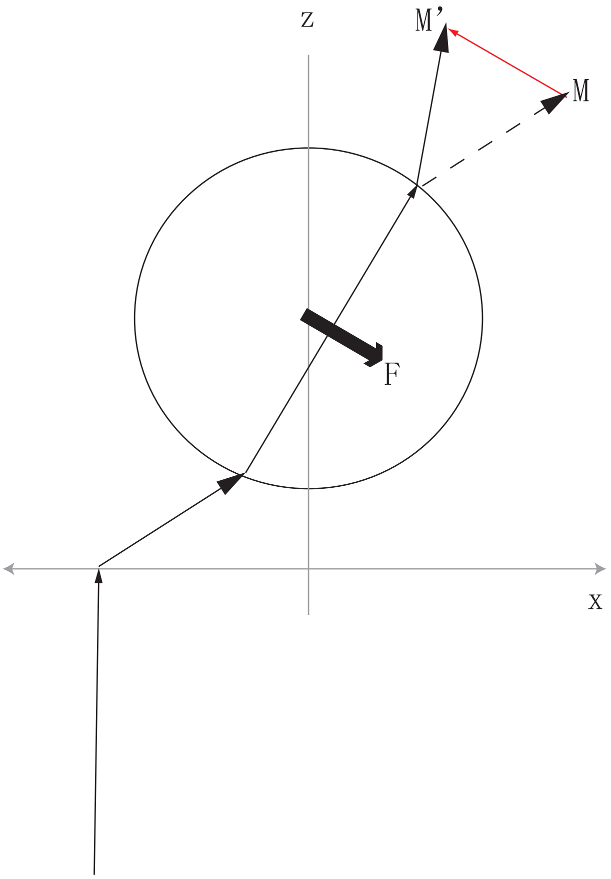

Figure 5.1: Schematic drawing to illustrate origin of optical force in the regime where ray optics can be used. The initial momentum of the light beam is denoted as M and the final momentum to each photon is denoted M' in the figure. The momentum change is represented by the red arrow. The force thus induced on the sphere points in the opposite direction, as represented by F.

a simple ray optics treatment is adequate. As shown in Fig. 5.1, a beam of light is bent by a dielectric sphere. The momentum change of the light beam is shown as the red arrow. Following Newton's third law, the object will gain momentum in the opposite direction [9]. The force induced on the particle due to bending of the beam is shown as F in Fig. 5.1. The net force on the particle is the vector sum of the forces induced by all the light beams of the incident light.

On the other hand, if the wavelength of light exceeds the particle dimensions, the particle can be treated as a point dipole in an inhomogenous electromagnetic field. The force applied on a single charge in an electromagnetic field is: $F_1 = q(E_1 + \frac{dx_1}{dt} \times B)$, where q is the charge of the particle, x_1 is the position of the particle, E_1 and B are the electric and magnetic fields at the particle position, respectively. The moment of a dipole is: $P = q(x_1 - x_2)$. Taking into account that the two charges have opposite signs, the force can be written as: $F = q(E_1 - E_2 + \frac{d(x_1-x_2)}{dt} \times B) = (p.\bigtriangledown)E + \frac{dP}{dt} \times B = \alpha[(E.\bigtriangledown)E + \frac{dE}{dt} \times B] = \alpha[\frac{1}{2} \bigtriangledown (E^2) + \frac{d}{dt}(E \times B)] \sim 0.5\alpha\nabla(E^2)$, where α denotes the electric susceptibility of the dipole. The second term in the last equality is the time derivative of a quantity that is related through a multiplicative constant to the Poynting vector, which describes the power per unit area passing through a surface. Since the total laser intensity is constant when sampling over frequencies much lower than the frequency of the laser light, which is on the order of 10^{13} Hz, the derivative of this term averages to zero. The square of the magnitude of the electric field is equal to the intensity of the beam. Therefore, the result indicates that the force on the dielectric particle, when treated as a point dipole, is proportional to the gradient of the intensity of the beam.

The narrowest point of the focused beam, known as the beam waist, is where the electric field gradient is the greatest. It turns out that a dielectric particle is attracted along the gradient to the region of the strongest electric field. By directing a monochromatic laser beam through a convex lens it is possible to create a light gradient with the ability to trap a dielectric particle.

5.2 Microrheology

Microrheology refers to studies on the elastic properties of polymer networks on micrometer scales using microscopic probes. The ability to study them with probes spanning some of the microscopic length scales that are characteristic of polymer networks (e.g., approaching the inter-chain separation or mesh size of gels) will also lead to important new insights into the microscopic basis of the macroscopic viscoelasticity of such systems. Microrheology readily allows for measuring viscoelasticity at higher frequencies, above 1 kHz or even up to MHz, because the inertia of both the probe and its embedding medium can be neglected at such small length scales [54, 76]. Depending on whether the probe particle is subject to a forced motion, microrheology can be differentiated into passive and active ones, which are introduced separately below.

5.2.1 Passive microrheology

Passive microrheology uses microscopic particles embedded in the sample and detects thermal fluctuations of those particles. More specifically, a single probe bead is observed at a time by laser interferometry in a light microscope [82]. Detection by photodiodes ensures a bandwidth of detection between about 0.1 Hz and 100 kHz [76]. Frequency-dependent shear elastic and loss moduli are determined from the fluctuations of the embedded probes.

The response function of the bead is calculated by the fluctuation-dissipation theorem. The procedure is outlined below [82]: The complex single-particle response function $\alpha(f) = \alpha^{'}(f) + i\alpha^{''}(f)$ relates the Fourier transform of the bead displacement to the Fourier transform of the force acting on the bead $\alpha(f) = x(f)/F(f)$. The fluctuation-dissipation theorem provides the link between the Power Spectral Density (PSD), $S(f) = lim_{t\rightarrow\infty}\frac{2}{t}x_t(f)x_t(f)^*$, where $x_t(f)$=$\int_{-t/2}^{t/2} x(t^{'})e^{2\pi i f(t^{'})}dt^{'}$, and the imaginary part of the response function by $\alpha^{''}(f) = \frac{\pi}{2k_BT}fS(f)$, where k_B is the Boltzmann constant, and T is the solution temperature. A Kramers-Krönig relation can then be used to calculate the real part of the response function [82], $\alpha'(f) = \frac{2}{\pi}\int_0^\infty \frac{f'\alpha''(f')}{f'^2 - f^2}df'$. Finally, the complex shear modulus is calculated using the generalized Stokes relation, $G(f) = \frac{1}{6\pi a\alpha(f)}$, where $G(f) = G^{'}(f) + iG^{''}(f)$, $G^{'}(f)$ and $G^{''}(f)$ are the elastic and loss moduli, respectively, and a is the radius of the bead. For a spherical probe particle in a purely viscous medium of viscosity η, this expression reduces to the familiar result of $G(f) = i2\pi f\eta$.

The following is a brief derivation of the Kramers-Krönig relation adapted from Toll *et al.* [93]. The response function $\alpha(t)$ (defined as displacement/force) must be zero for $t < 0$ since a system can not respond to a force before it is applied. Therefore, the Fourier transform $\alpha(f)$ is analytic in the upper half complex plane, where f is frequency. Additionally, the response of the probe particle at high frequency (infinity) vanishes because there is no time for it to respond to the force before the force has switched direction. We apply the residue theorem for complex integration to $\alpha(f)$, where both α and f are complex and f resides on the upper half plane. The integration goes as: $\oint \frac{\alpha(f)}{f-f_0}df$. The contour encloses the upper half plane at infinity, the real axis with the exception a singular pole at $f = f_0$, and a hump over the pole, leaving no poles inside, so that the integral vanishes. We decompose the integral into its contributions along each of these three contour segments. The segment at infinity vanishes since α vanishes as f goes to infinity. We are left with the segment along the real axis, and the half-circle, which yields $-i\pi\alpha(f_0)$, as predicted by the residue theorem. The sum of these two terms is zero, i.e. $\int_{-\infty}^{\infty} \frac{\alpha(f)}{f-f_0}df - i\pi\alpha(f_0) = 0$. Rearranging, we arrive at the compact form of the Kramers–Kronig relation: $\alpha(f_0) = \frac{1}{i\pi}\int_{-\infty}^{\infty} \frac{\alpha(f)}{f-f_0}df$. Finally, by splitting $\alpha(f)$ and the equation into real and imaginary parts, we obtain: $\alpha'(f_0) = \frac{1}{\pi}\int_{-\infty}^{\infty} \frac{\alpha''(f)}{f-f_0}df$ and $\alpha''(f_0) = -\frac{1}{\pi}\int_{-\infty}^{\infty} \frac{\alpha'(f)}{f-f_0}df$.

The Kramers–Kronig relation implies that observing the dissipative response of a system is sufficient to determine its in-phase (reactive) response, and vice versa. For reconstructing physical responses, we note that in most systems, the positive frequency-response determines the negative-frequency response because $\alpha(f)$ is the Fourier transform of a real quantity, so $\alpha(-f) = \alpha^*(f)$. This means α' is an even function of frequency and α'' is odd. Using these properties, we can collapse the integration range so that it is from 0 to infinity. Consequently, we can transform the integral for $\alpha'(f)$ into one of definite parity by multiplying the numerator and denominator of the integrand by $f + f_0$ and separating as $\alpha'(f_0) = \frac{1}{\pi}\int_{-\infty}^{\infty} \frac{f\alpha''(f)}{f^2-f_0^2}df + \frac{f_0}{\pi}\int_{-\infty}^{\infty} \frac{\alpha''(f)}{f^2-f_0^2}df$

(i.e., the integrand is separated into an even and an odd function). Since $\alpha''(f)$ is odd, the second integral vanishes, and we are left with $\alpha'(f_0) = \frac{2}{\pi}\int_0^\infty \frac{f\,\alpha''(f)}{f^2 - f_0^2} df$. The same derivation for the imaginary part yields: $\alpha''(f_0) = -\frac{2f_0}{\pi}\int_0^\infty \frac{\alpha'(f)}{f^2 - f_0^2} df$.

5.2.2 Active microrheology

Active microrheology uses microscopic particles embedded in the sample and detects their response to applied forces. The active method involves applying an oscillatory force to a single micron-sized bead. The amplitude and phase of the position of the bead and the applied force are determined, and the complex shear modulus is obtained from the bead response.

The equation of motion for a particle driven by an oscillating trap in a viscous medium is determined by two forces: the viscous drag force experienced by the particle, and the force imparted by the optical trap. Hookes' law, with an effective spring constant κ, can approximate the force produced by the laser on the trapped particle. Fig. 5.2 shows the forces on a particle of radius a, in an oscillating optical trap residing in a simple viscous liquid with viscosity η_0.

For a simple viscous liquid, the drag force is taken to be the Stokes drag $F_{drag} = -6\pi\eta_0 a v$, where η_0 is the zero shear viscosity of the liquid, and v is the velocity of the particle. For a micron-sized particle, this expression for the viscous drag is an approximation because the inertia of the fluid has been neglected (low Reynolds number flow), making the expression valid for relatively low oscillation frequencies.

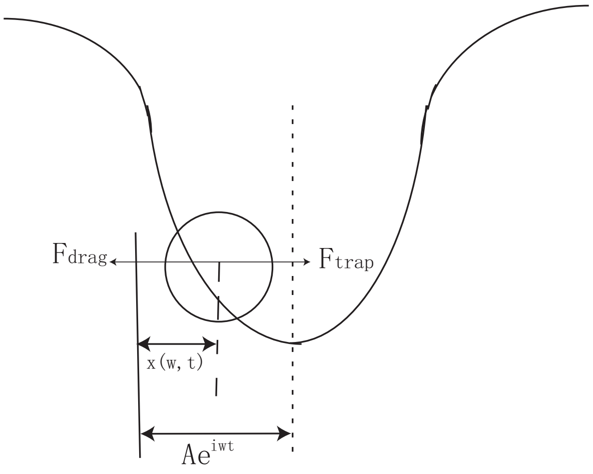

Figure 5.2: Schematic showing a damped driven harmonic oscillator, which illustrates the motion and the forces on a particle using an applied oscillatory laser trap. The solid line denotes the origin of the coordinate system, the dashed line indicating the location of the bead, and the dotted line the center of the oscillating trap. The equation of motion for the particle is: $m\ddot{x}(w,t) = -6\pi\eta(w)a\dot{x}(w,t) - \kappa(w)x + k_{ot}Ae^{iwt} - k_{ot}x(w,t)$, where k_{ot} is the trap stiffness of the oscillating beam, A is the amplitude of the oscillatory beam with frequency w, $\eta(w)$ and $\kappa(w)$ represent the viscosity and the elasticity of the medium, respectively, and $x(w,t)$ is the bead displacement with respect to the center of the trap (solid line).

The force due to the trap is given simply as the effective spring constant multiplied by the distance between the center of the particle and the center of the trap. Newton's second law of motion then leads to the equation of motion for the particle as: $m\ddot{x}(w,t) = -6\pi\eta(w)a\dot{x}(w,t) - \kappa(w)x + k_{ot}Ae^{iwt} - k_{ot}x(w,t)$, where k_{ot} is the trap stiffness of the oscillating beam, A is the amplitude of the oscillatory beam with frequency w, $\eta(w)$ and $\kappa(w)$ represent the viscosity and the elasticity of the medium, respectively. Here $x(w,t)$ is the time-dependent position of the particle as a function of oscillation frequency:

$$x(w,t) = x(w)e^{iwt} = D(w)e^{i(wt-\delta(w))} \tag{5.1}$$

To relate the motion of a single particle to the mechanical properties of the material surrounding the particle, the complex response function $\alpha(w)$, which is the ratio of the displacement of a particle to the external forces on the particle is calculated. The effective storage modulus, $G^{'}(w)$, and effective loss modulus, $G^{''}(w)$, are then obtained from $\frac{1}{6\pi a\alpha(w)}=\frac{k_{ot}}{6\pi a} + G(w) = \frac{k_{ot}}{6\pi a} + G'(w) + iG''(w)$, where $\alpha(w) = \frac{x(w)}{F(w)} = \frac{D(w)e^{-i\delta(w)}}{Ak_{ot}}$. Therefore, the storage and loss moduli of the medium can be calculated from the measured phase shift and amplitude of the particle motion using the following relationships:

$$G^{'}(w) = \frac{\kappa(w)}{6\pi a} = \frac{k_{ot}}{6\pi a}(\frac{Acos(\delta(w))}{D(w)} - 1) \tag{5.2}$$

$$G^{''}(w) = w\eta(w) = \frac{k_{ot}}{6\pi a}(\frac{Asin(\delta(w))}{D(w)}) \tag{5.3}$$

Chapter 6

Setup of the Optical Trapping and Position Detection System

6.1 Optical tweezers setup

The optical tweezers set up is illustrated in Fig. 6.1. The laser used is Diode Pumped (CrystaLaser) and has a maximum power of 500 mW. The 1064 nm wavelength is within a window of spectrum of minimal water absorption and cell damage. The laser beam first goes through an optical isolator (Thorlabs, Inc.), which prevents the reflected beam from re-entering the laser. Then the beam passes through a beam expander (CVI Laser, LLC), which lowers the incident power per area to reduce the wear on the optical components. A power attenuator made by combining a Glan Laser Prism (Zeta International) and a half-wave plate (CVI Laser, LLC) can

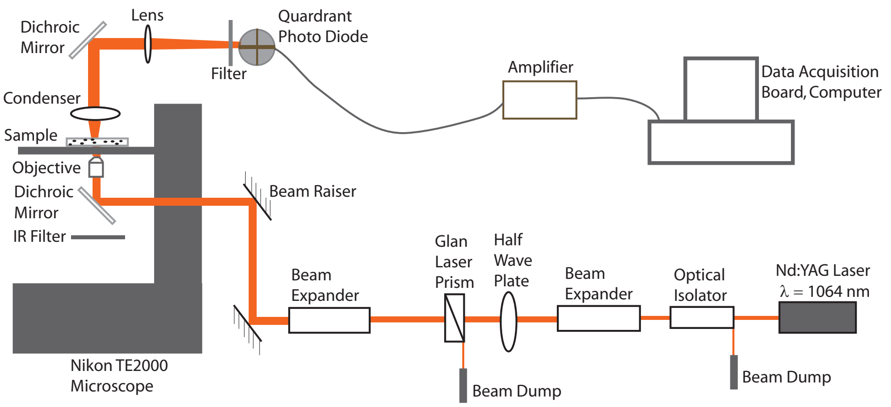
Dichroic Mirror
Lens
Quardrant Photo Diode
Filter
Amplifier
Data Acquisition Board, Computer
Condenser
Sample
Objective
Dichroic Mirror
IR Filter
Beam Raiser
Beam Expander
Glan Laser Prism
Half Wave Plate
Beam Expander
Optical Isolator
Nd:YAG Laser
λ = 1064 nm
Nikon TE2000 Microscope
Beam Dump
Beam Dump

Figure 6.1: Laser tweezers setup.

adjust the laser intensity. After the power attenuator, the beam goes through the second beam expander (Rodenstock) to increase the beam size enough to fill the back of the objective. The beam raiser consists of a stable rod and two mirrors set at 45°. After entering the inverted microscope (TE2000U, Nikon), the beam is reflected by a 1064 nm dichroic mirror (Part No. 900dcsp, Chroma Technology). The dichroic mirror reflects the laser beam upwards through the microscope objective while allowing visible light from the microscope light source above to pass downwards, and then reflected by another mirror to a FastCam PCI camera (FASTCAM-PCI R2, Photron). An IR filter is placed below the dichroic mirror to reduce the amount of residual laser light reflected by the sample from reaching the camera. An upper dichroic mirror of the same specification mounted at 45^o relative to the light path is used to direct the laser light from the back focal plane of the condenser to a lens. Finally, the laser beam reaches the quadrant photodiode detector (QPD). Room light is removed by a filter in front of the detector.

6.2 Position detection using photodiode detector

A Gaussian laser beam is brought to a focus at the sample by an objective lens and leads to the trapping of dielectric spheres as described previously. The condenser lens collects the diverging beam from the sample and images the laser focus where the bead is trapped. The trapped bead acts like a point-dipole scatterer. The incident light and the scattered light off the bead interfere and produce an intensity pattern on the back focal plane (BFP) of the condenser. The intensity distribution on the BFP of the condenser is then detected by a quadrant photodiode.

The signals from the four quadrants of the photodiode are combined and differentiated to obtain X and Y signals corresponding to the displacements of the bead in these directions in the plane normal to the propagation direction of the laser. For example, the x-position can be calculated by obtaining the total intensity and intensity difference in the two halves of the diode as follows: $\frac{I_{+}-I_{-}}{I_{+}+I_{-}} = \frac{16k\alpha}{\sqrt{\pi}w^2}\frac{x}{w}e^{-x^2/w^2}$, where $k = \frac{2\pi n_s}{\lambda}$ and λ is the wavelength of light, n_s is the refractive index of light in the solvent, w is the radius of the field on the focal plane and α is the electric susceptibility. As $x << w$, $\frac{I_{+}-I_{-}}{I_{+}+I_{-}} \propto x$.

The output signals are, after analog amplification and pre-processing by the differential amplifier, acquired as voltages using a BNC 2090 board and digitized using software written in Labview (National Instruments, Austin, TX).

6.3 Calibration of the optical trap

6.3.1 Theory

Various methods have been used to measure trap force in the linear region [70, 102, 31]. The method outlined below is commonly used to obtain trap stiffness. The equation of motion of a bead trapped in buffer solution is given by the equation: $\beta\frac{dx}{dt}+\kappa x = F(f)$, where β is the hydrodynamic drag coefficient and κ is the trap stiffness. $F(f)$ is the external random force due to Brownian Motion. The power spectral density (PSD), $S(f) = lim_{t\to\infty}\frac{2}{t}x_t(f)x_t(f)^*$, where $x_t(f)$=$\int_{-t/2}^{t/2} x(t^{'})e^{2\pi i f(t^{'})}dt^{'}$, can be shown to have a Lorentzian form: $S_{xx}(f) = \frac{k_BT}{\pi^2\beta(f^2+f_c^2)}$, which has a roll-off frequency $f_c = \frac{\alpha}{2\pi\beta}$, from which the trap stiffness can be calculated as: $\alpha = 2\pi\beta\, f_c$.

A position calibration factor for each laser power relates the quadrant diode output voltage to the displacement of the trapped bead with respect to the trap center. The position calibration factor is obtained by observing the thermal fluctuations of a bead in a buffer solution taken at the same power settings as for the actual samples of interest. Then a power spectral density $S_{vv}(f)$ was calculated from the voltage time series. We fit $S_{vv}(f)$ to a Lorentzian function $S_{vv}(f) = \frac{S_{vv}(0)\, f_c^2}{(f^2+f_c^2)}$, with $S_{vv}(0)$ and f_c as the fitting parameters. $S_{vv}(f)$ is related to the position power spectrum $S_{xx}(f)$ by $S_{vv}(f)$= $\rho^2 \cdot S_{xx}(f)$ (this equation can be taken as the definition for the conversion factor), where ρ represents the position conversion factor (in volt/nm). Take $f = 0$ Hz, we obtain $S_{vv}(0) = \rho^2 S_{xx}(0)$. Notice that $S_{xx}(0) = \frac{k_BT}{\pi^2\beta f_c^2}$, assuming that the

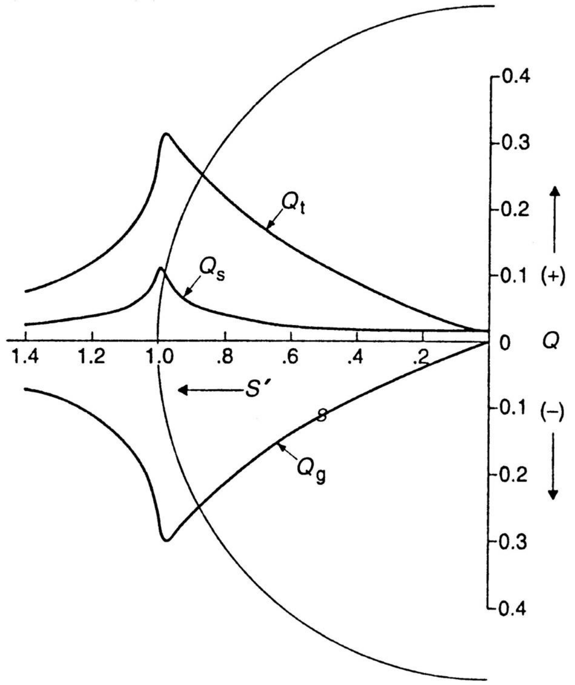

Figure 6.2: Scattering force, gradient force and total trap force on a one micron spherical particle as a function of the displacement of the particle to the trap center. This result is derived by A. Ashkin [9].

motion of the bead in the buffer is that of Brownian motion in pure water. So, $S_{vv}(0) = \rho^2 \frac{k_B T}{\pi^2 \beta f_c^2}$. Solving for ρ, we get $\rho = (\frac{S_{vv}(0) f_c^2 \pi^2 \beta}{k_B T})^{0.5}$, where β is the viscous drag coefficient of the particle in water and $S_{vv}(0)$ and f_c are obtained fitting parameters mentioned earlier.

Most optical traps are operated in such a way that the dielectric particle rarely moves far from the trap center. The reason for this is that the force applied to the particle is linear with respect to its displacement from the center of the trap as long as the displacement is small. In case of an application out of the trap center region, however, one needs to know the whole range force profile.

Over the whole range of the trap, Ashkin derived theoretically the total optical force on a bead as a function of distance between the focus of the laser beam and the center of the bead using geometric optics treatment [9]. Gittes *et al.* developed a method of calibrating the whole range trap force based on the fact that the rate of light momentum transfer is equal to the lateral trap force [36, 6]. Their experimental results were obtained using bead diameter smaller than the laser wavelength and the model they developed was based on small-particle scattering.

6.3.2 Experimental determination of trap stiffness and whole range trap force

We probed the force profile both in the linear region of an optical trap and in the region where the trap force decreases gradually. Our measured force profile using particle size of about 1.5 μm and laser wavelength of 1064 nm appears similar to that of the total optical force derived theoretically by Ashkin (Fig. 7 in [9]). Although the conditions of our measurements and the assumptions of the Ashkin derivation are not exactly the same, the force profile we obtained provides the actual strength and working range of the optical trap.

The trap stiffness near the center of the trap was first obtained from the power spectral density (PSD) of a trapped silicon bead of 1.5 μm diameter in water. The position fluctuation of the trapped bead was detected by a photodiode detector. The power spectral density of the bead was calculated and fit to a Lorentzian function [87, 3], $S_{xx}(f) = \frac{k_B T}{\pi^2 \beta (f^2 + f_c^2)}$, which has a roll-off frequency $f_c = \frac{\alpha}{2\pi\beta}$, where α is the trap stiffness and β is the viscous drag coefficient. Fig. 6.3a shows the data and fit of the power spectral density of a typical bead. From the value of the fitting parameter f_c ($\sim$40 Hz), we calculated the trap stiffness $\alpha = 2\pi\beta f_c \approx$ 0.0035 pN/nm.

The trap force near the center of the trap can also be obtained from the trap potential, assuming Boltzmann distribution of displacements of trapped particles. The probability distribution of displacement x of a typical bead $p(x)$ at the same laser intensity was used to obtain the trap potential $V(x)$ based on $V(x) = -k_B T\, ln(p(x)) + const$. The potential curve $V(x)$ was differentiated with respect to x to obtain the trap force. Fig. 6.3b shows the trap potential and a parabolic fit (dashed curve). Fig. 6.3c shows the corresponding trap force values (gray dots) and a linear fit (dashed line). Shown in comparison is a solid line with a slope equal to the trap stiffness

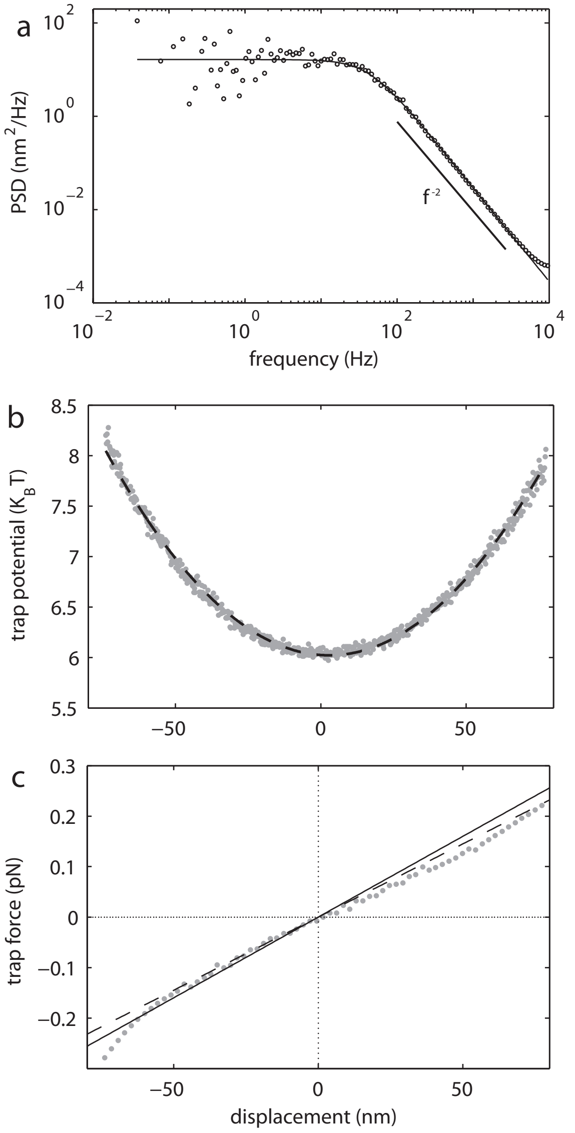

Figure 6.3: Measurement of trap force in the linear region of the trap. (a) Power spectral density of a typical bead and a Lorentzian fit $S_{xx}(f) = \frac{k_B T}{\pi^2 \beta (f^2 + f_c^2)}$. (b) Trap potential as a function of displacement and a parabolic fit. The potential is calculated from the distribution of bead displacement at the same laser intensity as that used in (a). (c) Comparison of trap force obtained from (a), denoted by the solid line, and (b), denoted by the gray dots and a linear fit to them shown as the dashed line.

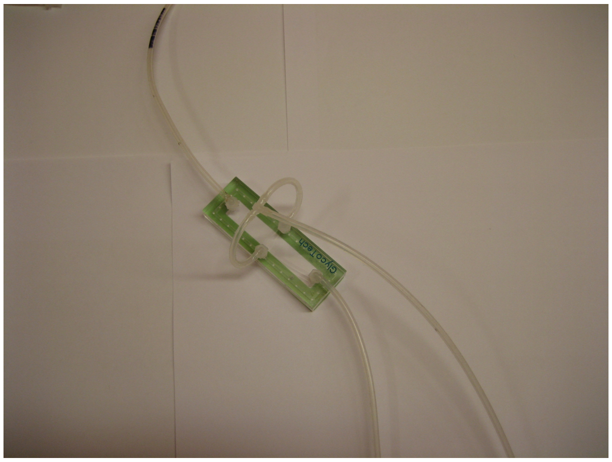

Figure 6.4: A picture of the flow cell. The cell is about 15 cm long and 5 cm wide. At the end of the cell are inlet and outlet tubings. The two outlets in the middle are connected to vacuum. A gasket is attached to the bottom of the cell (green) to ensure good isolation from the outside air and prevent leaking of solution.

calculated from Fig. 6.3a. The slopes of the two lines agree within 14 %. As can be seen from the linear fit to the gray dots in Fig. 6.3c, the relationship between the force and the displacement is approximately linear. Because the trapped bead rarely explored displacements that were beyond 100 nm from the trap center, experimental measurements of the trap force in the 100-500 nm range could not be obtained via the Boltzmann distribution method due to poor statistics.

In summary, the agreement of the trap force obtained by the power spectral density and the Boltzmann distribution analysis confirms the validity of both methods. The power spectral density method yields reliable result for the trap stiffness. The Boltzmann distribution method yields more directly the trap potential and the corresponding force. A drawback of the Boltzmann distribution method, however, is that the probability for the trapped particle to reach displacements far from trap center

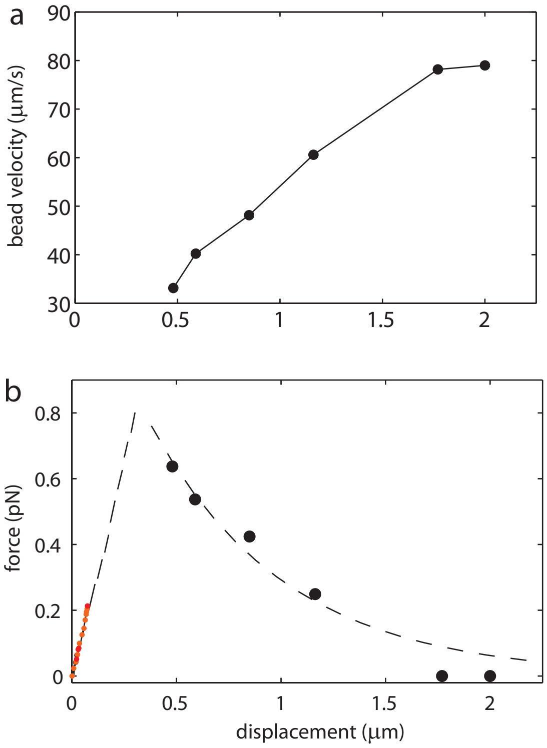

Figure 6.5: (a) The velocity of a typical bead initially trapped but then dislodged upon application of flow in the flow chamber. (b) The solid circles represent the force on the same bead as in (a) and were fit to an exponential function to yield $y = 1.4 \times e^{-1.5\,x}$ (dashed curve). In the linear region, the gray dots (red) within a displacement of about 100 nm are replots from Fig. 6.3c, and the dashed line depicts the expected force profile in this region.

becomes exceedingly small. Therefore, the statistics becomes inadequate to determine the potential reliably at large displacement. Nevertheless, the force it determines in the low displacement region is reliable.

We measured the trap force at the far edge using micron-sized beads in a flow chamber. A flow cell (GlycoTech) and a 170 μm thick glass coverslip formed the sample chamber. Flow was injected using a syringe filled with 1.5 μm diameter beads in water. The laser beam was focused inside the sample chamber and a bead was trapped before flow was applied. After the application of flow, the bead started to dislodge from the trap center when the flow speed increased and reached a threshold value. Several trials were performed in advance in order to optimize the progressing speed of the syringe pump, which produced the threshold flow speed. The trajectory of the escaping bead was recorded by the fast camera at 1000 fps, and the speed of the bead was measured along the trajectory. The trapping force was approximated as the following: $f_{trap} = 6\pi\eta a(v_{flow} - v_{bead})$, where the radius of the bead a is 0.75 μm, and v_{flow} and v_{bead} are the velocities of the flow and the bead, respectively. Here v_{flow} was taken as the terminal velocity of the bead. The speed of a typical bead in the flow chamber was plotted in Fig. 6.5a. The calculated force was plotted in Fig. 6.5b, denoted by solid circles, which were fit to an exponential function $y = 1.4 \times e^{-1.5\,x}$ (dashed curve).

Fig. 6.6 shows a schematic of the trap and the whole range trap force profile. The numbers represent displacements in micro-meters, with 0 indicating the center of the

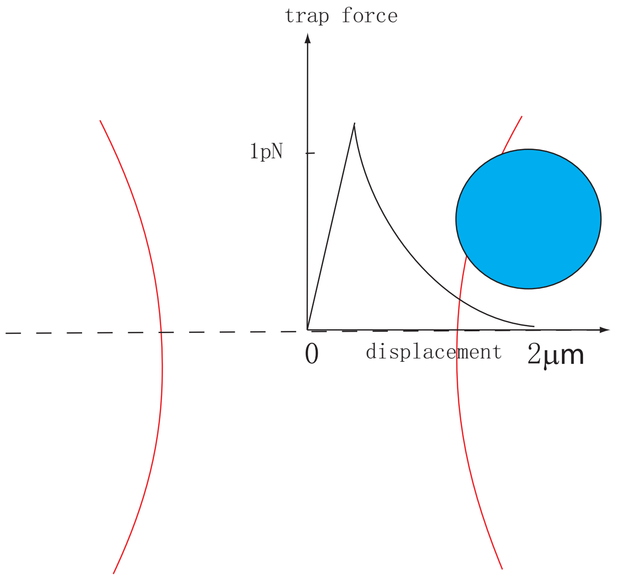

Figure 6.6: An illustration showing the force profile and range of a laser trap. A picture of the trap is shown in red, a probe particle in blue, and the whole force profile in black. The dashed line indicates the position of the beam waist. The dimensions are drawn roughly to scale. The trap force is linear with displacement in the low displacement regime, consistent with experiments. The force drops gradually down to zero beyond the peak when the bead is so far away from the trap center that no laser beams are scattered by the bead.

trap. The picture is drawn roughly to scale. An image of the probe particle is also shown.

Chapter 7

Application of Optical Tweezers in Microrheology of Microtubule and Actin Networks

7.1 Experimental methods

7.1.1 Measurement of viscoelasticity of isotropic and nematic actin networks using passive microrheology

Actin is a dominant cytoskeletal protein present in almost all eukaryotic cells. It plays an essential role in a variety of cell functions, such as motility, shape change, and mechano-protection [10]. For protein concentration up to a few mg/ml, actin filaments form an entangled isotropic network. Above a threshold concentration, F-actin solution undergoes an isotropic to nematic liquid crystalline phase transition [23, 32, 100]. Quantitative measurement of the elastic properties of actin networks in both phases is an essential first step in understanding the elasticity of cytoskeletal networks and the pivotal role of actin binding proteins in the mechanical behavior of the cell.

Actin was extracted from rabbit skeletal muscle following the technique of Pardee and Spudich [75] and kept in G-buffer (2 mM Tris HCl, pH 8.0, 0.2 mM ATP, 0.2 mM $CaCl_2$, 0.2 mM DTT, and 0.005% NaN_3) at $-80\ ^{\circ}C$ (G-actin). For experiments, aliquots of G-actin was thawed rapidly to $25\ ^{\circ}C$ and centrifuged for 5 min at 7000 g. The G-actin was then polymerized to form F-actin by adding KCl and $MgCl_2$ to final concentrations of 50 mM and 2 mM, respectively. For our experiments, the average filament length of F-actin was measured to be approximately 7 μm.

The beads used in our experiments are silica beads with a diameter of $1\mu m$ (Bangs Laboratories Inc., Fisher, IN). Bead suspensions were pre-diluted with the same buffer solution as that of F-actin before they were added to F-actin solutions in order to enable proper observation of beads motion without altering the ionic condition of F-actin. The mixed solutions were injected into rectangular capillary tubes (VitroCom Inc., Mt. Lakes, NJ) with cross-sectional dimensions of 0.1×1 mm^2. The tube long axis was defined as the x direction, and the y direction was perpendicular to the x direction and in the plane of observation. Due to the shear alignment when the sample was filled, the nematic director was along the x direction for F-actin in the nematic phase. Each capillary was immediately sealed with an inert glue to eliminate flow and evaporation from the system.

For passive microrheology measurements, we use a Nikon Eclipse TE 2000 inverted microscope. After loading a sample, the laser beam was focused at a sufficient height (larger than 10 μm) above the bottom surface of the sample chamber to minimize boundary effect. Displacement data for each bead was recorded until the desired number of data points were acquired (usually 540,000 or 1,080,000 data points per channel). Power spectral densities and Kramers-Krönig integrals were calculated using software written in C++. The complex shear modulus is calculated using the generalized Stokes relation, $G(w) = \frac{1}{6\pi a\alpha(w)}$, where $G(w) = G^{'}(w)+iG^{''}(w)$, as follows:

$$G'(\omega) = \frac{1}{6\pi a}\frac{\alpha'(\omega)}{[\alpha'^2(\omega)+\alpha''^2(\omega)]}\,, \tag{7.1}$$

$$G''(\omega) = \frac{1}{6\pi a}\frac{-\alpha''(\omega)}{[\alpha'^2(\omega)+\alpha''^2(\omega)]}\,. \tag{7.2}$$

For nematic solutions, $\alpha_x(\omega)$ and $\alpha_y(\omega)$ are different. Assuming decoupling of the motion in x and y directions, we consider separate response functions, $x(\omega) = \alpha_x(\omega)F_{x,\omega}$ and $y(\omega) = \alpha_y(\omega)F_{y,w}$. Using Eqs. 7.1 and 7.2, we obtain $G'_x(\omega)$, $G''_x(\omega)$, $G'_y(\omega)$ and $G''_y(\omega)$.

The $G''(\omega)$ that is measured experimentally incorporates the viscous modulus of both the buffer and the polymer network of interest. The solvent contribution $2\pi\eta f$ was subtracted from $G''(\omega)$, where η is the viscosity of the buffer solution (taken

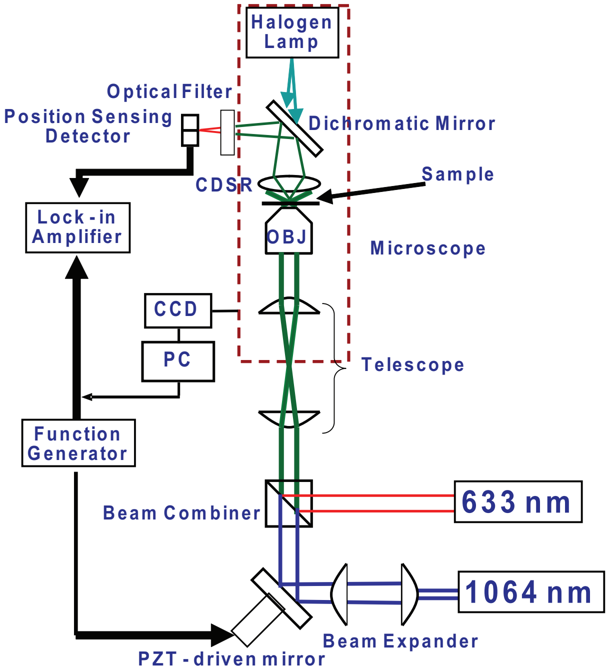
Halogen Lamp
Optical Filter
Position Sensing Detector
Dichromatic Mirror
Sample
CDSR
Lock-in Amplifier
OBJ
Microscope
CCD
PC
Telescope
Function Generator
Beam Combiner
633 nm
1064 nm
Beam Expander
PZT-driven mirror

Figure 7.1: A schematic diagram of the active microrheology experimental setup [104]. The area enclosed by the dashed lines represents an inverted optical microscope.

approximately as that of water). Since the probe particle experiences an elastic restoring force from the trap in addition to the elastic force from the medium, there is an elasticity contribution from the trap. Based on $G'(f) = \frac{\kappa(f)}{6\pi a}$, where $\kappa(f)$ represents the elasticity of the medium, the contribution to elasticity due to the trap stiffness is $k_{ot}/(6\pi a)$, where k_{ot} is the trap stiffness and a is the bead radius. This contribution has been subtracted from the measured G' values at every frequency.

7.1.2 Measurement of anisotropic elastic properties of MT bundled network using active microrheology

The use of oscillatory optical tweezers to trap and oscillate a particle embedded in an elastic medium and to measure its mechanical response has been demonstrated elsewhere [48, 98]. Fig. 7.1 shows the schematic diagram of the setup of an oscillating optical tweezer-based microrheometer used at Professor OuYang's lab at Lehigh University, where the active rheology experiments were conducted. The expanded beam has a size slightly larger than the back aperture of the microscope objective OBJ to achieve an "overfill, or full numerical aperture" condition. An infrared laser (Nd:YVO4 1064nm diode-pumped solid-state cw laser, Spectra Physics) was steered by a mirror mounted on a PZT (piezoelectric transducer, which converts electrical pulses to mechanical vibrations) 2-axis platform (S-330, Physik Instrument) which was connected to a function generator (a built-in function of the lock-in amplifier, Stanford Research SR-830) [104]. The active element of PZT is basically a piece of polarized material (i.e. some parts of the molecule are positively charged, whereas other parts of the molecule are negatively charged) with electrodes attached to two of its opposite faces. When an electric field is applied across the material, the polarized molecules will align themselves with the electric field, resulting in induced dipoles within the molecular or crystal structure of the material. This alignment of molecules will cause the material to change dimensions. The 2-axis platform allows the trapping beam to oscillate in two orthogonal directions (x and y), thus enabling the study of mechanical properties in two orientations.

The 1064 nm and 633 nm HeNe laser beams (Uniphase, 5mW) joined with a beam combiner cube into a collinear configuration were launched into the right side port of an inverted microscope (Olympus IX-81) via a telescope lens pair, and directed into the direction of microscope optical axis via a dichromatic mirror (not shown). An oil immersion objective lens (OBJ) (NA=1.3, 100X, Olympus) was used to focus both laser beams to a common focus. The 1064 nm beam was used to trap and the 633 nm beam was used to track the position of dielectric probe particles inside the sample.

The tracking beam, diffracted by the moving probe particle, was collected by the condenser CDSR (NA = 0.9) and projected onto a dual-lateral position-sensing detector (PSM2-4 and OT-301, On-Trak) where the motion of the probe particle in the transverse sample plane (X-Y plane) was tracked in real-time. An optical filter was inserted to prevent 1064 nm beam from reaching the detector. The lock-in amplifier, fed with signals from the detector and referenced with the sinusoidal electric signal that drove the PZT-driven mirror, provided the displacement amplitude and phase shift of the trapped particle with great sensitivity.

A CCD camera was installed on the microscope left-side-port to record bright-field images. The dichromatic mirror reflected laser beams and passed visible lights from the microscope halogen lamp so that sample imaging and rheological measurements could be performed simultaneously. The lock-in amplifier, PZT-driven mirror, and the microscope (including the CCD camera) were controlled by a PC.

We applied an oscillatory optical force to a trapped bead and analyzed the oscillatory motion of the particle to determine the viscoelastic moduli of the media. The trapped bead was forced to oscillate by the oscillatory tweezers driven by the PZT-controlled mirror.

The trap spring constant was determined by applying the equations for the amplitude and phase shift of bead displacement on water. The frequency-dependent amplitude and phase shift data were fit to the following equations [98, 104]:

$D(w) = \frac{A}{\sqrt{\tau^2 w^2 + (1 - w^2/w_0^2)}}, \ \delta(w) = tan^{-1}(\frac{\tau w}{1 - w^2/w_0^2}). \ Here \ \tau = \frac{6\pi\eta_0 a}{k_{ot} t}, \ w_0 = \sqrt{\frac{k_{ot}}{m}}.$
The spring constant k_{ot} thus deduced agreed with that measured by using Boltzmann statistics for a particle in a parabolic potential well.

Microtubule samples were prepared as follows: 3.6 mg/ml tubulin with 1.5 μm diameter silicon beads added was polymerized into MTs (taxol.OG was added with a molar amount 3.5% that of tubulin dimers to promote bundle formation and to label MTs). A chamber made of a glass slide and a coverslip with a thickness of about 100 μm was sealed with vacuum grease first and then further sealed using an inert glue. The slide was aged for about 24 h before measurements in order to minimize drift. In a typical measurement, a bead in the slide was located using bright field microscopy. MT bundles around the bead can also be examined using fluorescence microscopy. Confocal fluorescence images were taken, displaying the MT network around the bead.

7.2 Results and discussion

7.2.1 Moduli as a function of frequency for isotropic and nematic F-actin solutions

We use passive microrheology to measure G' and G" for isotropic actin solutions. We also characterized anisotropic viscoelasticity of nematic F-actin solutions, with the network more viscoelastic in the direction perpendicular to the nematic director. To our knowledge, this is the first time that the rheological properties of F-actin in the aligned phase are investigated.

There have been many rheological studies on conventional nematic polymer liquid crystals [7, 106, 11, 19]. Among the properties investigated are shear modulus as a function of concentration or temperature, and viscosity as a function of shear rate. However, few previous studies cover the anisotropic behavior of shear modulus in the nematic phase. Recently, a piezo-rheometer technique has been used to measure the complex shear rigidity modulus as a function of frequency and temperature of elastomers and polymers [33, 86, 61]. Martinoty *et al* [61] measured G' of nematic elastomers in two geometries, with shear rate perpendicular and parallel to the nematic director, respectively. This study shows anisotropy of viscoelasticity of nematic elastomers, with G'_y larger than G'_x. The lowering of G'_x in the nematic phase was attributed to the coupling between the shear and the director. Though the nematic elastomer with covalent crosslinks is different from the nematic F-actin network without crosslinks, these two systems do have similarly anisotropic viscoelasticity.

For both isotropic and nematic actin solutions, the displacements of the probe bead were recorded by the quadrant photodiode as voltage outputs which are proportional to displacements. Voltage outputs for two perpendicular directions are acquired by a BNC 2090 board and processed by LabVIEW. Then the response function $\alpha^*(\omega) = \alpha'(\omega) + i\alpha''(\omega)$ was calculated from power spectral density of the particle motion.

Typical results for a 0.5 mg/ml isotropic actin solution are shown in Fig. 7.2. Since the power spectral density was calculated from the displacements, which are discrete and cover only a limited time range, of the probe particle via Fast Fourier Transform, significant truncation errors near the frequency extremes were introduced, whereas it does give accurate results within the frequency region between the two extremes. To gain a physical understanding of the moduli, consider the two distinctive frequency regimes. At low frequencies, the elastic restoring force of the trap dominates the motion of the probe particle, so G' is larger than G". At high frequencies, the viscous damping force dominates the motion of the particle, so G" is larger than G'. Note that the moduli for the two orthogonal directions (x and y) overlap with each other, displaying isotropic viscoelasticity.

As we have noticed in Fig. 7.2, the data in low frequency range (below 1 Hz) is very noisy. In order to probe the low frequency viscoelastic properties more accurately, lower sampling frequencies (number of data points not changed) were used. Results

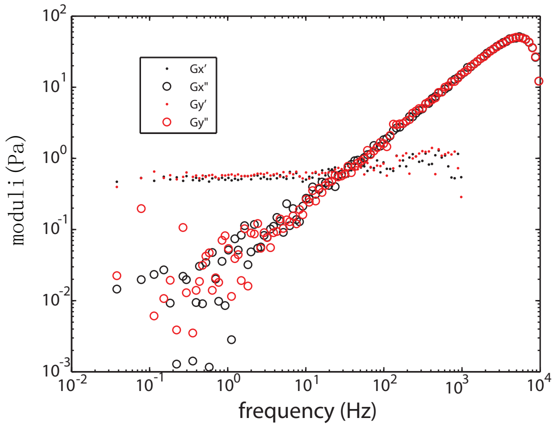

Figure 7.2: Moduli for a typical 0.5 mg/ml isotropic F-actin solution (contribution to elasticity due to the trap stiffness has been subtracted). Filled symbols represent G' and empty symbols represents G". Black symbols represent data for the direction perpendicular to the sample capillary. Red symbols represent data for the direction parallel to the capillary. The sampling frequency was 20000 Hz and 540000 data points were recorded.

with a sampling frequency of 2000 Hz and 540000 data points are shown in Fig. 7.3. By reducing the sampling frequency to 2000 Hz while maintaining the same number of data points (thus increasing the total measurement time), we were able to obtain more reliable low frequency information.

For the 1 mg/ml isotropic F-actin solution, G'_x and G'_y differ very little, and the same statement holds for G''_x and G''_y, showing isotropic viscoelasticity. The slight difference could be due to the weak metastable filament alignment caused by the shear flow as the sample was filled into the capillary. The G's have a weak dependence on frequency, showing the characteristic of a plateau modulus. The values of G' agree with those measured by Gardel *et al.* [34]. The G''s increase with frequency approximately in a scaling relation of $G'' \sim \omega^{3/4}$, consistent with the microrheology

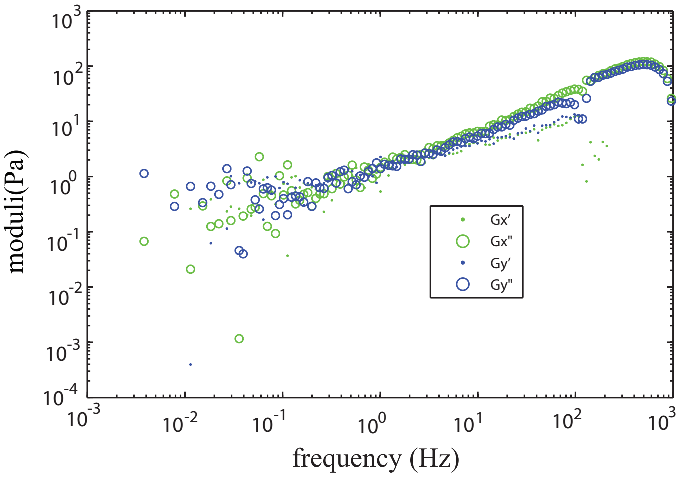

Figure 7.3: Moduli for a 1 mg/ml actin solution (contribution to elasticity due to the trap stiffness has been subtracted). Filled symbols represent G' and empty symbols represents G". Blue symbols represent data for the direction perpendicular to the sample capillary. Green symbols represent data for the direction parallel to the capillary. The sampling frequency was 2000 Hz and 540000 data points were recorded.

measurements by Gittes *et al.* [37], Xu *et al.* [108], and Mason *et al.* [63], and also with the recent optical tweezers passive microrheology results by Brau *et al.* [17].

The result (with a sampling frequency of 20,000 Hz, 540,000 data points) for a 4 mg/ml nematic actin solution is shown in Fig. 7.4 (LDPT). Shown together is the result for 4 mg/ml nematic actin solution obtained using video particle tracking (VPT) method, in which videos of bead motions are recorded, the positions of beads are tracked using MetaMorph software, and the displacements of the probe particles are measured.

For the 4 mg/ml nematic F-actin solution, results for G'_x, G'_y and G''_y agree with video particle tracking method. But the result for G''_x is one half of that measured by video particle tracking method in the overlapped frequency region. G'_x and G'_y both

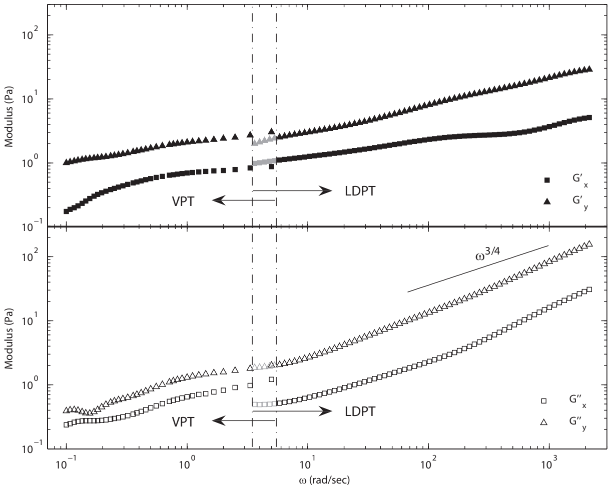

Figure 7.4: Frequency dependence of moduli for a 4 mg/ml nematic F-actin solution. For the spectra on the left, the bead displacement was measured with the VPT (video particle tracking) method and the mean square displacement was converted to moduli using Generalized Stocks Relation; for the spectrum on the right, the bead positions were tracked by the photodiode. In the overlapped region between the two dash dot lines, the laser tweezers based results are shown in gray symbols. The two methods give consistent results for G'_x, G'_y, and G''_y; G''_x measured by the VPT method, however, is about twice of that measured by laser tweezers based method. Both spectra were measured using 1 μm beads and obtained from averaging over ten beads. The solid straight line shows a scaling law of $\omega^{3/4}$.

show the behavior of plateau moduli. G''_x and G''_y follow a scaling behavior of $\omega^{3/4}$, consistent with recent optical tweezers passive microrheology results by Brau *et al.* [17].

The anisotropic viscoelasticity of nematic F-actin solutions can be interpreted based on the tube model [28, 65], which states that the motion of an individual filament in an isotropic network can be described as diffusing in a virtual tube constructed by its neighboring filaments (For a bead of diameter 1 μm embedded in an isotropic actin network, the mesh size is $\xi = 0.3\, c^{-0.5} = 0.3$ μm, where $c = 1$ mg/ml. For a bead with diameter of 1 μm embedded in a nematic actin network, the average spacing of two neighboring filaments is estimated to be $d = 0.17\, c^{-0.5} = 0.085$ μm, where $c = 4$ mg/ml). Consequently, the transverse diffusion of the filament is significantly suppressed, whereas its longitudinal diffusion is mostly unhindered. Since the transverse diffusion of the filaments is suppressed, the filaments whose contours are tangential to the bead experience more restriction in transverse diffusion and thus can hardly vacate room for the bead to diffuse, whereas the filaments pushing the bead with their ends can more easily diffuse away longitudinally, hence leaving more room for the beads to diffuse. In other words, the actin network is more resistant to perturbations in the transverse direction. As the complex shear modulus measures the resistance of material to deformations, it is reasonable that the modulus in the transverse direction is higher.

In summary, the laser tweezers based measurements are capable of giving high frequency information because the detector responds extremely fast to changes of the bead position. The method readily acquires a large number of data points, which can be efficiently processed by direct Fourier transform. The viscoelastic properties are isotropic for isotropic F-actin solutions, whereas nematic phase F-actin solution is more elastic in a direction perpendicular to the nematic director.

7.2.2 Anisotropic elastic properties of bundled MT network

MTs were labeled with taxol conjugated Oregon Green and imaged using spinning disc confocal microscopy, which enables us to observe the orientation of bundles during rheology measurements. Spinning disc confocal is capable of high spatial resolution and rapid image acquisition. The spinning disc consists of a thin wafer with hundreds of pinholes that are arranged in a spiral pattern. When a portion of the disc is placed in the internal light path of the confocal microscope, the spinning disc produces a scanning pattern of the subject. As the subject (exactly on the focal plane) is inspected, light is reflected back perpendicularly through the microscope objective. However, light that is reflected from in front of or behind the focal plane of the objective approaches the disc at an angle rather than perpendicularly. The pinholes of the disc permit only perpendicularly oriented rays of light to penetrate. This enables the microscope to view a very thin optical section of tissue, at extremely high speed because it is not limited by the speed of a scanning laser.

A typical superimposed confocal and bright field image is shown in Fig. 7.5A.

Three beads of 1.5 μm diameter are labeled. Bead 1 is embedded in a bundle. The oscillating laser beam is able to oscillate in two orthogonal directions, x and y, respectively. The amplitude and phase (with respect to the oscillating beam) of the bead motion were recorded. The storage and loss moduli of the medium were then calculated from the measured phase shift $\delta(w)$ and amplitude $D(w)$ of the particle motion.

The result of active rheological measurements for bead 1 is shown in Fig. 7.5B. Both moduli fall into the range of 5-500 Pa. Data at high frequency are noisy due to fluid inertia. Moduli in the directions along (x direction) and perpendicular (y direction) to the bundle orientation differ as expected. Also as expected, G'>G" at low frequencies and G'<G" at high frequencies.

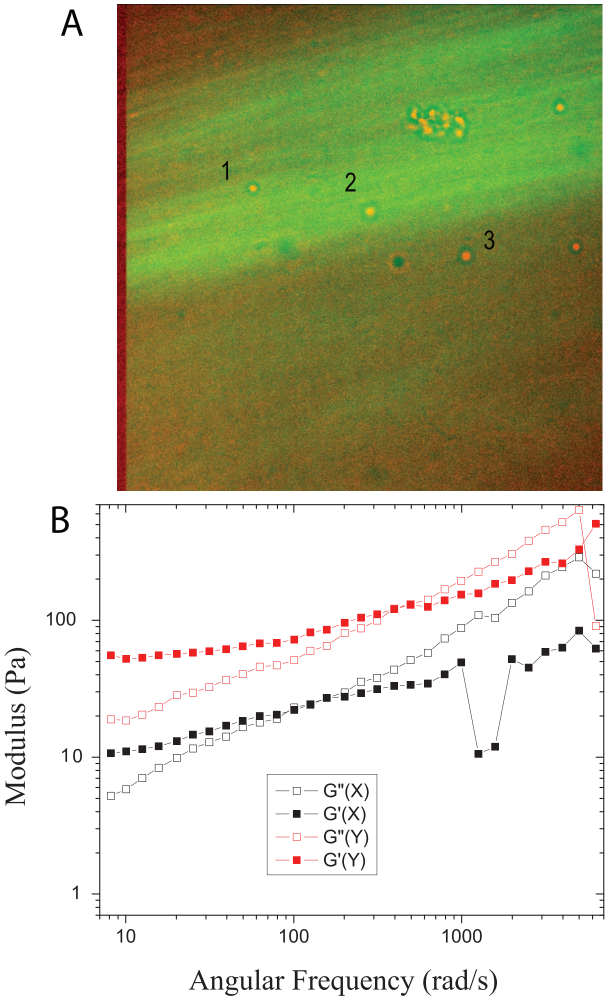

Figure 7.5: (A) A representative fluorescence image superimposed on a bright field image, so that both MT bundles (green) and beads (yellow) can be seen. (B) Moduli as a function of frequency for bead 1, showing large differences between the two directions.

Chapter 8

Application of Optical Tweezers in the Study of Bacteria Swimming and Adhesion

8.1 Introduction

laser tweezers have been used as a versatile tool for studying microorganisms at the single cell level [13, 12, 64]. We have built an in-house laser tweezers setup and used it to trap a single bacterial cell and study its cell body rotation, swimming, escape and adhesion.

Caulobacter crescentus is a Gram-negative bacterium ubiquitous in fresh water and soil [78, 79]. *C. crescentus* exhibits a dimorphic life cycle, dividing into a motile swarmer cell and a sessile stalked cell at every cell cycle [77]. A swarmer cell possesses a single polar flagellum and pili at the same pole [18], and swims by rotating its long, thin, helical flagellar filament, driven from the base by a reversible rotary motor. After the swarmer phase, the cell differentiates into a stalked cell, releasing the flagellum, retracting the pili, and synthesizing an adhesive holdfast and a stalk, a thin cylindrical extension of the cell envelope, at the same pole. The holdfast mediates an extremely strong adhesion of stalked cells to surfaces [95].

The adhesion of bacteria to surfaces plays a critical role in the environment, disease, and industry, and provides the critical first step in the biofouling of a surface and in biofilm formation. In this study, we optimize the use of optical tweezers to study *C. crescentus* motility and adhesion and to examine the effect of trap force on adhesion. We show that a swarmer cell can be captured and held vertical by an optical trap and can swim away upon decrease of the beam intensity to below a threshold. By measuring the swimming velocity of the cell during its escape from the trap, we have determined the trapping force exerted on the cell. In addition, recording the displacement of a trapped cell during the escape process provides further details on how the cell struggles and swims away from the trap. Finally, we show that the laser trap can be used to facilitate the adhesion of non-swimming stalked cells, which lack both the flagellum and pili, by bringing the stalked cells close to a surface.

8.2 Experimental methods

8.2.1 Bacteria sample preparation

Caulobacter swarmer cells were synchronized using the plate release method [25]. Briefly, *C. crescentus* CB15 cells were grown in a peptone yeast extract (PYE) medium (0.2% peptone, 0.1% yeast extract, 0.6 mM $MgSO_4$, and 0.5 mM $CaCl_2$) at 30°C with shaking at a rate of 100 rpm overnight. The culture was transferred to a petri dish with 15 ml fresh PYE after about 8 hours and was grown at room temperature overnight with gentle shaking. Then the petri dish was rinsed thoroughly with water and 20 ml fresh PYE was added to allow the cells to grow for another 5 hrs. The petri dish was rinsed with PYE and then 1 ml M2 salts (12 mM Na_2HPO_4, 8 mM KH_2PO_4, 9.3 mM NH_4Cl, 0.5 mM $MgSO_4$, 0.5 mM $CaCl_2$, 0.01 mM $FeSO_4$, 0.008 mM EDTA, pH 7.06) [79] solution was added and the petri dish was kept at room temperature for 5 min. An aliquot of the fluid containing swarmer cells born and released within the last 5 minutes from the plate surface was then taken from the petri dish for experiments.

In order to obtain stalked cells for adhesion experiments, 1 ml PYE instead of M2 salt was added in the final step as described above, and the petri dish was kept at room temperature for 5 min. After that, the solution containing swarmer cells were taken out of the petri dish and put into another petri dish with 10 ml PYE added. The cells were then grown for about 60 minutes at 30°C, by then they had lost their ability to swim, and differentiated into stalked cells.

8.3 Results and discussion

8.3.1 Trapping force on *Caulobacter* swarmer cells

We measured the force on a *Caulobacter* swarmer cell during escape from the trap. Briefly, a swimming swarmer cell was trapped and the laser intensity was reduced by turning the half wave plate until the cell was just about to escape from the trap. The critical laser intensity was defined as the intensity at which the bacterium just started to swim away from the trap center. We found that the critical intensity was at about 100 mW laser power and the difference among the critical laser intensity for different swarmer cells was within 10%. The trajectory of the cell was recorded by a fast camera at 250 fps and the velocity during the escape, V_{escape}, was calculated from the trajectory. The trapping force was approximated as the following: $f = (\alpha_c + \alpha_f)(V_{free} - V_{escape})$, where α_c is the drag coefficient for the cell body and taken as $6.8 \times 10^{-9} N\, s\, m^{-1}$, and α_f is the drag coefficient for the flagella filament and taken as $9.8{\times}10^{-9} N\, m\, s^{-1}$ [56]. The free swimming velocity of the swarmer cell V_{free} was taken as the final velocity of the cell when it was beyond 3 μm away from the trap center. V_{free} varied from cell to cell by about 20%.

The velocity of each of three bacteria after escaping from the trap center was plotted in Fig. 8.1a. Their velocities followed similar trend. The corresponding forces were plotted in Fig. 8.1b, denoted by empty symbols. Due to uncertainty in the determination of the cell center, the trapping force exerted on a cell within the initial 100 nm displacement was hard to measure.

As noted in Fig. 8.1b, the force exerted on the bacterium in the decaying region of the trap does not agree with that on a bead of comparable radius at the same displacement. This discrepancy is likely due to the difference in shape between a *Caulobacter* cell, which is about 1.5 μm in length and 0.5-0.8 μm in width, and a micron-sized spherical bead. During the escape as the cell swam away by up to half of the cell length from the trap center, part of the cell body would still remain in the trap. The net effect is that the escaping bacterium could sense the optical force over a larger range and therefore the drop of the optical force over distance appears less steep. The data shown in Fig. 8.1b are consistent with this assessment.

8.3.2 Cell body rotation of a trapped *Caulobacter* swarmer cell

Our observations indicate that the cell body aligns in the direction of the optical axis as it is trapped by the laser tweezers. Fig. 8.2 illustrates the reason for this alignment. A torque is produced by the laser trap when the elongated cell body is tilt from the optical axis. The torque thus induced rotates the cell body to be parallel with the optical axis direction. As to which end of the cell body is closer to the surface depends on the initial orientation of the cell body when it gets trapped. The

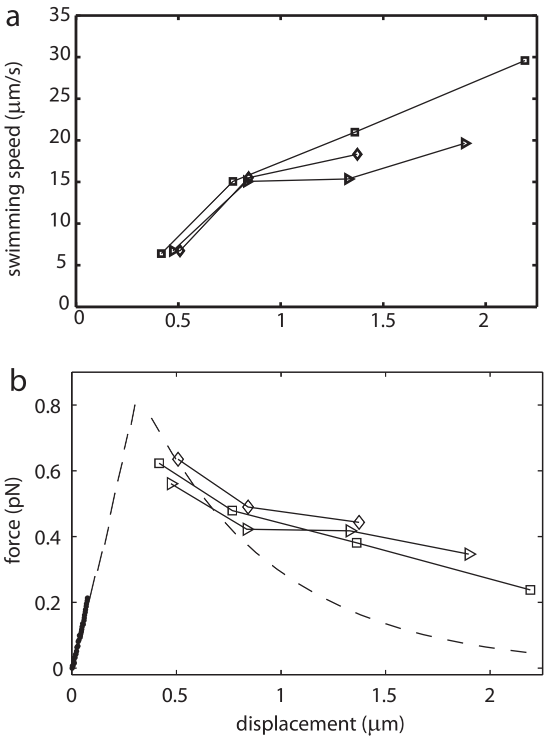

Figure 8.1: (a) The swimming velocity of each of three bacteria as a function of displacement from the center of the trap. (b) The empty symbols represent forces calculated from the velocities in (a), and the dashed curve is a replot from Fig. 6.5b. In the linear region, the gray dots within a displacement of about 100 nm are replots from Fig. 6.3c, and the dashed line depicts the expected force profile in this region.

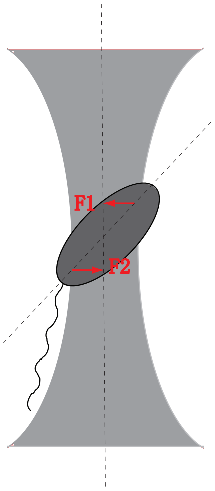

Figure 8.2: A schematic drawing which illustrates why the cell body aligns in the direction of the optical axis. Each end of the cell body experiences a trap force against the direction of the laser intensity gradient, shown as $F1$ and $F2$ in the figure. The net effect of these two forces is a torque which tends to rotate the cell body back to the optical axis direction. Therefore, the equilibrium position for the cell body is the optical axis direction.

net torque is zero when the axis of the particle is fully aligned. Because this torque depends on the detailed shape of the beam near the focus, it is not known exactly how big the torque is.

The cell body rotates and reverses the direction of rotation visibly unaffected by the laser trap. By direct counting of rotational cycles in recorded videos, the rate of rotation was measured to be about 50 Hz on average (ranging from 30 Hz to 60 Hz). This rotation rate is comparable to that of free swimming cells [56]. In addition, the average rotation rate was little affected by the laser intensity. We also noted that the switching frequency in the rotation of flagellar motor was unaffected by the laser trap (data not shown). Therefore, the laser tweezers did not appear to modify the swimming behavior of *C. crescentus* swarmer cells and provided a useful tool to study their adhesion to surfaces.

8.3.3 Escape of a *Caulobacter* swarmer cell from the laser trap

We noticed that as a *Caulobacter* swarmer cell escaped from the trap, it swam in a direction within about 20 degree angular deviation from the horizontal plane. This estimate was made based on our knowledge of the depth of focus, noting that the cell swam several micrometers away before it faded out of the depth of focus. Movies which display the escaping sequence as the laser intensity was decreased to about 100 mW were taken. Fig. 8.3 shows a few images extracted from a typical movie with times indicated. The movie covers approximately 1.4 seconds of real time. The cell body occasionally wobbled and tilted from the initially vertical orientation towards the horizontal plane prior to escape. From time to time, the cell body returned to the vertical orientation and then tilted towards another direction. Once the cell body tilted far to the side and became more or less parallel to the horizontal plane, it no longer returned back to the vertical position, but instead swam away.

In order to gain more details on how a trapped cell escapes from the trap center, the displacement of the escaping cell was recorded using a photodiode detector. Fig. 8.4a is a plot of a representative voltage signal in two orthogonal directions. The voltage reading shown on the vertical axis is proportional to the displacement of the cell body from the trap center projected in each direction. The dark thin curve shows that the total laser intensity reaching the sample was decreased stepwise. The

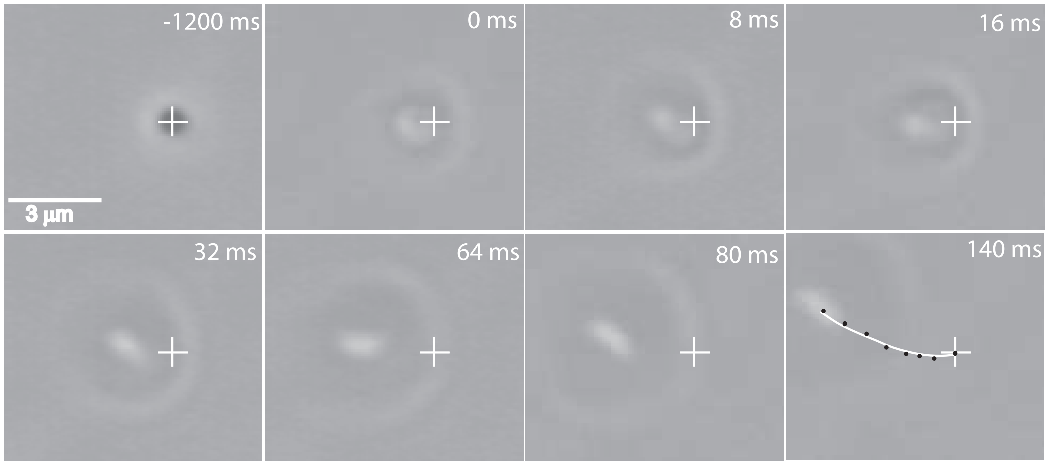

Figure 8.3: Selected frames from a movie displaying the escape process of a trapped swarmer cell. The cross indicates the position of the trap center. The white curve on the last image shows the trajectory of the cell. The dark dots indicate the center positions of the cell body over the eight frames.

position fluctuation of the cell right before escape was larger as compared to that when the cell was firmly trapped. Once the cell succeeded in an escape, the position fluctuation diminished and the cell quickly swam too far away from the trap center to be detected by the photodiode detector. Fig. 8.4b is a magnified view of the voltage trace during the escape process. The periodicity in the signal before escape indicates the constant rotation of the cell body. Fig. 8.4c shows the power spectral density of the time series signal in Fig. 8.4a. A broad peak at around 20 Hz indicates the rotation rate. The peak is smeared due to the fact that the rotation rate of the cell body varied over time and the cell tilted to varying extent during rotation. This rotation rate is smaller as compared to that for an average free swimming cell. To account for this discrepancy, we note that whenever the cell body appeared tilt, the rotational drag was increased and consequently the rotation rate was decreased.

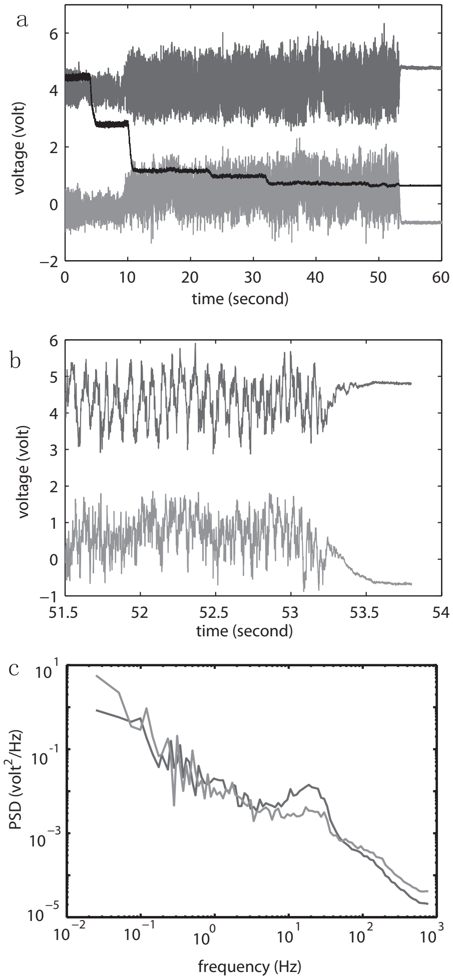

Figure 8.4: (a) Typical voltage signal as a function of time. The voltage is proportional to the displacement, projected in each of two orthogonal directions, of the cell body from the trap center. The dark thin curve shows that the total laser intensity was decreased stepwise. The other two curves represent the voltage traces in the two orthogonal directions acquired by the photodiode detector. (b) A magnified view of the voltage traces right before and after escape of the cell from the trap. (c) Power spectral density of the two voltage traces in (a), showing a wide peak corresponding to the rotation frequencies of the trapped cell.

We propose a qualitative explanation for the tendency of the cell to escape in near horizontal directions. When trapped, the cell body stands vertically, controlled by an optical restoring torque. As the laser intensity decreases, the optical torque also decreases. Thermal perturbations in the form of rotational Brownian motion cause the cell body to wobble and deviate from the optical axis direction. When the cell deviates from the optical axis, the direction of the force generated by the flagellum filament due to rotation driven by the flagellar motor no longer coincides with the axis of the cell body. The force component in the direction perpendicular to the axis of the cell body tends to rotate the cell body towards the horizontal direction, generating a torque in the opposite direction of the optical restoring torque. Once the optical torque falls below the torque induced by the flagellar motor, the cell proceeds by turning progressively towards the horizontal plane. In this new orientation, the trap force is smaller than when the cell body is vertical, where the whole cell body resides in the region of the strong electro-magnetic field generated by the optical trap. The propulsion force is then strong enough to overcome the trap force, and therefore the cell starts to swim away. Fig. 8.5 shows a schematic drawing of the configuration of the cell and the torque exerted on the cell body by the flagellar motor. The maximum measured torque induced by *Caulobacter* flagellar motor is in the range of 400-500 pN nm [56]. It is reasonable to assume that the trap force is on the order of 1 pN and peaks when the center of the cell body reaches a few hundred nanometers away from the trap center. Therefore the optical restoring torque is on the order of a few

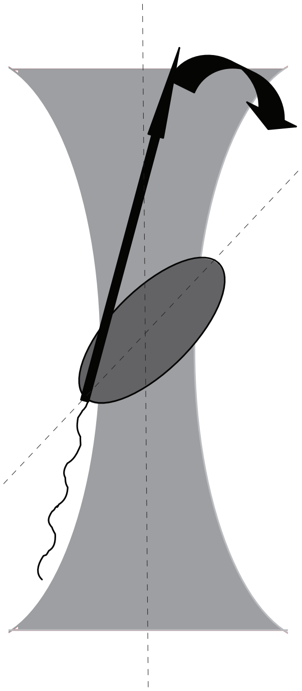

Figure 8.5: Schematic drawing of a cell tilting away from the optical axis. The straight arrow indicates the force generated by the flagella motor. The curved arrow indicates the resulting torque which tends to steer the cell towards the horizontal plane.

hundred pN nm, which is comparable to that of the torque induced by the flagellar motor, justifying the above explanation.

8.3.4 Facilitated adhesion of a *Caulobacter* stalked cell via holdfast using laser tweezers

We studied the kinetics of adhesion of stalked cells in order to understand the underlying mechanism of facilitation of adhesion by laser tweezers. Laser tweezers were used to bring a stalked cell into close proximity to a glass surface for 30 seconds and the probability of its adhesion to the surface was then examined. Effective attachment

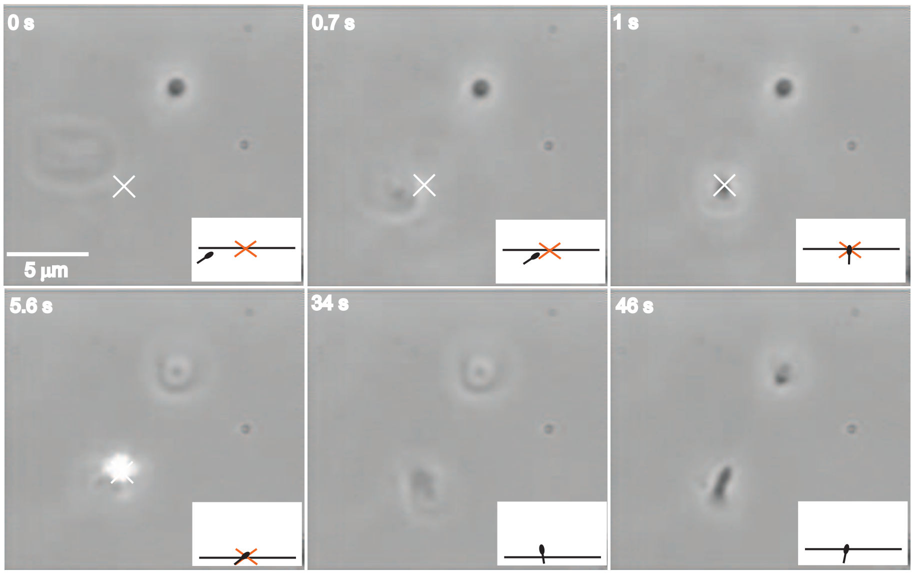

Figure 8.6: Facilitation of *Caulobacter* adhesion via holdfast by the laser trap. The cross indicates the center of the trap. The laser beam was blocked at later times, thus no cross is shown on the time frame of either 34s or 46s. The inset at the lower right corner of each picture depicts the facilitated adhesion process, in which the box represents the sample chamber, the dark tadpole-like drawing illustrates the cell and the horizontal line represents the position of the focal plane.

requires that the cell approaches the surface with the pole containing the holdfast. Since cells are oriented vertically in the trap, the success rate of adhesion is expected to be under 50% because in half of the attempts, the stalked cell would approach the surface with the non-adhesive pole. Among the twenty cells tested, nine resulted in adhesion, as they remained in place except for fluctuations due to rotational Brownian motion [55]. In contrast, the non-adhered cells jiggled away. This success rate was far higher than if laser trap was not utilized and there was only random collisions of holdfast-bearing cells with the surface [14]. Movies of facilitated adhesion were recorded for analysis of the process. Fig. 8.6 consists of selected frames from a typical movie to illustrate the process.

We propose that the enhanced rate of adhesion of *Caulobacter* cells with the presence of laser tweezers can be partly accounted for by laser tweezers aided encounter between the cell and the surface. The geometry of the laser trap ensures that the cell hits the surface either head or tail on, thus the interaction is confined to the vertical orientation. In other words, laser tweezers can steer the orientation and proximity of cells to facilitate adhesion. In contrast, in the absence of laser tweezers, the adhesion of stalked cells is a totally random process. The cell randomly hits the surface in a random orientation.

It was proposed that there is a repulsive barrier between the negatively charged glass surface and the negatively charged cell surface [14, 53]. Several recent studies explore the issue of existence of a repulsive barrier a bacterium must overcome prior to a productive attachment [49, 80, 97, 101]. The interaction energy is predicted based on the Derjaguin-Landau-Verwey-Overbeek (DLVO) theory, which is well established in the colloidal science literature [45]. Specifically, the DLVO theory predicts two minima in the interaction energy-distance curve between a bacterial cell and a surface (primary minimum and secondary minimum) [45, 60]. The cell body does not come to a close contact with the surface due to electrostatic repulsion since the opposing surfaces are both negatively charged. This electrostatic repulsion accounts for the repulsive barrier. After taking the van der waals interaction into consideration, which is attractive, the total interaction energy is actually negative upon close contact, shown as the primary minimum in Fig. 8.7. There is, however, a secondary minimum in the combined DLVO energy curve. The secondary minimum is in the range of a few nanometers to tens of nanometers away from the surface, depending sensitively on the ionic condition of the medium. Cells near the surface are easily trapped in the secondary minimum. Cells trapped in this minimum can still move laterally, due to either swimming or Brownian motion. Since the energy barrier between the two minima is quite large, cells must penetrate the barrier to be trapped in the primary minimum irreversibly, leading to an adhesion event.

Based on the predictions of the DLVO theory as described above, the cell must overcome an energy barrier in order to move from the secondary minimum to the primary minimum, which is about 10 nm closer to the surface than the secondary minimum. Some simulation work (G. Li, *et al.*, to be submitted) on the DLVO theory and the energy barrier indicates that the energy barrier is on the order of a few $k_B T$. In our experiment, the trap is used to grab the cell body and push it against the surface. The force applied on the cell is on the order of 1pN. So the energy input provided by laser tweezers is about $1pN \times 10nm$, which is sufficient to overcome the energy barrier, thereby facilitating adhesion.

8.4 Summary and conclusion

We have built a laser tweezers, which can manipulate micron-sized particles such as bacterial cells, and a sensitive displacement detection system. The displacement measurement allows us to detect nano-meter scale motion of the trapped particle.

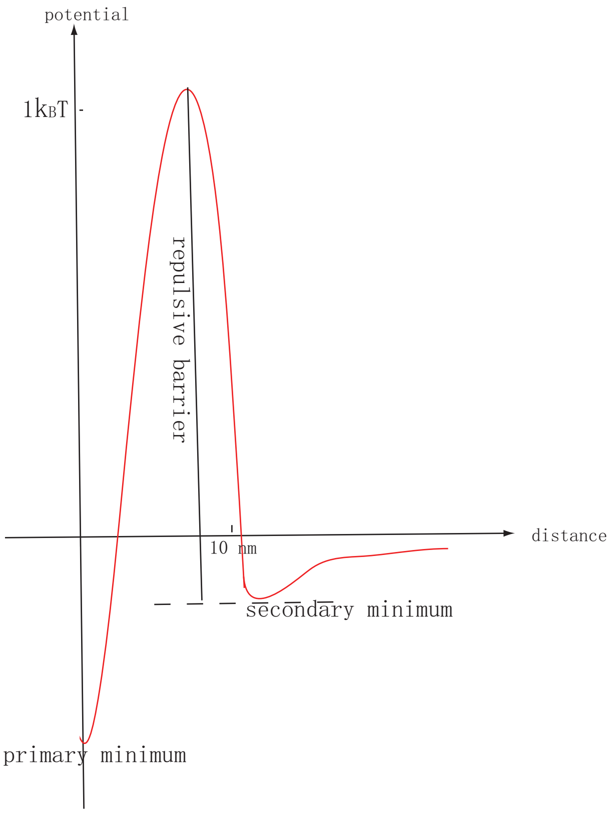
potential
1kBT
repulsive barrier
10 nm
distance
secondary minimum
primary minimum

Figure 8.7: An example of DLVO energy of a bacterium interacting with a flat glass surface as a function of the distance from the cell to the surface.

We have applied this laser tweezers setup in the passive microrheology studies of actin networks, especially in the nematic phase, which is, to our knowledge, the first study of this type using passive microrheology techniques. Our results regarding the moduli of the actin networks are consistent with literature and also agree with results measured using video particle tracking. Using the well-known tube model of polymer networks, we provide an explanation for the anisotropy of moduli in nematic actin solutions.

Using an oscillatory optical trap, we applied an oscillating force on a probe particle and studied the visco-elastic properties of microtubule bundles, which are highly aligned. Our results indicate strong anisotropy of moduli between the direction of bundle alignment and the direction perpendicular to the alignment. The technique of oscillating the laser beam in two orthogonal directions allows measurement of anisotropic viscoelasticity, which is at the frontier of the microrheology field.

We have characterized the force profile of the newly built laser trap using independent techniques and have shown agreement between different techniques. The detailed knowledge of relative strength and effective range of the trap enables its application in studies on biological systems such as bacteria, protein motors, and sub-cellular granules. Using the calibrated laser tweezers, we were able to measure the trapping force on a *Caulobacter* swarmer cell during its escape from the trap center. In addition, we were able to study the rotation of the cell body without attaching any part of the cell body to a surface, which may have further applications in the studies of bacterial rotary motor. We found that the slow down of rotation of the cell body upon decrease of laser intensity, rotational Brownian motion which causes the trapped cell to wobble and tilt, and the force generated by the flagellar motor together produce a net torque that counter-acts the optical restoring torque. Therefore, the cell tends to rotate towards the horizontal plane right before swimming out of the trap instead of escaping in the vertical direction.

Furthermore, we have used laser tweezers as a novel technique to study adhesion of a *Caulobacter* stalked cell. We demonstrated that laser tweezers facilitate the adhesion of stalked cells by orienting the future holdfast pole close to a surface. We further proposed that laser tweezers may help the cell overcome an energy barrier between the cell and the surface, assuming the predictions of DLVO theory regarding the two energy minima apply.

Bibliography

[1] The sample was polymerized from 8 mg/ml tubulin solution (same buffer condition as in [2]) in a $40 \times 10 \times 1\,\mathrm{mm}^3$ quartz cuvette and was subjected to convective flow (induced by asymmetrical thermal contacts, with the left and bottom surfaces in contact with a 37°C waterbath-warmed aluminum holder and other sides exposed to 30°C ambient) for the first 9 min. The cuvette was then laid flat on the microscope stage for observation and measurement at 30°C.

[2] The sample was polymerized from a 5 mg/ml tubulin solution (2 mM GTP, 3.5% in molar ratio of Oregon Green conjugated taxol to tubulin dimers, 100 mM PIPES, 1 mM EGTA, 2 mM $MgSO_4$, PH 6.9) in a $40 \times 8 \times 0.4\,\mathrm{mm}^3$ glass cuvette which was exposed to 9 T vertical static magnetic field for 5 min at 37°C (the magnetic field direction is along the long axis of the cuvette). The cuvette was then laid flat on the microscope stage and a coherently buckled area was chosen for observation and measurement at 30°C.

[3] Karim M. Addas, Christoph F. Schmidt, and Jay X. Tang. Microrheology of solutions of semiflexible biopolymer filaments using laser tweezers interferometry.

Phys. Review E., 70:021503–1–15, 2004.

[4] Wright A.J., Wood A.W., Dickinson M.R., Gleeson H.F., and Mullin T. The transverse trapping force of an optical trap: factors affecting its measurement. *J. of Modern Optics*, 40:1521–1532, 2002.

[5] B. Alberts, D. Bray, J. Lewis, M. Raff, K. Roberts, and J. D. Waston. *Molecular Biology of the Cell, 2nd edition.* Garland, New York, 1989.

[6] M.W. Allersma, F. Gittes, and C. F. Schmidt. Two-dimensional tracking of ncd motility by back focal plane interferometry. *Biophys. J.*, 74:1074–1085, 1998.

[7] T. Asada, H. Muramatsu, R. Watanabe, and S. Onogi. *Macromolecules*, 13:867, 1980.

[8] A. Ashkin. Trapping of atoms by resonance radiation pressure. *Phys. Rev. Lett.*, 10:729–732, 1978.

[9] A. Ashkin. Forces of a single-beam gradient laser trap on a dielectric sphere in the ray optics regime. *Biophys. J.*, 61:569–582, 1992.

[10] A. R. Bausch and K. Kroy. *Nat. Phys.*, 2:231, 2006.

[11] G. C. Berry. *Mol. Cryst. Liq. Cryst.*, 165:333, 1988.

[12] Richard M. Berry and Howard C. Berg. Absence of a barrier to backwards rotation of the bacterial flagellar motor demonstrated with optical tweezers. *Proc. Nat. Acad. Sci. USA*, 94:14433–14437, 1997.

[13] Steven M. Block, David F. Blair, and Howard C. Berg. Compliance of bacterial flagella measured with optical tweezers. *Nature*, 338:514–518, 1989.

[14] Diane Bodenmiller, Evelyn Toh, and Yves V. Brun. Development of surface adhesion in *Caulobacter crescentus*. *J. Bacteriol.*, 186:1438–1447, 2004.

[15] Clifford P. Brangwynne, Frederick C. MacKintosh, Sanjay Kumar, Nicholas A. Geisse, Jennifer Talbot, L. Mahadevan, Kevin K. Parker, Donald E. Ingber, and David A. Weitz. Microtubules can bear enhanced compressive loads in living cells because of lateral reinforcement. *J. Cell Biol.*, 173(5):733–741, 2006.

[16] W. Bras, G. P. Diakun, J. F. Diaz, G. Maret, H. Kramer, J. Bordas, and F. J. Medrano. *Biophys. J.*, 74:1509–1521, 1998.

[17] R R Brau, J M Ferrer, H Lee, C E Castro, B K Tam, P B Tarsa, P Matsudaira, M C Boyce, R D Kamm, and M J Lang. Passive and active microrheology with optical tweezers. *J. Opt. A: Pure Appl. Opt.*, 9:S103–S112, 2007.

[18] Y. V. Brun and R. Janakiraman. Dimorphic life cycles of *Caulobacter* and stalked bacteria. In Yves V. Brun and Larry Shimkets, editors, *Prokaryotic Development*, pages 297–317. ASM Press, 2000. book section.

[19] W. R. Burghardt and G. G. Fuller. *Macromolecules*, 24:2546, 1991.

[20] D'Helon C., Dearden E. W., Rubinsztiein-Dunlop H., and Heckenberg N. R. Measurement of the optical force and trapping range of a single-beam gradient

optical trap for micron-sized latex spheres. *J. of Modern Optics*, 41:595–601, 1993.

[21] Giuliano Callaini. *Development*, 107:35–41, 1989.

[22] Mireille M. A. E. Claessens, Mark Bathe, Erwin Frey, and Andreas R. Bausch. Actin-binding proteins sensitively mediate f-actin bundle stiffness. *Nature Materials*, 5:748–753, Sep 2006.

[23] C. Coppin and P. Leavis. *Biophys. J.*, 63:794, 1992.

[24] Lim C.T., Dao C., Suresh S., Sow C.H., and Chew K. T. Large deformation of living cells using laser traps. *Acta Materialia*, 52:1837–1845, 2003.

[25] Suzanne T. Degnen and Austin Newton. Chromosome replication during development in *Caulobacter crescentus. J. Mol. Biol.*, 129:671–680, 1972.

[26] Arshad Desai and Timothy J. Mitchison. Microtubule polymerization dynamics. *Annu. Rev. Cell Dev. Biol.*, 13(83):83–117, 1997.

[27] M. Dogterom and B. Yurke. *Science*, 278:856–860, 1997.

[28] M. Doi and S. F. Edwards. *The Theory of Polymer Dynamics.* Oxford University Press, Oxford, 1986.

[29] N. Dubey, P. C. Letourneau, and R. T. Tranquillo. *Exp. Neurol.*, 158:338–350, 1999.

[30] R. P. Elinson and B. Rowning. *Dev. Biol.*, 128:185–197, 1988.

[31] S Ermilov and B. Anvari. Dynamic measurements of transverse optical trapping force in biological applications. *Ann. Biomed. Eng.*, 32:1016–1026, 2004.

[32] R. Furakawa, R. Kundra, and M. Fechheimer. *Biochemistry*, 32:12346, 1993.

[33] J.L. Gallani, L. Hilliou, P. Martinoty, F. Doublet, and M. Mauza. *J. Phys.*, 6:443, 1996.

[34] M. L. Gardel, M.T. Valentine, J. C. Crocker, A. R. Bausch, and D. A. Weitz. Microrheology of entangled f-actin solutions. *Phys. Rev. Lett.*, 91:158302–1–4, 2003.

[35] Scott F. Gilbert. *Developmental Biology.* Sinauer Associates, Inc. Publishers, Sunderland, MA, 3th edition, 2000.

[36] F. Gittes and C. F. Schmidt. Interference model for back focal plane displacement detection in optical tweezers. *Opt. Lett.*, 23:7–9, 1998.

[37] F. Gittes, B. Schnurr, P. D. Olmsted, F. C. MacKintosh, and C. F. Schmidt. Microscopic viscoelasticity: shear moduli of soft materials determined from thermal fluctuations. *Phys. Rev. Lett.*, 79:3286–3289, 1997.

[38] J. R. Gladden, N. Z. Handzy, A. Belmonte, and E. Villermaux. Dynamic buckling and fragmentation in brittle rods. *Phys. Rev. Lett.*, 94:035503–1–4, 2005.

[39] Nicolas Glade and James Tabony. Brief exposure to high magnetic fields determines microtubule self-organisation by reaction-diffusion processes. *Biophys. Chem.*, 115:29–35, 2005.

[40] O. Glatter and O. Kratky. *Small Angle X-ray Scattering.* Academic Press, Washington D.C., 1982.

[41] Yongxing Guo, Yifeng Liu, Rudolf Oldenbourg, Jay Tang, and James M. Valles. Effects of osmotic force and torque on microtubule bundling and pattern formation. *Phys. Rev. E.*, submitted.

[42] Yongxing Guo, Yifeng Liu, Jay Tang, and James M. Valles. Polymerization force driven buckling of microtubule bundles determines the wavelength of patterns formed in tubulin solutions. *Phys. Rev. Lett.*, 98:198103–1–4, 2007.

[43] Robert Hard and Robert D. Allen. *Cell Motility*, 5:31–51, 1985.

[44] B. Herman, MA Langevin, and DF. Albertini. The effects of taxol on the organization of the cytoskeleton in cultured ovarian granulosa cells. *Eur J Cell Biol.*, 31:34–45, 1983.

[45] P.C. Hiemenz. *Principles of colloid and surface chemistry.* M. Dekker., New York, 1986.

[46] A. L. Hitt, A. R. Cross, and R. C. Williams. *J. Biol. Chem.*, 265:1639–1647, 1990.

[47] S. B. Horwitz. Mechanism of action of taxol. *Trends Pharm. Sci.*, 13:134–136, 1992.

[48] Lawrence A. Hough and H. D. Ou-Yang. Viscoelasticity of aqueous telechelic poly(ethylene oxide) solutions: Relaxation and structure. *Phys. Rev. E.*, 73:031802, 2006.

[49] B. Jucker, A. Zehnder, and H. Harms. Quantification of polymer interactions in bacterial adhesion. *Environ. Sci. Technol.*, 32:2909–2915, 1998.

[50] Daniel T. Kulp and Judith Herzfeld. Crowding-induced organization of cytoskeletal elements: 111. spontaneous bundling and sorting of self-assembled filaments with different flexibilities. *Biophys. Chem.*, 57:93–102, 1995.

[51] James R. LaFountain and Rudolf Oldenbourg. Maloriented bivalents have metaphase positions at the spindle equator with more kinetochore microtubules to one pole than to the other. *Mol. Biol. Cell*, 15:5346–5355, 2004.

[52] L. D. Landau and E. M. Lifshitz. *Theory of Elasticity.* Oxford, New York, 3rd english ed. edition, 1986.

[53] Assaf Levi and Urs Jenal. Holdfast formation in motile swarmer cells optimizes surface attachment during *Caulobacter crescentus* development. *J. Bacteriol.*, 188:5315–5318, 2006.

[54] A.J. Levine and T.C. Lubensky. The response function of a sphere in a viscoelastic two-fluid medium. *Phys. Rev. E*, 631:041510, 2001.

[55] G. Li, C. S. Smith, Y. V. Brun, and J. X. Tang. The elastic properties of the *Caulobacter crescentus* adhesive holdfast are dependent on oligomers of n-acetylglucosamine. *J. Bacteriol.*, 187:257–265, 2005.

[56] Guanglai Li and Jay X. Tang. Low flagellar motor torque and high swimming efficiency of *Caulobacter crescentus* swarmer cells. *Biophys. J.*, 91:2726–2734, 2006.

[57] Yifeng Liu, Yongxing Guo, James M. Valles, and Jay Tang. Microtubule bundling and nested buckling drive stripe formation in polymerizing tubulin solutions. *Proc. Natl. Acad. Sci. U.S.A.*, 103(28):10654–10659, 2006.

[58] Thomas L. Madden and Judith Herzfeld. Crowding-induced organization of cytoskeletal elements: 1. spontaneous demixing of cytosolic proteins and model filaments to form filament bundles. *Biophys. J.*, 65:1147–1154, 1993.

[59] Eckhard Mandelkow, Eva Maria Mandelkow, Hirokazu Hotani, Benno Hess, and Stefan C. Muller. Spatial patterns from oscillating microtubules. *Science*, 246:1291–1293, 1989.

[60] K.C. Marshall, R. Stout, and R. Mitchell. Mechanism of the initial events in the sorption of marine bacteria to surfaces. *J. Gen. Microbiol*, 68:337–348, 1971.

[61] P. Martinoty, P. Stein, H. Finkelmann, H. Pleiner, and H. Brand. *Eur. Phys. J. E*, 14:311, 2004.

[62] Alexander Marx, Jan Pless, Eva-Maria Mandelkow, , and Eckhard Mandelkow. On the rigidity of the cytoskeleton: Are maps crosslinkers or spacers of microtubules? *Cellular and Molecular Biology*, 46:949–965, 2000.

[63] T. G. Mason, T. Gisler, K. Kroy, E. Frey, and D. A. Weitz. Rheology of f-actin solutions determined from thermally driven tracer motion. *J. Rheol.*, 44(4):917–928, 2000.

[64] R. P. McCord, J. N. Yukich, and K. K. Bernd. Analysis of force generation during flagellar assembly through optical trapping of free-swimming chlamydomonas reinhardtii. *Cell Motil. Cytoskeleton*, 61:137–144, 2005.

[65] D. C. Morse. *Phys. Rev. E*, 63:031502, 2001.

[66] F. J. Nedelec, T. Surrey, A. C. Maggs, and S. Leibler. *Nature*, 389:305–308, 1997.

[67] D. J. Needleman, M. A. Ojeda-Lopez, Uri Raviv, Herbert P. Miller, Leslie Wilson, and Cyrus R. Safinya. *Proc. Natl. Acad. Sci. USA*, 101:16099–16103, 2004.

[68] Daniel J. Needleman, Miguel A. Ojeda-Lopez, Uri Raviv, Kai Ewert, Jayna B. Jones, Herbert P. Miller, Leslie Wilson, and Cyrus R. Safinya. Synchrotron

x-ray diffraction study of microtubules buckling and bundling under osmotic stress: A probe of interprotofilament interactions. *Phys. Rev. Lett.*, 93:198104–1–4, 2004.

[69] Daniel J. Needleman, Miguel A. Ojeda-Lopez, Uri Raviv, Kai Ewert, Herbert P. Miller, Leslie Wilson, and Cyrus R. Safinya. Radial compression of microtubules and the mechanism of action of taxol and associated proteins. *Biophys. J*, 89:3410–3423, 2005.

[70] Keir C. Neuman and Steven M. Block. Optical trapping. *Rev. Sci. Instrum.*, 75:2787–2809, 2004.

[71] R. Oldenbourg and G. Mei. *J. of Microscopy*, 180:140–147, 1995.

[72] Rudolf Oldenbourg, E. D. Salmon, and P. T. Tran. Birefringence of single and bundled microtubules. *Biophys. J.*, 74:645–654, 1998.

[73] Fumio Oosawa. *Polyelectrolytes.* Marcel Dekker, INC, NewYork, 1971.

[74] Cyril Papaseit, Nathalie Pochon, and James Tabony. *Proc. Natl. Acad. Sci. USA*, 97:8364–8368, 2000.

[75] J. D. Pardee and J. A. Spudich. Counterion-induced abnormal slowdown of f-actin diffusion across the isotropic-to-nematic phase transition. *Methods Cell Biol.*, 24:271, 1982.

[76] E.J.G. Peterman and et al. Extending the bandwidth of optical-tweezers interferometry. *Rev. Sci. Instrum.*, 74:3246, 2003.

[77] D. L. Pierce and Y. V. Brun. *Developmental control in Caulobacter crescentus: Strategies for survival in oligotrophic environments, Myxobacteria multicellularity and differentiation.* ASM Press, Washington D.C., 2008.

[78] J. S. Poindexter. Biological properties and classification of the *Caulobacter crescentus* group. *Bacteriol. Rev.*, 28:231–295, 1964.

[79] J. S. Poindexter. The *Caulobacters*: ubiquitous unusual bacteria. *Microbiol. Rev.*, 45:123–179, 1981.

[80] J.A. Redman, S.L. Walker, and M. Elimelech. Bacterial adhesion and transport in porous media: role of the secondary energy minimum. *Environ Sci Technol*, 38:1777–1785, 2004.

[81] Hidemi Sato, Gordon W. Ellis, and Shinya Inoue. *J. Cell Biol.*, 67:501–517, 1975.

[82] B. Schnurr and et al. Determining microscopic viscoelasticity in felxible and semiflexible polymer networks from thermal fluctuations. *Macromolecules*, 30:7781, 1997.

[83] B. I. Shklovskii. Wigner crystal model of counterion induced bundle formation of rodlike polyelectrolytes. *Phys. Rev. Lett.*, 82:3268–3271, 1999.

[84] Michael Shribak and Rudolf Oldenbourg. *Applied Optics*, 42:3009–3017, 2003.

[85] Bruce M. Spiegelman, Stephen M. Penningroth, and Marc W. Kirschner. Turnover of tubulin and the n site gtp in chinese hamster ovary cells. *Cell*, 12:587–600, 1977.

[86] P. Stein, N. Afalg, H. Finkelmann, and P. Martinot. *Eur. Phys.J. E*, 4:255, 2001.

[87] K. Svoboda and S. M. Block. Biological applications of optical forces. *Annu. Rev. Biophys. Biomol. Struct.*, 23:247–285, 1994.

[88] J. Tabony. *Science*, 264:245–248, 1994.

[89] J. Tabony and Nicolas Glade. *Langmuir*, 18:7196–7207, 2002.

[90] J. Tabony and D. Job. *Proc. Natl. Acad. Sci. USA*, 89:6948–6952, 1992.

[91] J. X. Tang, T. Ito, T. Tao, P. Traub, and P. A. Janmey. *Biochemistry*, 36:12600–12607, 1997.

[92] J. X. Tang, S. Wong, P. T. Tran, and P. A. Janmey. *Ber. Bunsenges. Phys. Chem.*, 100:796–806, 1996.

[93] John S. Toll. Causality and the dispersion relation: Logical foundations. *Physical Review*, 104:1760 – 1770, 1956.

[94] J. Torbet, J. M. Freyssinet, and G. Hudry-Clergeon. *Nature*, 289:91–93, 1981.

[95] Peter H. Tsang, Guanglai Li, Yves V. Brun, L. Ben Freund, and Jay X. Tang. Adhesion of single bacterial cells in the micronewton range. *Proc. Nat. Acad. Sci. USA*, 103:5764–5768, 2006.

[96] J. A. Tuszyński, T. Luchko, S. Portet, and J. M. Dixon. Anisotropic elastic properties of microtubules. *Eur. Phys. J. E*, 17:29–35, 2005.

[97] V. Vadillo-Rodriguez, H.J. Busscher, W. Norde, J. de Vries, and H.C. van der Mei. Relations between macroscopic and microscopic adhesion of streptococcus mitis strains to surfaces. *Microbiology*, 150:1015–1022, 2004.

[98] M. T. Valentine, L. E. Dewalt, and H. D. Ou-Yang. Forces on a colloidal particle in a polymer solution: a study using optical tweezers. *J. Phys. Condens. Matter*, 8:9477, 1996.

[99] R. B. Vallee. *Methods Enzymol*, 134:89–104, 1986.

[100] J. Viamontes, P. W. Oakes, and J. X. Tang. *Phys. Rev. Lett.*, 97:118103, 2006.

[101] M.A.S. Vigeant, R.M. Ford, M. Wagner, and L.K. Tamm. Reversible and irreversible adhesion of motile escherichia coli cells analyzed by total internal reflection aqueous fluorescence microscopy. *Appl. Environ. Microbiol*, 68:2794–2801, 2002.

[102] K. Visscher, S. P. Gross, and S. M. Block. Construction of multiple-beam optical

traps with nanometer- resolution position sensing. *IEEE J. Sel. Top. Quantum Electron.*, 2:1066–1076, 1996.

[103] W A. Voter and H P. Erickson. *J. Biol. Chem.*, 259:10430–10438, 1984.

[104] Ming-Tzo Wei, Angela Zaorski, and et. al. A comparative study of living cell micromechanical properties by oscillatory optical tweezers. *OPTICS EXPRESS*, 16:8594, 2008.

[105] Richard. C. Weisenberg, William J. Deery, and Peter J. Dickinson. Tubulin-nucleotide interactions during the polymerization and depolymerization of microtubules. *Biochemistry*, 15:4248–4254, 1976.

[106] K. F. Wissbrun. *J. Rheol.*, 25:619, 1981.

[107] D. L. Worcester. *Proc. Natl. Acad. Sci. USA*, 75:5475–5477, 1978.

[108] Jingyuan Xu, Andre Palmer, and Denis Wirtz. Rheology and microrheology of semiflexible polymer solutions: Actin filament networks. *Macromolecules*, 31:6486–6492, 1998.